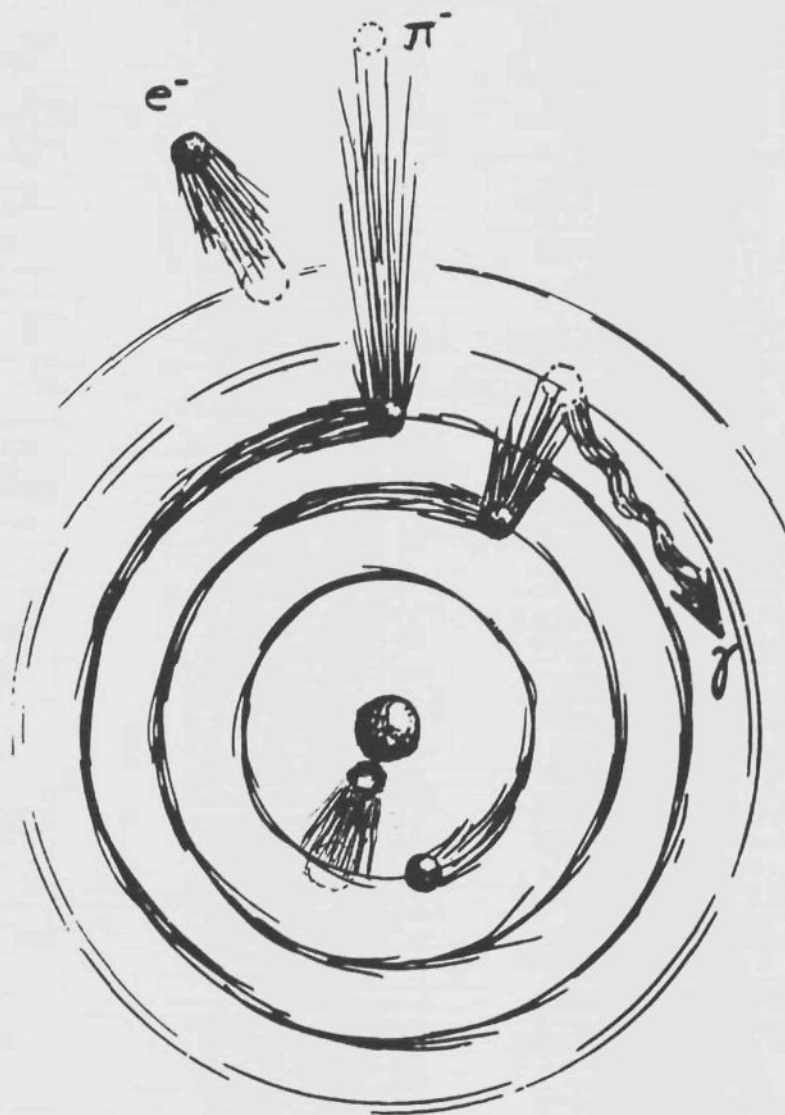


STRONG AND ELECTROMAGNETIC INTERACTIONS IN HEAVY EXOTIC ATOMS



TR diss
1623

C. T. A. M. de Laat

6400 79
317 0602
PA dec 1623

**STRONG AND ELECTROMAGNETIC INTERACTIONS
IN HEAVY EXOTIC ATOMS**

STRONG AND ELECTROMAGNETIC INTERACTIONS IN HEAVY EXOTIC ATOMS



Proefschrift

ter verkrijging van de graad van
doctor aan de Technische Universiteit
van Delft, op gezag van de Rector Magnificus,
prof. dr. J.M. Dirken, in het openbaar te verdedigen
ten overstaan van een commissie door het College
van Decanen daartoe aangewezen, op
31 maart 1988 te 16.00 uur
door

Cornelius Theodorus Adrianus Maria de Laat

geboren te Boxtel,
natuurkundig ingenieur

TR diss
1623

Dit proefschrift is goedgekeurd door de promotoren
prof. dr. A. H. Wapstra,
prof. dr. G. van Middelkoop.

dr. ir. J. Konijn heeft als begeleider in hoge mate bijgedragen aan het totstandkomen van het proefschrift. Het College van Dekanen heeft hem als zodanig aangewezen.

This work is part of the research programme of NIKHEF-K at Amsterdam, made possible by financial support from the Foundation for Fundamental Research on Matter (FOM) and the Netherlands' Organization for the Advancement of Pure Research (ZWO). It was also supported in part by the Swiss National Foundation and by the Bundesministerium für Forschung und Technologie of the Federal Republic of Germany and by the University of Warsaw.

Aan mijn ouders

Aan Emelie

CONTENTS

1	Introduction	1
2	Improvements in experimental methods and analysis	5
2.1	Introduction	5
2.2	Basic interactions in gamma-ray detectors	6
2.3	Compton suppression	7
2.3.1	Background contributions	7
2.3.2	Compton suppression scintillation crystal design	8
2.3.3	Compton suppression spectrometer set-up	12
2.4	Neutron time of flight discrimination in γ -ray detection	12
2.5	Experimental and electronic set-up	16
2.6	Reprint: General-purpose fast CAMAC software for PDP-11 computers	20
2.7	Data reduction	26
2.8	Fit program	26
2.8.1	General structure of the program	26
2.8.2	Peak shape representation functions	27
2.8.3	Hyperfine complexes	29
2.8.4	Step function	29
2.9	Relative efficiency calibration	31
3	Theory of hadronic interactions in pionic atoms	33
3.1	Introduction	33
3.2	The Klein Gordon equation	35
3.3	π -N scattering and the π -nucleus interaction	35
3.4	Coulomb potential and nuclear density distribution functions	39
3.5	Optical potential parameter fits	40
3.6	Deformation	41
3.7	Higher order corrections	44
3.8	Optical potential calculations	48
3.8.1	Strong interaction monopole shifts and widths	48
3.8.2	Quadrupole splitting	49

4	Systematics of 3d and 4f pionic levels in ^{181}Ta, natural Rhenium, natural Platinum, ^{197}Au, ^{208}Pb, ^{209}Bi and ^{237}Np	53
4.1	Introduction	53
4.2	Experiments	54
4.2.1	Pionic atoms of the spherical nuclei $^{\text{nat}}\text{Pt}$, ^{197}Au , ^{208}Pb and ^{209}Bi	55
4.2.1.1	Pionic $^{\text{nat}}\text{Pt}$ and ^{197}Au	56
4.2.1.2	Pionic ^{208}Pb	58
4.2.1.3	Pionic ^{209}Bi	61
4.2.2	Pionic atoms of the strongly deformed nuclei ^{181}Ta , $^{\text{nat}}\text{Re}$ and ^{237}Np	64
4.2.2.1	Pionic ^{181}Ta	64
4.2.2.2	Pionic $^{\text{nat}}\text{Re}$	67
4.2.2.3	Pionic ^{237}Np	69
4.3	Strong interaction level widths from intensity balances	70
4.4	Discussion and conclusions	72
4.4.1	Strong interaction monopole shifts and widths	72
4.4.2	Extension of optical potential terms	76
4.4.3	Strong interaction quadrupole shifts	85
4.4.4	Summary	86
5	The Quadrupole Moment of ^{237}Np	87
5.1	Introduction	87
5.2	Muonic X-rays and nuclear structure effects	88
5.3	Experimental details and results	90
5.4	Discussion	92
	References	95
	Appendix A Reprint: The Probability of Non-Radiative Decay of the 3d level in Muonic ^{237}Np	99
	Appendix B Detailed tables of pionic atom calculations	105
	Summary	115
	Samenvatting	117
	Curriculum Vitae	119



Chapter 1

Introduction

This thesis is concerned with phenomena that occur when a negatively charged particle interacts with an atom. Such a particle can occupy quantum mechanical orbits around the atomic nucleus which, for the same principal and angular momentum quantum numbers, have radii smaller than those for the atomic electron by the ratio of the masses of the two particles. Their binding energies are larger by the same ratio, in first approximation. Since even the lightest of such particles, the muon, has a mass $m_\mu = 211 m_e$, all pertinent orbits lie far inside even the smallest electron orbits. Their energies are therefore little influenced by the presence of the electrons in the "exotic" atom formed by the capture of such a negative particle. Moreover, this influence is caused by the well known electromagnetic interaction and can therefore be calculated with sufficient precision, as will be shown in chapter 3.

The influence of the structure of the nucleus on electron orbits is almost negligible (hyperfine structures excepted). This is no longer true for exotic atoms. Especially if the exotic particle is a muon, the wave function describing the innermost orbit has a considerable overlap with the nucleus and is therefore strongly influenced by the distributions of nuclear charge and magnetism. Since this influence is almost purely electromagnetic for leptons, it can be used to obtain from measurements precise information on these distributions, such as the average charge radius, its surface thickness, and the nuclear electric quadrupole moment. For heavier nuclei the weak interaction has a noticeable influence but essentially only to the effect that the muon will be absorbed by the nucleus within around 10^{-7} s.

If, however, the negative particle is a hadron, it will experience the strong interaction with the nucleus. This influence decreases very rapidly with increasing distance between the two and therefore the strong interaction has only minor influence on the properties of outer orbits. In inner orbits, it causes in the first place fast absorption of this hadron by the nucleus. As a result, the atom exists only shortly in a state with such an orbit, and therefore its energy has a considerable width. This effect increases so drastically as the captured particle cascades down through atomic orbits that until only few years ago the strong interaction width could be measured for just one state directly from the line shape. Not only is the population of the next lower state decreased as a consequence of absorption from the higher one, but also its width becomes so large that transitions to it are quite difficult to disentangle from continuous backgrounds always present.

In the second place, the strong interaction affects the energies of such states. This effect is commonly described as a "shift" to the actual energies from the energies that a lepton of the same

mass would have around a point nucleus of the same nuclear charge (as mentioned above, the latter energies can be calculated very accurately).

The properties of the strong interaction are much less well known than those of the electromagnetic one. More and precise information on its effects is therefore valuable. The present work intends to provide such information from sophisticated measurements of such shifts and widths for more than one level in pionic atoms (the pion being the lightest hadron, $m_\pi \approx 273 m_e$).

Of course, such measurements have been performed before. Attempts have been made to describe these shifts and widths by inserting in the Klein Gordon equation for the pion-nucleus system an optical potential representing the strong interaction (see chapter 3). The optical potential, developed by Kisslinger and modified by Ericson and Ericson, adequately predicts the strong interaction effects on the complex energy levels in pionic orbits not too close to the nucleus. Rather recently, experimental results for the deeply bound pionic 3d orbit in heavy nuclei such as ^{181}Ta , $^{\text{nat}}\text{Re}$ and ^{209}Bi indicate, however, that for them strong interaction widths are smaller by a factor of up to two or more than predicted from the standard optical potential theory. Such a tendency for strong interaction absorption widths has also been observed in other deeply bound pionic atom orbits: the 3p in ^{110}Pd , 2p in ^{75}As and 1s in ^{23}Na . These nuclei are reported to have smaller absorption widths by a factor of about 1.5 as compared to theoretical predictions. Similar deviations from theory have been observed for the strong interaction shifts.

Some authors have suggested that at least part of the anomalies might be due to the influence of deviations of the nucleus from spherical symmetry (nuclear deformation). We therefore studied some cases (^{208}Pb , ^{209}Bi) where deformation plays no role but where otherwise, by analogy, strong anomalies could be expected. The results, discussed in chapter 4, do not indicate a strong influence of deformation.

Some other authors disputed reported anomalies on experimental grounds. We therefore reinvestigated some cases devoting special attention to methods of obtaining clearly improved results (see chapter 2). The improvement was partly established by using modern spectroscopic equipment such as large-volume high-purity Ge-detectors in combination with Compton suppression BGO-shields. We also took care to provide good statistics by making measurements using very intense pion beams at the meson factory Paul Scherrer Institut (formerly Schweizerisches Institut für Nuclearforschung). This is especially necessary in cases where the absorption from the next higher level is already large (Pb, Bi) or where the influence of the nuclear quadrupole moments causes an extra complication (see chapter 3.4) such as for Ta and Re. Highly important is also the attention paid in attempts to reduce backgrounds or, where this was not possible, to correct for them (see chapter 2). Thus, e.g., the neutrons, produced in the target under investigation, cause in the Ge-detectors nuclear reactions and background radiation. We could eliminate this part of the background almost completely by making use of the fact that these

neutrons travel more slowly than electromagnetic radiations. As a result of all these improvements, we are able to show that the deviations from the theory as mentioned are indeed real.

In reconsidering the optical potential theory (chapter 3) we noted, that up to now most authors use equal radii for the proton and neutron distributions in determining the parameters of the potential. By introducing a slightly larger neutron distribution radius as is found also in scattering experiments, we could obtain a significantly better, though not perfect agreement with the present experimental values. We also noted that some possible absorption terms had not been taken into account, more specifically those that depend on the difference between the density distributions of protons and of neutrons in the nucleus. Neglecting these isovector terms can be defended for relatively light nuclei and higher orbits, but possibly not for the cases where the anomalies are found. We will indeed show in chapter 4 that a further improvement between experiments and theory results if this term is taken into account.

In the treatment of the experiment on ^{237}Np , knowledge of the electrical quadrupole moment of its nucleus is required. Also as a demonstration of the possibilities of measurements with exotic atoms, its determination has been treated in a separate chapter (5).

Chapter 2

Improvements in experimental methods and analysis

2.1 Introduction

Due to the fact that deeply bound pionic orbits become very broad with increasing Z , the pionic X-ray transitions populating such levels are wide and difficult to observe in a high background environment. Therefore, until recently, strong interaction shifts and (directly measured) widths could be studied for only one level in a pionic atom. Much better information about the pion-nucleus interaction and a better understanding of the higher-order terms in the optical potential would be obtained from a knowledge of shifts and widths for two subsequent transitions, connecting pionic orbits with different overlap between the pion wave function and the nucleus.

Important facts affecting the precision in establishing the position and width of the pionic X-rays are the complexity of the spectra and the following background contributions:

- 1) The pionic X-rays and γ -rays can suffer Compton scattering in the target material, in the material between target and detector, and in the detector itself. In most cases no contribution to the full energy peak will then occur, since the detector registers less than the original pionic X-ray transition energy.
- 2) Neutrons produced after pion absorption can scatter inelastically in the Ge-detectors and thus excite nuclei. These subsequently decay by transitions which, since produced inside the detector, have a high detection probability. Their photo peaks have a characteristic exponential tail at the high energy side, due to the kinetic energy transferred by the neutron to the Ge-nucleus.
- 3) The nucleus remaining after absorption of the pion and emission of several nucleons is usually left in an excited state, which mostly decays by emitting γ -rays.

Before 1977 shifts and widths were only known up to $Z = 10$ for the 1s level, $Z = 30$ for 2p and $Z = 60$ for 3d. Beyond these Z -values, separation of the pionic X-ray transitions from the background becomes increasingly difficult, especially since these broad and low-intensity transitions are often obscured by nuclear γ -rays. The availability of intense pion beams at the meson facilities started to improve the possibilities. Data acquisition systems and detection devices also became more sophisticated combined with the introduction of modern spectroscopic techniques such as Compton suppressed germanium spectrometers and the elimination of neutron induced backgrounds by time of flight. The Z -range for e.g. the 3d-level could be extended to $Z = 83$ as is demonstrated in the present work.

2.2 Basic interactions in gamma-ray detectors

The number of electron-hole pairs which are collected by the electric field across a germanium diode detector is essentially proportional to the energy deposited by the secondary electrons produced by the incident γ -ray. We here summarize the basic processes producing these secondary electrons.

In the photo-electric process (photo effect) all the energy E_γ of the incident photon is absorbed by a bound electron of an atom. As a result the atom is left with an electron vacancy causing emission of X-rays or Auger-electrons. Both are generally absorbed too so that the total energy E_γ is absorbed within the detector and a full-energy peak is observed.

In the Compton process incident photons are scattered by the electrons with a partial energy loss. The energy $E_{\gamma'}$ of the scattered photon is

$$E_{\gamma'} = \frac{E_\gamma}{1 + (1 - \cos \theta) E_\gamma / mc^2} \quad (2 - 1)$$

and that of the scattered electron is

$$E_e = E_\gamma - E_{\gamma'} \quad (2 - 2)$$

where m is the rest mass of an electron.

Thus, the primary Compton electron energy spectrum extends from zero energy ($\theta = 0^\circ$) up to a maximum energy ($\theta = 180^\circ$) or Compton edge:

$$E_{CE} = E_\gamma - \frac{1}{2} mc^2 / \left(1 + \frac{mc^2}{2E_\gamma} \right) \quad (2 - 3)$$

Secondary interactions between the scattered γ -ray and the detector partly fill up the gap between the Compton edge and the full energy peak, or contribute to the latter. An incident γ -ray with an energy in excess of $2mc^2$ (1.02 MeV) may cause production of an electron-positron pair. The positron annihilates almost always within the detector with an other electron by emission of two photons of 511 keV. One or both of these annihilation quanta can escape from the detector either completely or after Compton scattering. Thus, this effect causes a complex spectrum with three discrete peaks at E_γ , $E_\gamma - mc^2$ and $E_\gamma - 2mc^2$.

2.3 Compton suppression

2.3.1 Background contributions

The detection of low intensity peaks is often complicated by background continua caused by higher energy radiation. Even the high-resolution large-volume germanium detectors as used in the present experiments suffer from the fact that a large fraction of the incident gamma radiation is subject to Compton scattering. Already at 140 keV the Compton cross section in Ge equals the photoelectric cross section. At 400 keV the ratio is 10:1 and above 1 MeV the factor exceeds 100. Of course multiple processes occur: the major fraction of the counts in the full energy peaks for γ -rays above 140 keV originates from them.

Below we summarize processes leading to continua:

- 1) Compton scattering, where the scattered photon leaves the germanium detector.
- 2) Compton scattered photons escaping after a second Compton scattering. This effect causes a bump between the Compton edge and full energy peak as shown e.g. in fig. 2.3.
- 3) Gamma rays Compton scattering out of inactive material into the active part of the detector.
- 4) Gamma rays that Compton scatter out of active detector material and are absorbed in the inactive part.
- 5) Compton scattering at material from the source or between the source and the detector.
- 6) Incomplete charge collection due to the escape of secondary electrons, or of the bremsstrahlung associated with them, from the active region of the detector,
- 7) Pile-up due to random coincidence summing. This effect can be observed on the high energy side of γ -ray photo peaks. The intensity depends on the detector count rate during beam bursts and the electronics used.

Suppression of these backgrounds is an effective means of enhancing the signal-to-noise ratio. In the cases 1 and 2 above, one can do this by capturing the escaping photons in a scintillator surrounding the basic one, and not accepting detector pulses in coincidence with those from that scintillator. This part of the background can not in this way be completely eliminated. Those γ -rays, which scatter at angles of about 180° escape through the entrance hole in the scintillator. These γ -rays correspond to the part in the Ge spectrum around the Compton edge.

The effect of Compton scattering at material from the source or material between source and detector can of course not be suppressed. Therefore, the targets in pionic atom experiments should not be too thick and preferably there should be no material between target and detector.

2.3.2 Compton suppression scintillation crystal design

The scintillation counter just mentioned must surround the Ge-diode and its cryostat. Simultaneous occurrence of signals in both the γ -ray detector and its scintillation shield is used as a veto signal to suppress part of the spectrum detected by the central germanium counter. The scintillation crystal must be shielded against radiation coming directly from the target. Often, this target emits simultaneously two or more gamma rays; if one were detected in the scintillation counters, the system would selectively suppress the other ones.

The detection efficiency of the scintillator depends on the material used. Earlier, NaI(Tl) was much used because of the high atomic number of I ($Z=53$) causing high photo cross sections, and its high density. Recently, BGO (Bismuth germanate, $\text{Bi}_4\text{Ge}_3\text{O}_{12}$) has come into use which is superior in both respects ($Z=83$, see also table 2.1). Its scintillation efficiency, however, is smaller by a factor of eight. For this reason BGO is less suitable to detect the low-energy γ -rays produced by large angle Compton scattering. A good detection efficiency for those rays can be obtained by applying NaI(Tl) around the entrance channel of the Compton suppression crystals (see figs. 2.1 and 2.2).

Table 2.1: Physical properties of BGO and NaI(Tl) [Har 86].

	maximum emission nm	decay time ms	index of refraction	density g/cm ³	conversion efficiency %
NaI(Tl)	415	0.23	1.85	3.67	100
$\text{Bi}_4\text{Ge}_3\text{O}_{12}$	480	0.30	2.15	7.13	12

Figures 2.1 and 2.2 illustrate the two varieties of the Compton suppression spectrometer systems that were used in the present experiments. The crystals in both have been manufactured by Harshaw Chemie, de Meern, The Netherlands. Fig. 2.1 gives details on the geometry of an asymmetric detector combination designed for the highest suppression at low energies. Forward scattered γ -rays lose little energy, therefore the Ge detector is not placed in the center of the scintillation crystal but more towards the source. This results in a high suppression in the low-energy part of the recorded spectrum. Fig. 2.2 shows a design developed with the purpose in mind to permit simultaneous use of six detectors close around a target. Its scintillator is a symmetric annulus, also a combination of BGO, and a front end of NaI(Tl). The disadvantage is the smaller suppression factor at lower energies: they are due to γ -rays scattering at small angles

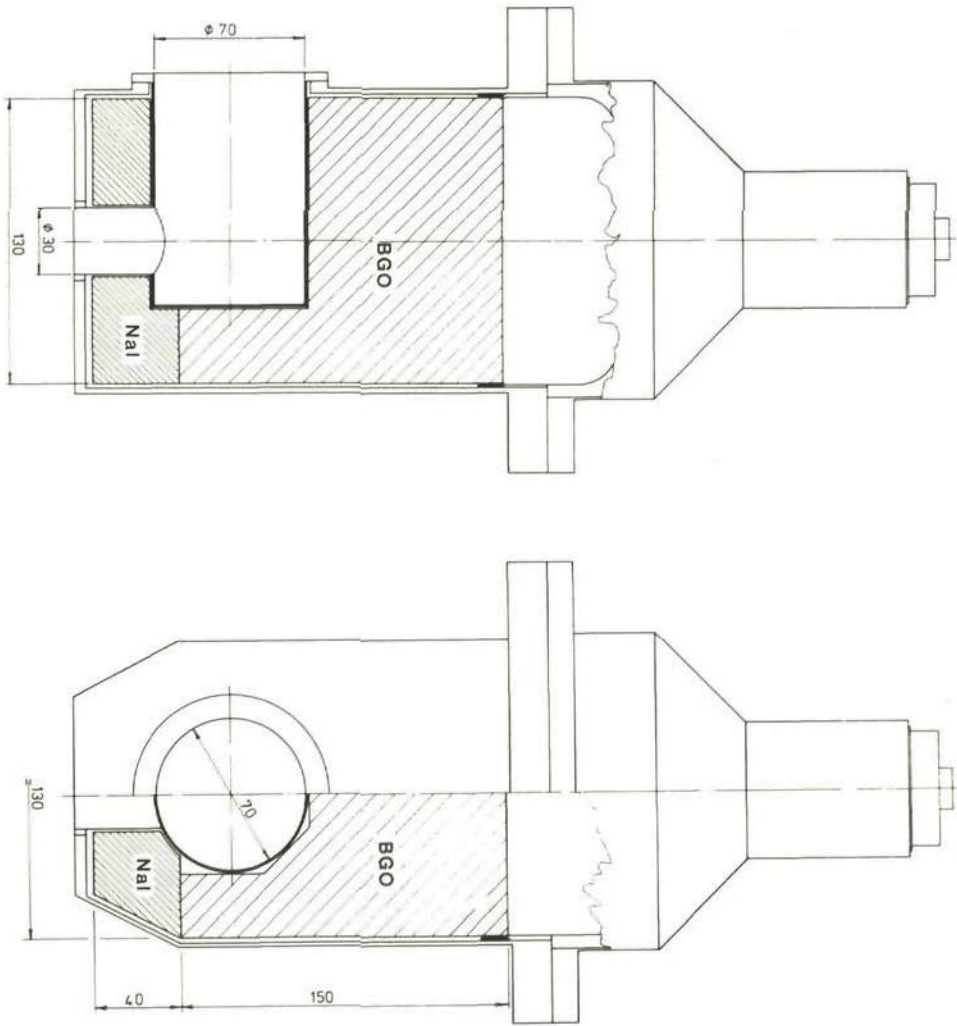


Fig. 2.1 Anti-Compton detector system with an asymmetric scintillator. It has a rectangular shape and consists of a BGO part and a NaI(Tl) part. The latter crystal is situated at the entrance side for the γ -radiation to be detected in an intrinsic large-volume Ge (n-type) detector placed in the $\text{\O}70$ mm well. A cylindrical hole machined through the thinnest part of the NaI(Tl) admits and collimates the radiation on the Ge detector. The axis of this hole is perpendicular to the axis of the well. The centre of the Ge-detector is 75 mm from the front side of the scintillation crystal. The scintillator is viewed by a $\text{\O}=127$ mm EMI photomultiplier.

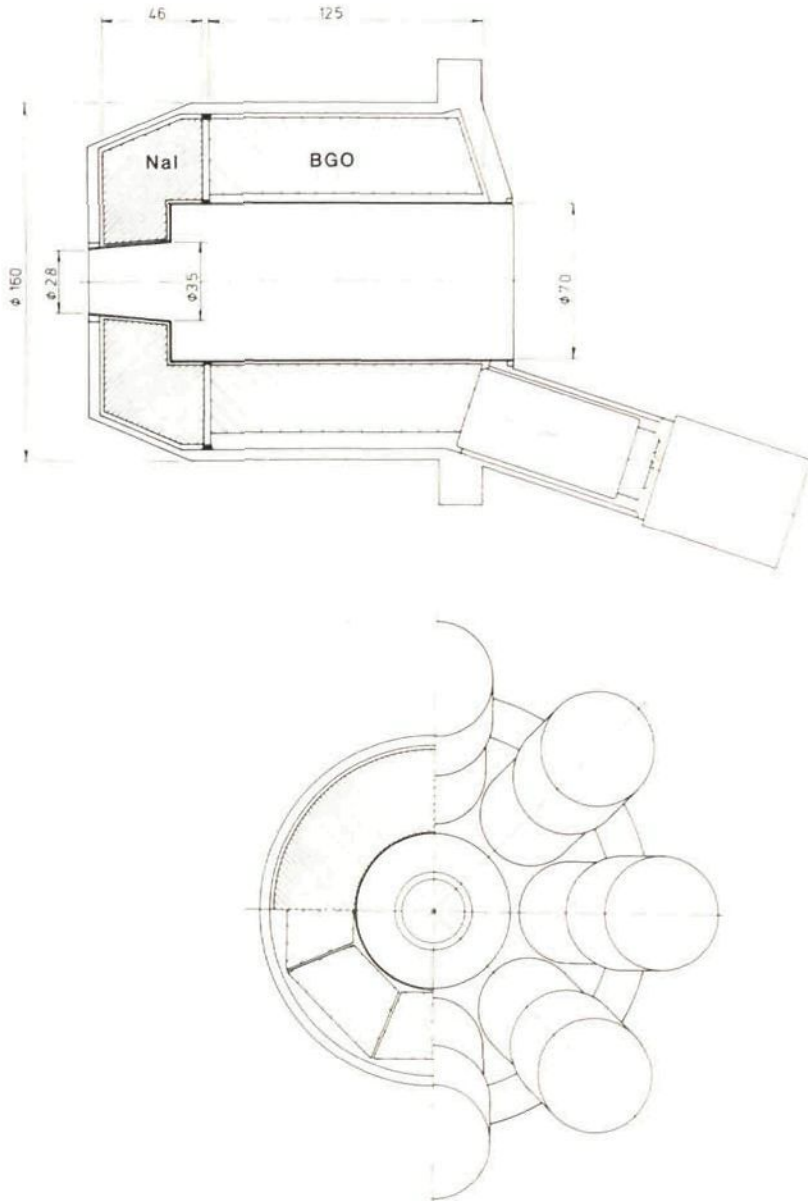


Fig. 2.2 Anti-Compton detector system with a symmetric annulus scintillator. It is also a combination of BGO and a front end of NaI(Tl). The entrance hole to collimate the incident γ -radiation on the Ge detector in the $\text{\O}70$ mm well has a conical shape over a length of 53 mm. The scintillator is viewed by eight Hamamatsu 2060 photomultipliers with $\text{\O}=38$ mm, mounted under an angle of 18° .

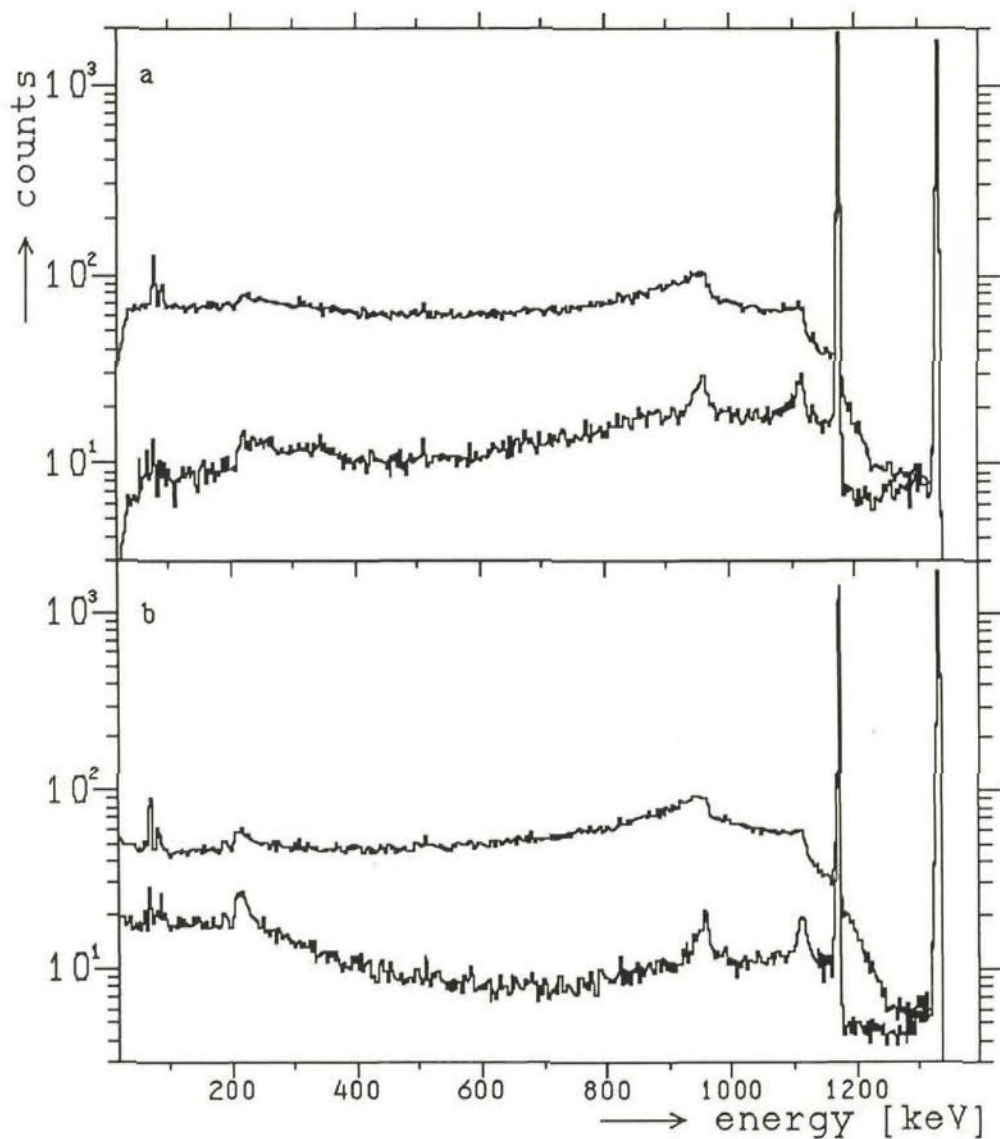


Fig. 2.3a Spectrum of ^{60}Co γ -rays measured with and without the asymmetric BGO shield. The upper curve is the total γ -spectrum from ^{60}Co , the lower curve contains only those events not accompanied by a BGO crystal signal.

Fig. 2.3b Same as above but with the symmetric BGO shield. Compared to the preceding spectra, this crystal has worse performance for energies from 0 to 400 keV but better from 600 to 1100 keV.

and thus leaving the system undetected via the entrance hole for the Ge detector. In the asymmetric design (fig. 2.2), these high energetic quanta are viewed by a thickness of about 13 cm of BGO material. This difference in performance between the two designs is illustrated in figure 2.3.

2.3.3 Compton suppression spectrometer set-up

Both the asymmetric and symmetric scintillation crystal designs are used in combination with large-volume, high resolution n type Ge detectors. Maximum performance of the Compton suppression spectrometer is obtained by keeping the mounting material and the amount of inactive material between the intrinsic ion-implanted n-type Ge diode and BGO crystal crystal to a minimum. The aluminum cap of the cryostat vacuum housing next to the detector has a thickness of about 0.5 mm. The important advantage of n-type Germanium over p-type is its 25 times higher tolerance against neutron damage.

High-purity n-type germanium detectors (GX) from ORTEC and CANBERRA with efficiencies ranging from 28 to 34 % and having full width at half maximum (FWHM) line width of about 1.9 keV at 1333 keV (because of high count rate this can deteriorate to 2.5 keV under beam conditions) were used to detect the cascade of pionic X-rays and nuclear γ -rays following pion absorption in the target.

An important quality factor is the peak-to-Compton ratio, obtained by dividing the peak height by the average number of counts per channel at the minimum height of the Compton continuum. For a large-volume high-resolution Ge detector as used in the present work, the ratio is about 40. The Compton suppression factor, defined as the ratio of the peak-to-Compton ratios in the single spectrum and the anticoincidence one, usually is approximately five in the present experiments (see fig. 2.3).

2.4 Neutron time-of-flight discrimination in γ -ray detection

A list of the levels excited by the $(n,n'\gamma)$ reaction in the Ge detector is provided in table 2.2. Even if these levels deexcite by more than one gamma ray, their chance of being absorbed in the detector is so large that the peaks seen correspond to level energies rather than to γ -ray energies. The elimination of this background is essential in the cases of pionic Ta and Re because the 1040 keV line in ^{70}Ge is situated next to the pionic $4f - 3d$ complexes in both spectra.

We reduce the effect of neutron induced γ -rays by time-of-flight techniques. The Ge detectors, surrounded by their BGO shields, are placed at a distance of about 60 cm from the target. This

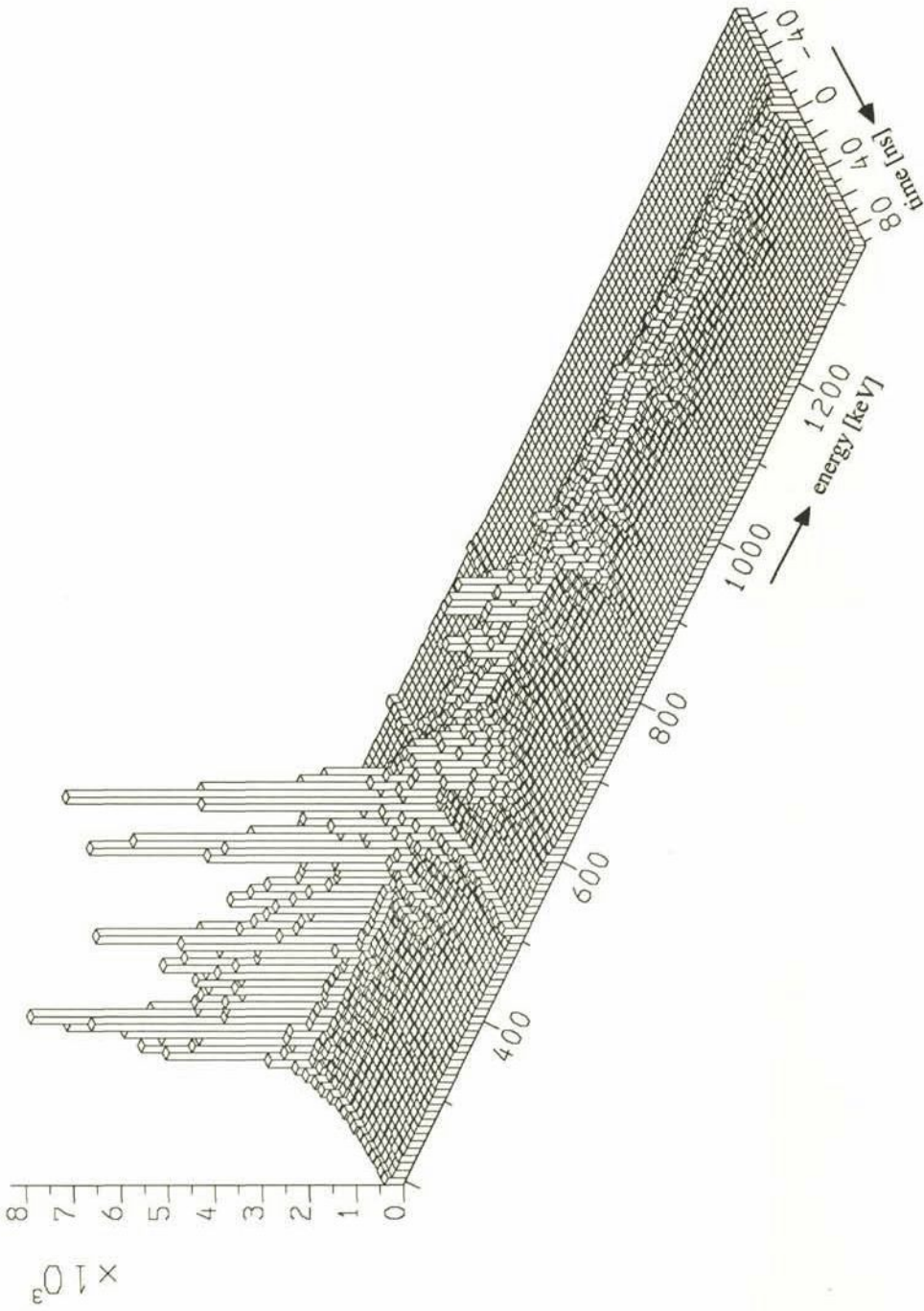


Fig. 2.4 Three dimensional spectrum versus energy and time in pionic Tantalum. The scales are keV and ns respectively. Clearly seen are e.g. the delayed 595 keV and 1040 keV lines. The 424 ns delayed 691 keV is still rising in the time interval considered. The 511 keV annihilation line arrives from different positions and, therefore, with a scale of delays.

permits discrimination between photons and neutrons by recording the time interval between the stopping of the pion in the target and the detection of the γ -rays in the Ge detector. Typical flight times over this distance for neutrons of 1 to 100 MeV are 72 and 8 ns, respectively, compared with 2 ns for photons. The time resolution for the large-volume high-purity Ge detectors at energies above 550 keV amounts to typically 10 ns FWHM so that neutrons can effectively be suppressed by cuts in the time spectra. As shown in the three dimensional graph (fig. 2.4) where intensity is plotted versus energy and time, the delayed neutron induced structures are well separated from the prompt X- and γ -rays.

Table 2.2: Neutron induced γ -emitting levels (in keV) in Ge isotopes.

energy	562.92	595.88	691.55†	834.14	868.0	1039.60	1108.45
isotope	76	74	72	72	73	70	76
energy	1204.31	1215.56	1410.08	1464.12	1482.58	1539.06	1708.15
isotope	74	70	76	72	74	76	70

† This level has a lifetime of 424 ns.

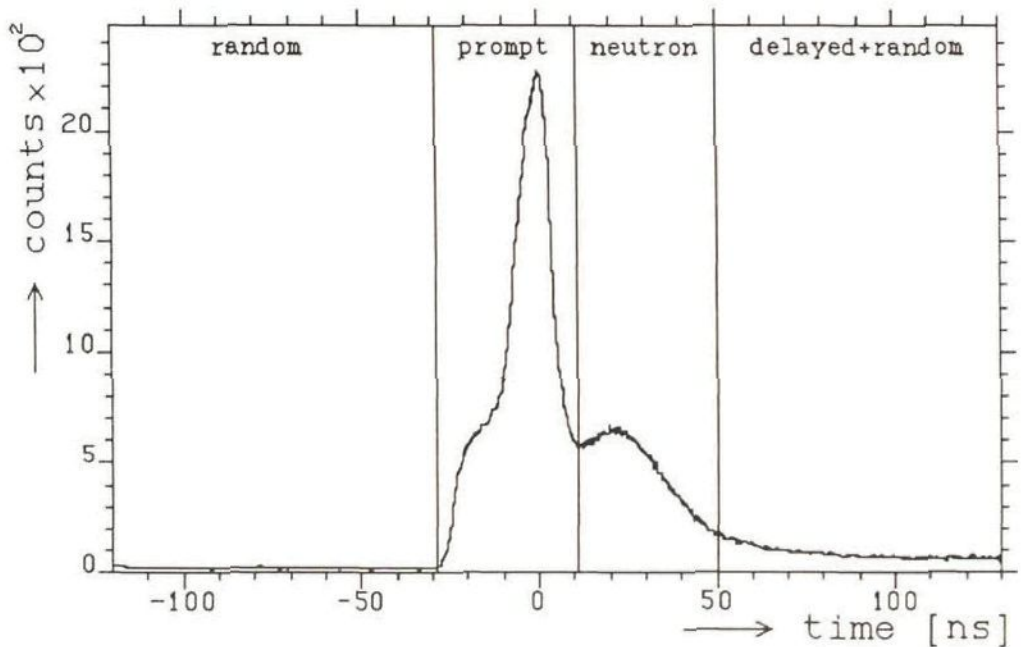


Fig. 2.5 Time spectrum of the γ -rays versus pion-stops. This time spectrum is integrated over all energies and thus includes delayed transitions, partly due to neutron time of flight.

A typical time spectrum is shown in fig. 2.5. The bump at ≈ 20 ns corresponds to gamma rays produced by $\text{Ge}(n,n')$. At times larger than 80 ns, the spectrum has a higher count rate than for less than -30 ns, where only true random events are present. This extra background is produced by γ -ray transitions with long lifetimes (notice eg. the 692 keV line in ^{72}Ge with $\tau = 424$ ns lifetime). Neutron damage in the detectors give rise to pulse shapes having slower rise times. This causes the tail at -20 ns of the prompt peak. Several authors [Mat 80, Kas 82] have described this pulse shape dependent effect and give methods how to utilize it for avoiding deteriorated resolution in the energy or the time spectra. Using the method of Matsushita et al. [Mat 80] on the prompt peak we could thus improve the FWHM of the energy spectra from 2.7 keV to 2.5 keV at around 1 MeV. By selecting suitable windows on the time spectrum, shown in fig. 2.5, we effectively separate the prompt spectra from the neutron induced γ -rays; see fig. 2.6.

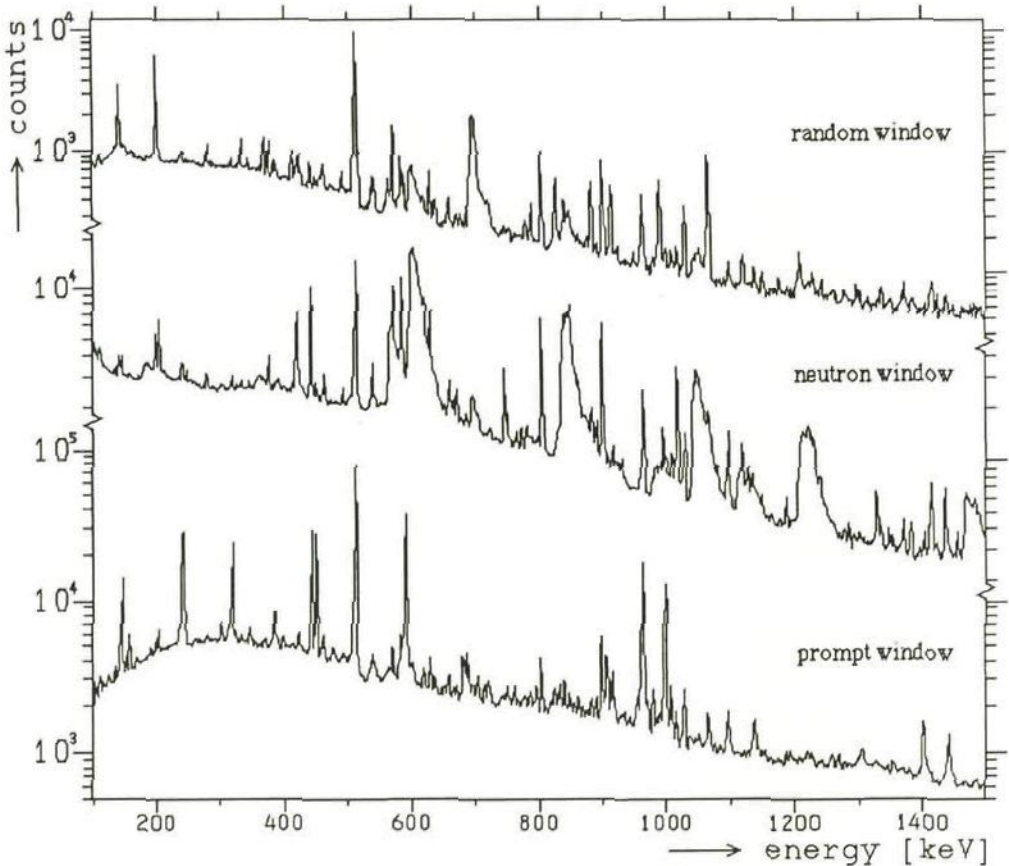


Fig. 2.6 Prompt, delayed and random spectrum of pionic ^{209}Bi . In the delayed spectrum clearly the neutron induced γ -rays in Ge and Al (from the detector cap) are recognized.

2.5 Experimental and electronic set-up

Measures were taken to optimize the number of pions stopped in the target. The number of incident pions increases with increasing energy setting of the pion channel. In order to stop them in the (thin) target, their energy has to be reduced (by absorbers of graphite or beryllium) to a low value. For high incident energy, the range spread is large, which means that a smaller percentage of the incident pions is stopped in the target. The optimum pion beam setting corresponded to an pion momentum $p = 100 \text{ MeV}/c$; then approximately 10^6 pions could be stopped per second.

An experimental area with a low background of neutrons and γ -rays should be chosen such as the $\mu\text{E}4$ area at the Paul Scherrer Institute (PSI, formerly SIN). This area includes a superconducting solenoid with a magnetic field of up to 4 T and three bending magnets with the necessary quadrupoles for beam focussing purposes (focus: $2 \times 2 \text{ cm}^2$). This lay-out permits to avoid unnecessary background radiation, as produced in beam defining slits.

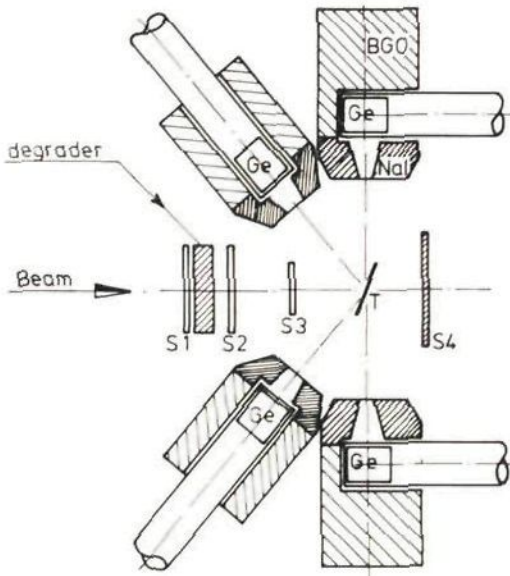


Fig. 2.7 Experimental set-up for the measurement of pionic X-rays. Two symmetric and two asymmetric BGO Compton suppression spectrometers are placed at a distance of about 60 cm around the target. The incident beam is recorded by the plastic (NE102A) scintillators beam telescope $S_1 - S_4$. S_1 and S_2 have dimensions $150 \times 130 \times 5 \text{ mm}^3$, S_3 , used for time definition of incident beam, is smaller ($100 \times 100 \times 3 \text{ mm}^3$), S_4 , used as veto, is larger ($250 \times 250 \times 7 \text{ mm}^3$).

In fig. 2.7 the essential parts of a typical set-up are given. The pion telescope, consisting of the scintillation counters S_1 through S_4 signals by $S_1 \times S_2 \times S_3 \times \bar{S}_4$ that a pion has stopped in the target. The counters S_1 and S_2 define the incident beam, S_2 shows a pion coming through the degraders and no signal in S_4 that it has been stopped in the target. The timing of the pion stop is defined by S_3 .

Care was taken to prevent pile-up in the pion stop signal in a time interval of about 150 ns either before or after any pion stop, to avoid ambiguities in the recording of the time spectra. The electronics then yields a veto signal that prevents recording any event coincident with such a pair of pions by the data acquisition system. In this way, the time spectra were free from ambiguous events as one pion causing the start of the time-to-amplitude converters (TAC) and another pion the γ or X-ray transition to be detected in the Ge detector.

The energy signals from the preamplifiers of the detectors are fed into Canberra 2021 spectroscopic amplifiers in combination with Canberra pile-up rejectors. These pile-up rejectors, using the preamplifier output as a timing input, are capable of discriminating between two events separated by less than 500 ns. The output signals from the main amplifiers are then gated such that the analog to digital converters (ADC's) only receives signals resulting from a single energy event in the detector during the processing time of the spectroscopic amplifier. The pile-up rejectors are essential in high count rate experiments such as ours. They improve the peak shapes and reduce the pile-up background by an order of magnitude.

The timing signals from the preamplifiers are fed via pulse shaping timing filter amplifiers (TFA Ortec 474) into constant fraction discriminators (CFD Ortec 934). The ADC's are gated with the CFD outputs in anticoincidence with the Compton suppression scintillation crystal signals. The event trigger is the coincidence of the ADC gate with a pion stop signal. An electronic scheme, which was used with only minor modifications in all pionic and muonic experiments is given in fig. 2.8.

A routing interface has been developed for successive storage of the digital output of Laben 13-bit ADC's into selected parts of 16K CAMAC histogramming modules and, if an event trigger is applied, simultaneously into four 64-words deep (16 bit) so called first in first out (FIFO) CAMAC modules. In this way it is possible to accumulate on-line single spectra and, at the same time, write coincident data in list mode on magnetic tape under computer control [Ach 85]. The digital computer interfacing part of the electronics is shown in fig. 2.9.

At each event trigger two words of each 16 bits, an energy and a time, per detector are written on tape. The data for experiments with two detectors (four words per event) are accumulated in blocks of each 510 events and written on 800 BPI (bits per inch) tapes. One such tape can contain 4750 blocks which is equivalent to 2.4×10^6 events. Each of our experiments produced between 50 and 100 tapes with data.

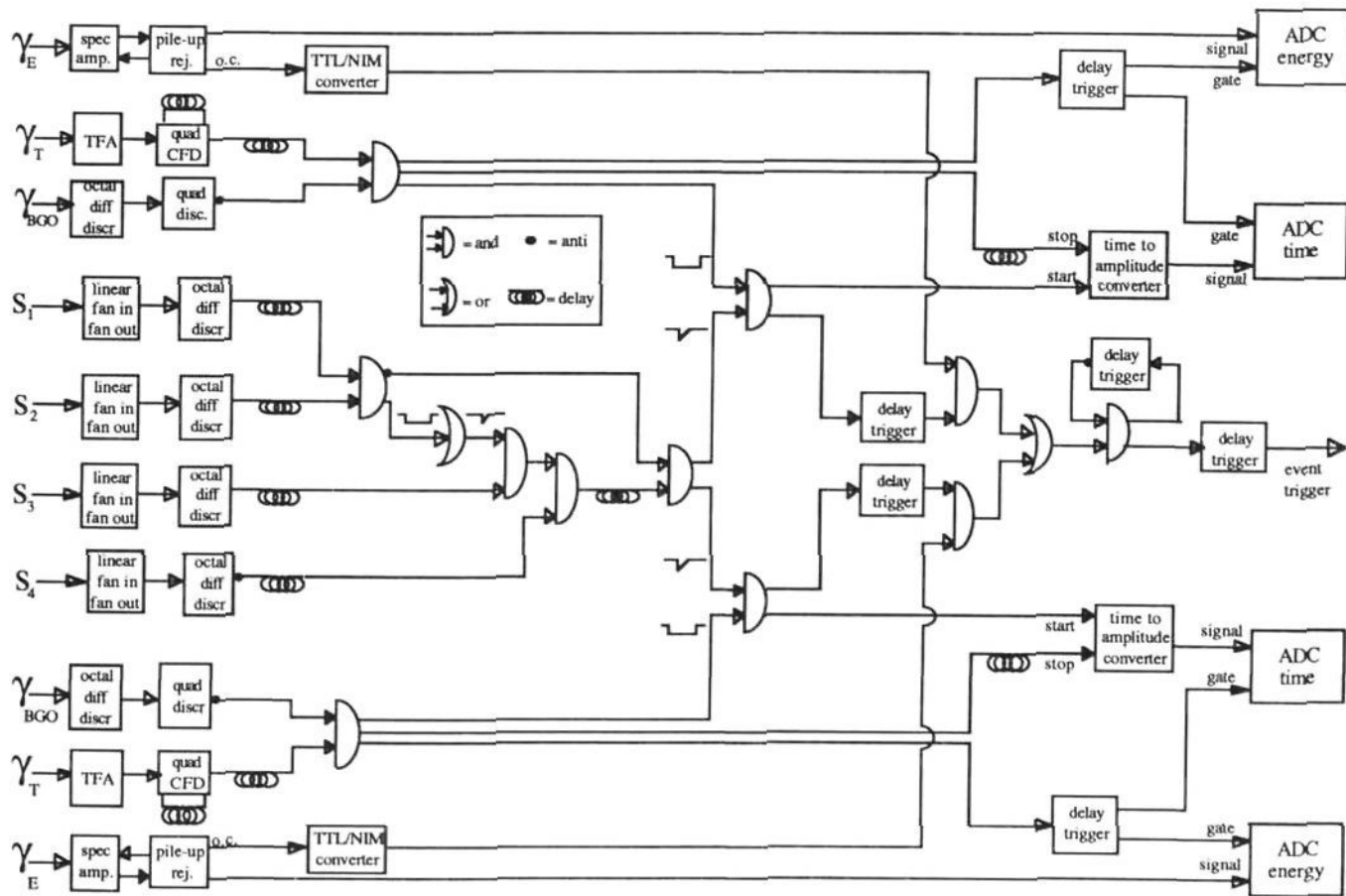


Fig. 2.8 *Electronical set-up for an experiment with two anti-Compton spectrometers. This electronics allows accumulation at high speed of information on pulse heights and time differences for each detector. The event trigger signals that a pulse height not vetoed by the anti-Compton shield, and a corresponding time of arrival are being presented.*

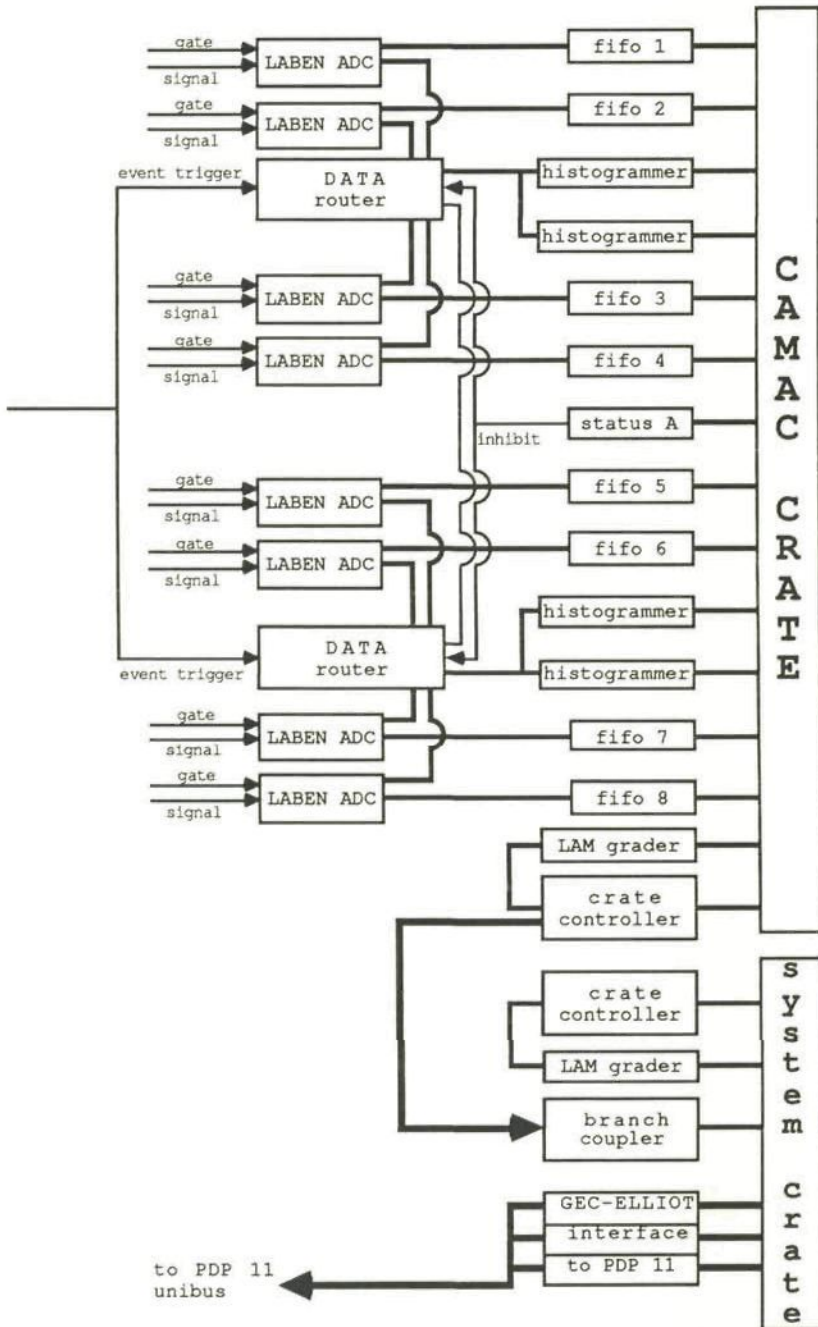


Fig. 2.9 Digital part of the electronics from ADC's up to the computer. The figure shows a set-up for an eight ADC coincidence experiment.

(The next paragraph has been reproduced from Nuclear Instruments and Methods in Physics Research A239 (1985) 556-561 North-Holland, Amsterdam.)

2.6 Reprint:

GENERAL-PURPOSE FAST CAMAC SOFTWARE FOR PDP-11 COMPUTERS

Cornelius T.A.M. DE LAAT

Nationaal Instituut voor Kernfysica en Hoge-Energiefysica, sectie K, Amsterdam, and Technische Hogeschool, Delft, The Netherlands

Johan G. KROMME

Interuniversitair Reactor Instituut, Delft, The Netherlands

Received 1 April 1984

A set of easy-to-use general purpose software routines for data acquisition in experiments using a GEC-Elliot CAMAC interface is described. The software concerned is based on Digital's IAS real-time operating system and consists of a fast multi-user CAMAC driver, a number of service routines and a FORTRAN library of user-friendly subroutines. The multi-user approach allows several data acquisition programs to be run simultaneously on different terminals. The CAMAC driver supports direct memory access channels, lists and loops of N-A-F functions (software emulated data-channel) and single module operations. Typical data transfer rates on a PDP-11/34 are 150K words per second for hardware direct memory channels and 40K words per second for software lists and loops. An example of application of this software in pionic- and muonic-atom experiments at NIKHEF-K in Amsterdam and in muon-induced fission experiments at SIN-Villigen, Switzerland is given.

1. Introduction

1.1. Design goals

For the growing demand of computer automated measurements and control of nuclear experiments at the Interuniversity Reactor Institute at Delft it became necessary to implement read-out software on a PDP-11/70. As an interface we use the GEC-Elliot CAMAC hardware. The basic design goals were to implement a data acquisition and control system that is (1) user-friendly, (2) safe to use, (3) flexible and (4) has the highest possible data acquisition rate. Point (1) implies that it must be possible for a user to write the control software in a commonly accepted "high level" programming language (such as FORTRAN) instead of assembler. With respect to point (2) it should be noted that the system must be safe-guarded against (unintentional) misoperation at any hardware or software level. With respect to point (3), the hardware must be accessible independently of the position of the module in the crate, and commands must be specified dynamically or changed without relinking the controlling process. Related to this is the last point: depending on the type of data one must be able to choose the most efficient transfer mode.

1.2. The choice of the system

Partly for historical reasons (previously a PDP-9 with an in-house developed CAMAC system was in use)

a combination of a GEC-Elliot CAMAC system and a PDP-11/70 running under RSX-11-D (now IAS) was chosen. Besides this, a multi-tasking, multi-user real-time operating system, such as RSX, offers the possibility of sharing computer hardware among many users with many experiments. The selected components are of modular design. For instance: the GEC-Elliot CAMAC system supports the use of several controllers (including direct memory access controllers) and can address up to 50 different crates. The same applies to the PDP-11/70 hardware, it is modular in that it can be expanded to satisfy growing demands.

1.3. Principles for implementation of the driver

A pre-requisite for the multi-tasking sharing approach is the development of a central monitoring program (called a device driver in the IAS operating system) to control the use of units in the CAMAC hardware system. Contrary to a system in which only one task is in direct control of the CAMAC hardware and other tasks cannot interact without affecting the process, the driver in the multi-task system must emulate all interactions between the hardware and the related user software as if the user software had direct control. This involves the execution of CAMAC instructions, the initialisation of data transfers and the control of LAMs, and further the translation of special hardware conditions like LAMs to corresponding actions in the user task. Besides this, the driver has an administrative func-

tion in protecting CAMAC units against illegal access. The functions of the driver can be divided into three groups:

- 1) administrative; e.g. reserving a unit for a user, establishing a link between a LAM and an associated event;
- 2) direct action; e.g. execution of (a list of) AF CAMAC functions, starting a direct memory access channel, enabling a LAM;
- 3) triggering; e.g. translating the occurrence of a LAM to a specified action.

For security reasons LAM-graders are used to control the processing of LAMs. The driver controls these to prevent system hang-ups. Much attention has been paid to the integrity of the system - a crate or even a whole branch may be disconnected from power by whatever reason while other parts of the system remain unaffected. The communication between user software and the driver is established via so-called "QIO system calls". For FORTRAN users an easy-to-use subroutine package has been developed as an interface for these system calls.

2. The CAMAC subroutine package

2.1. General

As already indicated in sect. 1.2, all the operations on the hardware are emulated by the driver and accessible via simple FORTRAN calls. A number of additional actions are necessary due to the multi-tasking approach and the hardware protection through the use of LAM-graders. Several actions are complementary, e.g. reserving a module and releasing a module, enabling and disabling a LAM, starting a direct memory access data transfer and stopping it.

2.2. Administrative actions

Due to the multi-user environment it was necessary to implement a mechanism to protect CAMAC modules against illegal access. Therefore a CAMAC module can be reserved upon request for exclusive use by a certain task or a group of tasks belonging to the same user. The reverse action can also be specified - on exit or abort all necessary actions are executed to make modules accessible to other users again.

Variable areas of memory can be reserved for data storage or histogramming via the memory management directives of the operating system. Other actions involve the preparation of future events; a task can specify several triggering modes to be activated after the occurrence of the related LAM. Also a list of CAMAC instructions can be prepared for execution at system interrupt level. The interrupts are repeated until an array of data is filled or emptied.

2.3. Direct actions

One can select several different transfer modes for executing (a list of) CAMAC instructions depending on the transfer rate desired and the response time needed. The first and simplest way is to provide a list of (AF) instructions with the necessary data words inserted in between; Q and X responses are returned and set in the relevant AF code.

In this way, however, large data transfers will result in an inefficient instruction list. Therefore a second type of transfer has been implemented in which the data words are replaced by addresses of arrays containing the data words. In this case, the list of CAMAC instructions is executed repetitively until one or more arrays are filled, emptied or if a specified Q-response is absent. This method is used in situations where data are already present in a buffer and are ready for transfer.

The third type of data transfer is similar to the latter, differing only in that the list of CAMAC instructions is executed at system interrupt level each time a LAM occurs; until one or more arrays are filled, emptied or if a specified Q-response is not present. This method is used in situations where data are sampled and presented at random time intervals.

The fourth and fastest type of transfer is hardware-controlled via a direct memory access channel operating independently of the CPU. Only one instruction per interrupt is executed at a high repetition rate until an array is filled, emptied or some error condition occurs. Three modes of this hardware-oriented transfer are implemented: read mode (in which data are transferred from CAMAC to memory), write mode (in which data are transferred from memory to CAMAC) and histogram mode (in which data are read from CAMAC and are used as index in an array, the content at the given address then being incremented by one).

The last three types of data transfer normally effect arrays inside the user task. However, it is possible to select memory outside the range of the controlling task by creating so-called dynamic regions. The administration of the regions is done by the CAMAC driver. This facility enables the user to overcome the normal 32K user-area restriction of the PDP-11. The user retains fast access to the data via memory management directives. An example of all these types of data flows is shown in fig. 1.

Double buffering is supported for the last two types of data transfer; this is a feature which is to take place without interruption for setup of a new transfer. Thus, in a continuous data stream no data will be lost. To use this facility, one simply has to specify a second transfer while the first one is executing; after execution of the first, and during execution of the second at system interrupt level, a third transfer may be specified.

A special direct action is the enabling of a LAM.

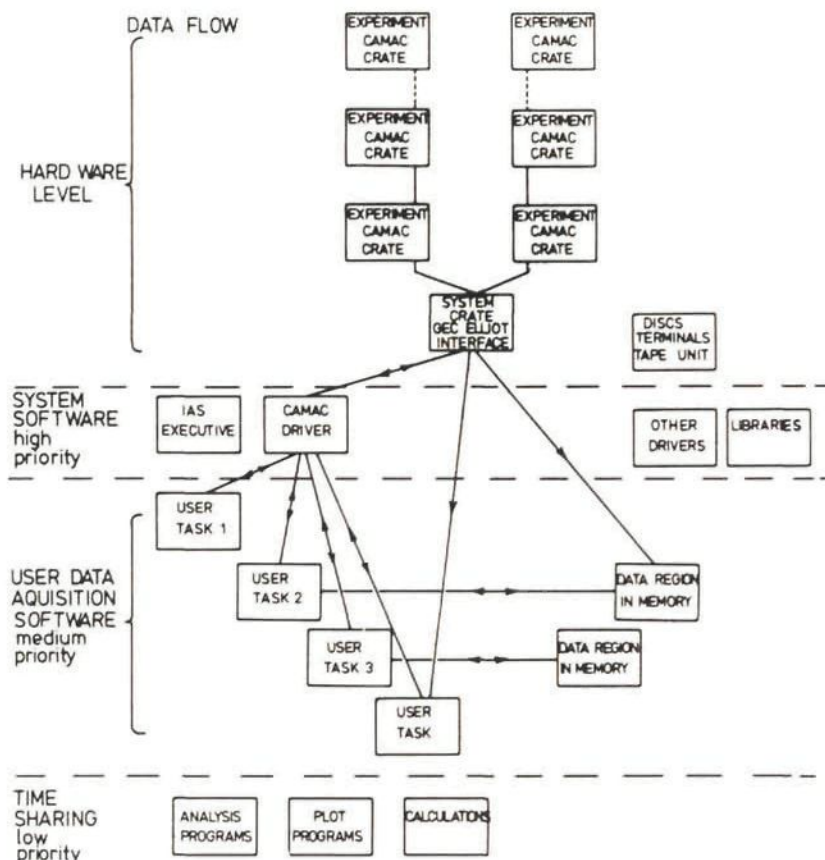


Fig. 1. Data flows in hardware and software system.

With this command the LAM generated by a CAMAC module is allowed to be handled by the hardware, so that an interrupt can be produced. On the other hand, LAMs that are not allowed cannot hang the computer.

2.4. Triggering of events

The CAMAC subroutine package utilizes the full set of trigger mechanisms supported by IAS. The triggers are activated on the occurrence of a LAM, when a system level transfer or a direct memory access transfer has been completed. The trigger tools are basically:

- 1) requesting a task,
- 2) resuming a suspended task,
- 3) sending a message,
- 4) setting an event flag.

5) software task interrupt.

The user task may specify any combination of these facilities, but it is the responsibility of the user task to choose the right combination and to select the appropriate status. This is necessary for triggering a task, i.e. setting an event flag only makes sense if a task is waiting for it.

A special feature for FORTRAN tasks in this concept is the possibility of triggering the task by a software-initiated interrupt (to be distinguished from system-level interrupts), normally only available to assembler-oriented tasks. If some basic rules are obeyed, it is possible to interrupt a running task, execute a specified subroutine and continue after the return statement with the execution of the interrupted program. One rule arises from the fact that the FORTRAN compiler does

not generate re-entrant object modules for I/O operations so it is not possible to do FORTRAN I/O at normal and interrupt level at the same time. These restrictions can be overcome by using non-standard, QIO-based I/O routines rather than standard FORTRAN I/O statements.

3. Historical and numerical data

The system described here has been implemented on a PDP-11/70 with the full CAMAC package and has been in use since 1976. The same system was installed on a PDP-11/44 in 1981, and on a PDP-11/34 in 1982. These packages are now in use at IRI-Delft, NIKHEF-Amsterdam and in some experiments at SIN-Villigen, Switzerland. A subset of the CAMAC package is implemented under the RSX-11-M operating system. Versions based on interfaces from HYTEC and KINETICS have also been developed.

The data achieved with the package is dependent on the type of transfer mode and of course on the type of CPU used. Basically there are four types of transfer modes. Combined with the appropriate waiting state in the first two modes, the relevant times for a PDP-11/70 are given in table 1. Typically this means for the first type a maximum of 2K instructions per second, for the second type 40K per second and for the third type 25K per second, whereas with the fourth type a transfer rate of 200K per second can be achieved.

4. Data acquisition and analysis programs

4.1. Types of experiments

In this section we describe an application, written to perform data acquisition and analysis in various experiments at different accelerators. This software is capable of transferring 30K words/s from CAMAC to tape without on-line analysis.

The software was developed mainly for spectroscopic coincidence measurements. Normally the events consist of several ADC-words (analog-to-digital converter),

Some usually represent energies, some time-to-amplitude converter outputs. Some of the experiments are pionic experiments at NIKHEF in Amsterdam by d'Achard van Enschut et al. [1] and muon-induced fission experiments at SIN-Villigen, Switzerland, by David et al. [2].

4.2. Available hardware and requirements to handle software

The available hardware consists of a PDP-11/34 with floating point processor and 1 Mb SYSTIME EMMU memory. As peripherals two RL02 disc units, a 4-fold Quadrasync terminal interface, a tape controller with two tape units, and a GEC-Elliott/Fischer CAMAC interface consisting of a PT11C and a PT11D unit are available. The CAMAC software does not use an interrupt vector generator. The required LAM mask operations are done in LAM graders which must be present in every crate where a LAM can be generated.

4.3. Set of developed programs

For the experiments we developed a set of programs, which work together to perform the entire measurement. This set consists of:

- 1) the main program MESA,
- 2) the program RESEND to receive and send commands,
- 3) the program DSCWRI to process scaler readings,
- 4) the program LGB as a logbook keeper,
- 5) the program PLO performing the plotting of the spectra.

The main control is done by the program MESA. This program contains the tables of initialized hardware and spectrum buffers. It services the start, stop and interrupts, writes the data on tape and performs on-line analysis of the data. It also reads the scalers and sets up a message for the program DSCWRI to dump these data. In this way, the processing of the readings of the scalers cannot interfere with the main measurement, since DSCWRI is only a time-sharing task. For memory-management reasons the command input during measurement is not done directly in MESA but via the program RESEND.

Messages from MESA are not only typed on the terminal but also sent to the program LGB where they are written in a logbook file including date and time.

To inspect the analysed spectra the program PLO is used. It will plot spectra (the data of which are located in memory, CAMAC LeCroy histogrammers, or files on disk) in two dimensions or a three-dimensional view, scatter-plots and so forth. Its capabilities include calibrations, listings of channel contents and sums, and different lines of view for the presentation of three-dimensional spectra.

Table 1
Timing of the different data transfer modes

	Context overhead [μ s]	Driver overhead [μ s]	Interval time [μ s]
1 wait, event, transfer	800	400	50
2 wait, event, array transfer	800	600	10
3 system level transfer	0	150	10
4 direct memory access	0	0	5

4.4. MESA program

Currently MESA can cope with up to 12 ADCs connected to CAMAC via CERN first-in-first-out fifo registers type 175, 6 LeCroy CAMAC memory histogrammers 3588 each containing a memory of 16K 24-bit locations, 16 scalers type SEN 2003, and one CAMAC Status A register CERN type 155. A typical electronics setup is shown in fig. 2. The data, measured in list mode by the ADCs can be analysed in up to 18 spectra, each having a maximum size of 8K channels. These spectra are located in the main memory of the computer and consist of data regions. Various conditions and windows can be set on the data to decide whether or not to sort the data.

In the initialisation stage of an experiment, the user can specify which part of the maximum configuration described above he wants to use in a question-and-answer session. He has also to define where the modules are located in the CAMAC crates. The locations and the number of the modules can vary from experiment to experiment without relinking the MESA program. This gives the possibility of running MESA on several terminals, so that various experiments can be done simultaneously on the same computer. This is possible because the addresses of the modules are not fixed in the measuring program, and because the CAMAC driver is multi-user oriented.

When one starts an experiment by an initialisation, the program asks the CAMAC driver if the desired CAMAC stations are available, and if so it claims them

so that no other measurements can interfere during the run.

Data-taking in MESA is performed by a LAM trigger followed by software read-out of the CAMAC units. For this purpose an array is filled with a list of N-A-F functions which define the way in which the CAMAC will be read out. The list is put together in the initialisation stage and can vary in principle for every experiment. Two checks on the validity of the data are built into the program. First it is verified that the ADC words in the first-in-first-out registers belonging to the same event are still contiguous.

Since we normally measure with 8192-channel ADCs, only 13 bits are used in every 16-bit word. In the data router [3] (see fig. 2) a 3-bit counter was built in to count the events. These 3 bits are added to all ADC data simultaneously and tested in the interrupt routine.

A second check is purely software-wise and tests whether one or more bits in the input words are never set; if so, this indicates that a cable to one of the ADCs is defect.

Since we perform experiments with a multi-detector spectroscopic system, we must be able to increment many large spectra at relatively high speed. This was accomplished by the use of memory management directives, supported by the IAS system.

An address window of 8K is reserved within the measuring program MESA for mapping to the area in the computer memory where the spectra are located. Every time a block of data is to be analysed, the program connects the 8K address space to the first

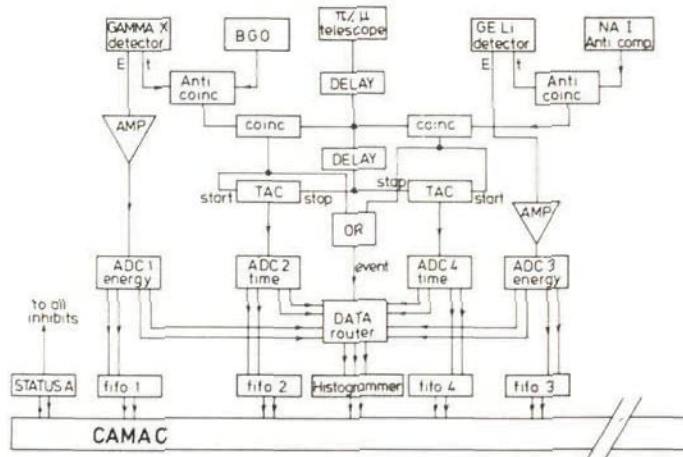


Fig. 2. Electronics setup for the pionic atoms measurement.

spectrum, analyses the contents of the data block concerning this spectrum, remaps to the next spectrum and so on. Typical analysis speeds are 20.000 events/s per spectrum including mapping and checking for overflows.

4.5. Non-buffered data acquisition

Recently a data acquisition program for a completely different experimental setup was implemented. In this experiment it was necessary to read out a number of LeCroy TDCs (time-to-digital converters), a number of LeCroy ADCs and 32 scalers all situated in CAMAC. The program had to read out in total 173 words out of twelve modules. As the data do not first enter some kind of fifo, the transfers should be done immediately after the occurrence of the LAM. This problem is solved by utilizing the third type of transfer (system level). The rest of the program has a similar structure as MESA. Maximum data transfer rates achieved are 23000 words/s on a PDP-11/34 (173 words are transferred per LAM interrupt).

5. Conclusion

We have developed a fast, reliable multi-user CAMAC driver, which has proven its usability in several

completely different environments. It is used on a PDP-11/70, which services 14 CAMAC crates from four different user groups, who simultaneously perform small, moderate and large experiments with it. This system uses 8 direct memory channels to perform spectrum increment measurements which do not need CPU time in this way. The CAMAC package is also in use on a computer specially dedicated to one experiment to perform high speed data acquisition.

This work is part of the research programme of NIKHEF-K at Amsterdam and IRI at Delft, made possible by the financial support from the Foundation for Fundamental Research on Matter (FOM) and the Netherlands Organization for the Advancement of Pure Research (ZWO).

References

- [1] J.F.M. d'Achard van Enschut et al., Phys. Lett. 136B (1984) 24.
- [2] P. David et al., in preparation.
- [3] J.F.M. d'Achard van Enschut et al., submitted to Nucl. Instr. and Meth.

2.7 Data reduction

The data reduction is done with the same software as used to perform the experiment. The first step in the analysis is to check the different tapes from an experiment carefully for changes in the time and energy calibrations of any ADC. In case of changes, a specially developed off line re-binning program is used to combine the spectra. Also changes in peak to background ratio and full width at half maximum (FWHM) for some prominent γ -rays are monitored. If a change in any of these parameters is observed, the data set is further treated independently. A time spectrum is then accumulated for each independent data set from each detector such as shown in figure 2.6. For these operations not all the data are analyzed but rather a few hundred blocks from every tape. In every time spectrum, windows are determined to disentangle prompt, delayed and accidental events. All the tapes are then analyzed to get the corresponding energy spectra for each detector. The results are summed to get the final spectrum.

2.8 Fit program

2.8.1 General structure of the program

For the evaluation of the pionic gamma spectra we developed a flexible interactive fit computer code [Laa 88]. Line positions, widths and intensities are obtained by fitting the experimental spectra with a list of functions representing lines, Compton continua and continuous background. The user of the program can add and delete various function to and from it. The functions mostly encountered in nuclear γ -ray spectroscopy are Gaussian with tails, Gaussian convoluted with Lorentzian shape etc., and several types of backgrounds, like linear quadratic, exponential and step functions. Other function shapes can be defined and build into the program easily. Some function types can be defined as hyperfine components (see 2.8.3). The computer code uses the fitting routines grids, gradls, chifit and curfit described by Bevington [Bev 69]. The fast fit subroutine curfit uses an algorithm developed by D. Marquard [Mar 63].

The program developed is more general than necessary for fitting γ -ray spectra, and indeed in use for several other purposes like fitting life time spectra, antiprotonic X-rays, beam momentum spectra and level schemes.

2.8.2 Peak shape representation functions

The full-energy γ -ray peaks are fit with a line shape composed of a Gaussian and an exponential distribution on both sides of the peak. The transition points between Gaussian and exponential line shape on the left and right hand side are chosen in terms of the FWHM of the Gaussian distribution shape to make them independent of the calibration of the energy-axis. The parameters of the exponentials are then calculated to preserve functional and differential continuity at the boundaries. This function shape Gaussian with tails is expressed in the following formula:

$$f_{\text{Gauss}}(x) = A e^{-\left| 4t_1 \left(-2 \frac{x-x_0}{w} - t_1 \right) \right| \ln 2} \quad \text{for } \frac{x-x_0}{w} < -t_1 \quad (2-4a)$$

$$f_{\text{Gauss}}(x) = A e^{-\left| 4t_h \left(2 \frac{x-x_0}{w} - t_h \right) \right| \ln 2} \quad \text{for } \frac{x-x_0}{w} > t_h \quad (2-4b)$$

$$f_{\text{Gauss}}(x) = A e^{-\left(2 \frac{x-x_0}{w} \right)^2 \ln 2} \quad \text{for } -t_1 < \frac{x-x_0}{w} < t_h \quad (2-4c)$$

where x_0 = position, A = amplitude, w = FWHM, t_1 and t_h are the distances from x_0 to lower and higher tail connection. Neglecting the tails seriously affects the χ^2 value and therefore would hinder a good evaluation of the quality of the line fits.

For pionic transitions a pure Gaussian distribution convoluted with a Lorentzian shape was used. As shown by Routti [Rou 69] and Batty [Bat 76], this convolution can be written in terms of the complex error function $\text{erf}(z)$ which can be computed reasonable fast using an algorithm given by Gautschi [Gau 69]:

$$f(x) = A \frac{\text{Real}\left\{ g \left(2\sqrt{\ln(2)} \frac{x-x_0}{w} + i\sqrt{\ln(2)} \frac{\Gamma}{w} \right) \right\}}{\text{Real}\left\{ g \left(i\sqrt{\ln(2)} \frac{\Gamma}{w} \right) \right\}} \quad (2-5a)$$

$$g(z) = e^{-z^2} (1 - \text{erf}(z)) \quad (2-5b)$$

$$\text{erf}(z) = \frac{2}{\sqrt{\pi}} \int_0^z e^{-t^2} dt \quad (2-5c)$$

were Γ is the FWHM of the Lorentzian shape. This method relies, however, on the assumption that the detector response function has no tails. The result of numerical integration of a Gaussian distribution with tails convoluted with a Lorentzian function has been compared to the above mentioned analytical method and no deviations bigger than 0.4% were found for tail parameters as we find them in our spectra.

An extra complication arises if a line occurs near a Compton edge of another strong line, as is the case in pionic ^{209}Bi . The shape of a Compton edge is represented by formulæ:

eq. (2 - 6 a,b,c) = eq. (2 - 4 a,b,c) and

$$f(x) = f_{\text{Gauss}}(x_0 - wr_l) e^{-\ln(2) \frac{x_0 - wr_l - x}{wh_l}} \quad \text{for } \frac{x - x_0}{w} < -r_l \quad (2 - 6d)$$

$$f(x) = f_{\text{Gauss}}(x_0 + wt_h) e^{-\ln(2) \frac{x - x_0 - wt_h}{wh_h}} \quad \text{for } \frac{x - x_0}{w} > t_h \quad (2 - 6e)$$

were r_l and r_h are distances to lower and higher triangle connection respectively and h_l and h_h are decay lengths of the exponential tails. The parameters in these functions are determined with the help of calibration lines (see table 2.3). In the particular case mentioned, we found that, neglecting such Compton contributions would give an as much as 5 keV larger value for the width of the pionic transition.

Table 2.3: Parametrization of Compton continua in relation to the corresponding full energy peaks. The function shape is expressed by formulæ 2 - 5 and 2 - 6. The energy in the table is that of the corresponding full energy peak. These data have been used to find the shape for the Compton continuum of the 1609 keV γ -ray occurring in the pionic ^{209}Bi spectra.

energy keV	Amplitude ratio	t_l	t_h	r_l	h_l	r_h	h_h	
1172	5.1×10^{-3}	0.054	0.70	3.28	17.3	0.56	6.5	1.58
1332	6.2×10^{-3}	0.054	0.70	3.28	17.3	0.56	6.5	1.58
2752	5.3×10^{-3}	0.065	0.70	2.66	17.8	0.63	11.0	1.69
4806	3.2×10^{-3}	0.065	0.65	2.60	17.5	0.63	10.0	1.05
1609	5.5×10^{-3}	0.060	0.70	3.0	17.5	0.60	7	

2.8.3 Hyperfine complexes

As described in chapter 3, quadrupole splitting of muonic and pionic atom levels causes a transition between them to be a hyperfine complex of a certain number of lines with strictly correlated (and known) intensities. Their positions with respect to the centroid of the complex are also known but for a common factor in the distances to the centroid. Also, these distances are so small that all components can be assumed to have the same shape. Thus, the whole complex can be described by just one parameter (the "hyperfine splitting") more than a single line.

The functional description of a hyperfine complex is

$$x_i = x_0 + \frac{rx_i * fs}{rx_2 - rx_1} + as_i \quad (2 - 7a)$$

$$a_i = A * ra_i \quad (2 - 7b)$$

$$f(x) = \sum_{i=1}^n ft(x_i, a_i, \dots) \quad (2 - 7c)$$

where $ft(x)$ is the function type for the members of the hyperfine complex, x_i and a_i are the position and amplitude of subpeak i , n is the number of subpeaks, rx_i , as_i and ra_i are the relative position, absolute shift and relative amplitude of subpeak i and fs is the fine structure splitting (usually the splitting between the two main components).

2.8.4 Step function

One notices that the distribution extending at the low energy side the full energy peak is higher than the distribution at the other side. It exhibits a kind of step function (see fig. 2.10). This effect is probably due to incomplete charge collection, and escape of bremsstrahlung from the germanium detector. Since pionic transitions may extend over 50 keV, the knowledge of the behaviour of the steps is essential. Neglecting them can significantly change the results of the analysis of the widths. If the step is underestimated, the width will usually be larger because the fit program will try to fill the hole with a function with long tails. In the special case of ^{209}Pb , neglecting these steps for the 1402 and 1440 lines would seriously affect the background fitted below the 4f-3d pionic X-ray complex, which would then turn out to be considerably broader. This feature at least partly explains the difference between our result and that of Olin et al., see section 4.2.1.3.

An additional point arises in the case of the radiationless transitions in muonic ^{237}Np (see appendix A) due to the low statistics in the coincidence spectra distributed over a large number of peaks. One only wants to know the intensity of the whole complex, thus we need not to fit the individual peaks. An accurate estimate for the background including the step, though, is essential. The step function is designed $S(x)$, the background without it $B(x)$, so that the total count rate is:

$$F(x) = B(x) + P(x) + S(x) \quad (2-8)$$

in which P is the collection of peaks. The step function is defined:

$$S(x) = S_f \int_x^{x_m} P(t) dt \quad (2-9)$$

where S_f is the step factor and x_m is a suitable position above the peaks. The advantages of defining the step in this way are:

- 1) it gives a straightforward algorithm which can be used on all peaks.
- 2) if the function $P(x)$ is unknown but the background $B(x)$ and the magnitude of the step $S(x)$ at a point below the collection of peaks are known, it is possible to make an iterative procedure to determine the stepfactor S_f and the integral of $P(x)$.

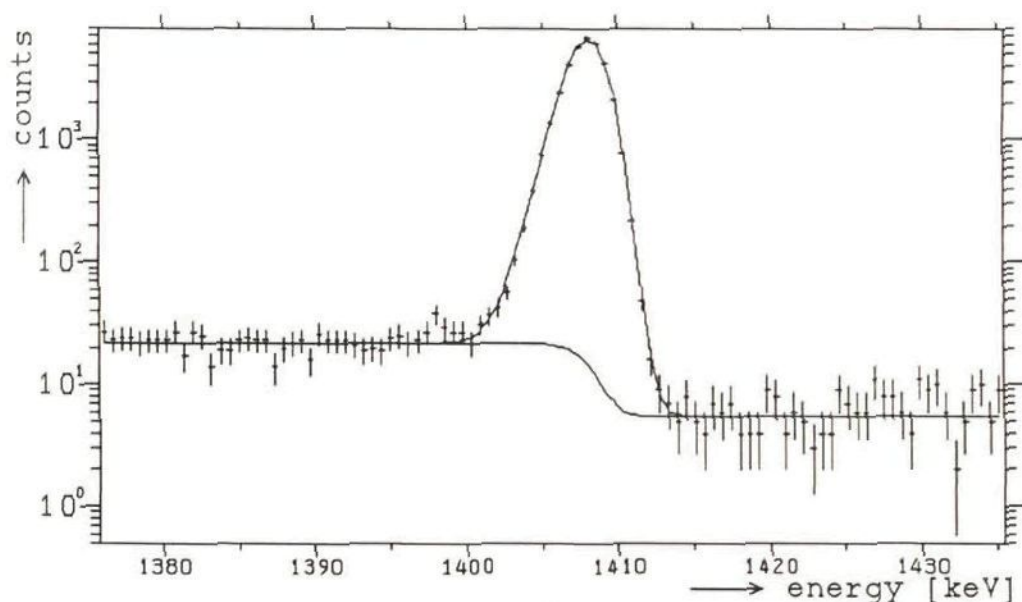


Fig. 2.10 The 1408 keV transition in the decay of ^{152}Eu plotted on a logarithmic scale. The step function is indicated by a solid line.

2.9 Relative efficiency calibration

The relative efficiency curve of the detectors has been obtained from calibration spectra, taken with radioactive sources such as ^{152}Eu , ^{133}Ba , ^{66}Ga (see fig. 2.11). The intensity ratios of the calibration lines in each of those sources are very well known, but the absolute intensity of each source is less accurately known. The errors in fig 2.11 correspond to the latter intensities, which explains that the calibration curve agrees better with them than could be expected from statistics alone. The obtained curve might therefore shift a little as a whole in vertical direction, but this will have negligible influence on the relative efficiencies.

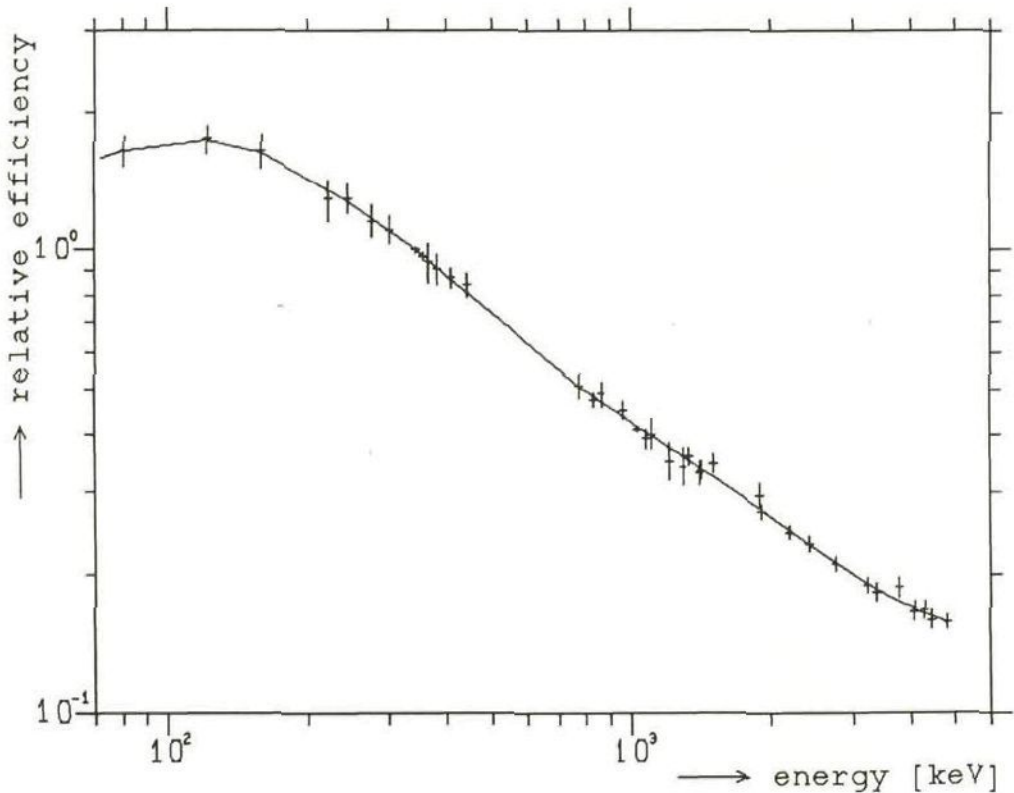
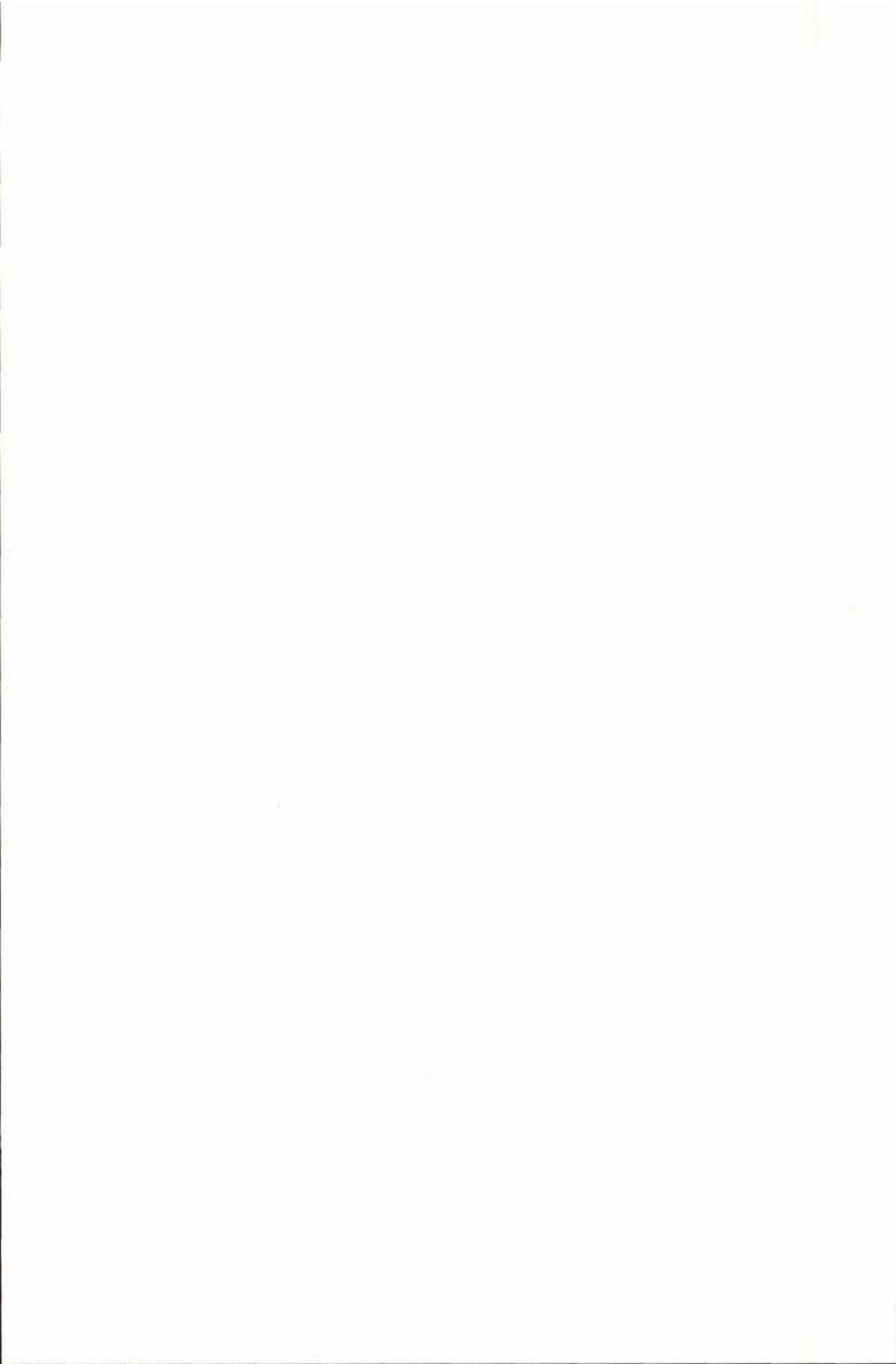


Fig. 2.11 Relative efficiency curve for the ORTEC-GX detector, surrounded by a BGO Compton-suppression shield. The calibration was done on site with sources such as ^{152}Eu , ^{133}Ba and ^{66}Ga , placed in the target position.



Chapter 3

Theory of hadronic interactions in pionic atoms

3.1 Introduction

In this chapter the formalism of strong interaction in pionic atoms is presented briefly. In general no detailed derivations are given. These can be found in standard references (e.g. [Sch 83, Kol 69]). We have adopted the units in which $\hbar = c = 1$.

Pionic atoms are formed by stopping a negatively charged pion in a target and trapping it in the Coulomb field of a nucleus. The initial Bohr orbits into which the pion is captured are not precisely known but indications are that the initial orbit usually has a principal quantum number around 20. It is usually assumed that the initial sublevels have a statistical population ($q_n(2l+1)/n^2$), where q_n is the total population of level n [Men 84]. The main part of the pionic cascade occurs between circular orbits where $n - l = 1$. Neglecting strong interactions and assuming a point nucleus, these are Bohr-like orbits, were the negatively charged pion is replacing one of the electrons. During the cascade down to lower levels, the pionic atom emits Auger electrons and X-rays. This cascade takes between 10^{-15} and 10^{-19} seconds, depending on the nuclear charge number of the host atom.

The principal quantum number n of the highest pionic orbit for which the pion already is localized within the K-electron orbit of the host atom is $n \approx 16$ as follows from the formula

$$\langle r \rangle = \frac{n^2}{(Z\alpha) m} \quad (3-1)$$

for the radius of a Bohr orbit, where Z , α and m are the atomic number, the fine structure constant and the mass of the orbiting particle, respectively. The mass ratio of the pion and the electron is deduced by Jeckelmann et al. [Jec 86] to be $m_\pi/m_e = 273.12677(71)$. This greatly simplifies the analysis for pions in the initial part of the cascade since their motion can be described to a great accuracy as that of a boson influenced only by the Coulomb field from a point-like nucleus with a small correction from vacuum polarization, screening by atomic electrons, effects of electromagnetic polarizability of the nucleus and relativistic reduced mass and the Lamb shift.

When the pion arrives in orbits where its wave function has a significant overlap with the wave function of the nucleus, strong interaction and finite size of the nucleus become important. The

energy levels of such exotic atoms deviate from the energy levels in a point-like Coulomb field for two reasons. They are shifted towards lesser binding because the nuclear charge distribution $\rho(r)$ is not point-like. The levels experience an additional shift, either attractive or repulsive, due to the strong interaction of the bound pion with the nucleons. At the same time the pionic levels are broadened by all those processes which lead to the disappearance of the trapped particle when it interacts strongly with the nucleus (i.e. pion absorption). Both types of level shifts heavily depend on the model used to describe the density distribution of the nuclear matter in the nucleus. As a consequence the experimentally observed energies of the pionic orbits are usually represented by differences with respect to the model-independent theoretical point-nuclear Coulomb energies, corrected for higher order terms. These level shifts and the absorption widths are an important source of information about the strong pion-nucleus interaction. These shifts and widths of atomic levels with hadrons are the quantities of interest in this thesis.

Since the pion is bound in a hydrogen like state, the interaction occurs practically at zero energy or, more precisely, somewhat below the threshold for free particle-nucleon scattering. Because of the low energies only the first partial waves of the pion nucleon interaction are important. An advantage is that the pionic state (the energy and angular momentum l with respect to the nucleus are of course well known for the observed levels) is well-defined in the strong interaction process. Pionic atoms are, therefore, an important source of information about the strong pion-nuclear interaction at low energies.

Low-energy pions are an important probe of nuclei. The reason is that the mean free path of the pion in nuclei is a few fm at energies lower than several tens of MeV. These pions can, therefore, penetrate the interior of the nucleus. They have the additional advantage that pionic atoms can provide information about the π^- -nucleus interaction at the threshold. Such information is supplementary to what we learn from the low-energy scattering. Scattering is not an angular-momentum selector, but has contributions from various angular-momentum states. Furthermore, accurate data of low-energy pion scattering are experimentally difficult to obtain due to the rather high decay-rate of the low-energy pions into muons.

3.2 The Klein Gordon equation

The pion is a boson with spin-parity $J^P = 0^-$ and the pion-nucleus system is therefore described by the modified Klein-Gordon equation:

$$\left[\nabla^2 - \mu^2 + (E - V_C(\mathbf{r}))^2 \right] \Psi(\mathbf{r}) = 2\mu V_S(\mathbf{r}) \Psi(\mathbf{r}) \quad (3-2)$$

The electromagnetic interaction is represented by the Coulomb potential $V_C(\mathbf{r})$, while the "optical potential" $V_S(\mathbf{r})$ represents the influence of the strong interaction, which we will discuss in section 3.3. The reduced mass of the pion-nucleus system is

$$\mu = \frac{m_\pi m_A}{m_\pi + m_A} \quad (3-4)$$

The exact solution of this Klein-Gordon equation, if we neglect the strong interaction and assume a point-like charge distribution, $V_C = Z\alpha/r$, yields the following eigenvalues for the total energy :

$$E_{n,l}^{\text{pnt}} = \frac{\mu}{\sqrt{1 + \left(\frac{Z\alpha}{\lambda}\right)^2}} \quad (3-5)$$

with

$$\lambda = n - (l + 1/2) + \sqrt{(l + 1/2)^2 - (Z\alpha)^2} \quad (3-6)$$

The binding energies of the bound states are then found by subtracting the rest mass:

$$B_{n,l}^{\text{pnt}} = E_{n,l}^{\text{pnt}} - \mu \quad (3-7)$$

3.3 π -N scattering and the π -nucleus interaction

To understand pionic atoms one can describe the π -nucleus interaction on the basis of multiple-scattering theory by the use of the impulse approximation. In this approximation, the scattering of the projectile on a system of bound nucleons is treated as a multiple scattering off free nucleons except for kinematic corrections [Eri 67]. In the multiple scattering formalism describing the π -nucleus interaction a series of coupled integral equations is obtained. We limit ourselves to coherent interactions where the nucleus remains in the ground state and our aim is to derive a Schrödinger equation in the pion variable alone. The total pion wave $\Psi(\mathbf{r})$ is defined as the sum of

the incident wave $\varphi(\mathbf{r})$ and the scattered waves emerging from every one of the scatterers in the medium given by

$$\Psi(\mathbf{r}) = \varphi(\mathbf{r}) + \int d\mathbf{x} \rho(\mathbf{x}) \int d\mathbf{r}' g(\mathbf{r}, \mathbf{r}') \int d\mathbf{r}'' f(\mathbf{r}' - \mathbf{x}; \mathbf{r}'' - \mathbf{x}) \varphi(\mathbf{r}''; \mathbf{x}) \quad (3-8)$$

where $\rho(\mathbf{x})$ is the nucleon density distribution, $\varphi(\mathbf{r}; \mathbf{x})$ the impinging wave on a nucleon located at the site \mathbf{x} , $g(\mathbf{r}, \mathbf{r}')$ a Green's function and $f(\mathbf{k}, \mathbf{k}')$ the pion-nucleon scattering amplitude in the pion-nucleus centre of mass system. For the wave $\varphi(\mathbf{r}; \mathbf{x})$ we can construct a similar equation

$$\varphi(\mathbf{r}; \mathbf{x}) = \varphi(\mathbf{r}) + \int d\mathbf{y} \rho(\mathbf{y}) [1 + G(\mathbf{x}, \mathbf{y})] \int d\mathbf{r}' g(\mathbf{r}, \mathbf{r}') \int d\mathbf{r}'' f(\mathbf{r}' - \mathbf{y}; \mathbf{r}'' - \mathbf{y}) \varphi(\mathbf{r}''; \mathbf{x}, \mathbf{y}) \quad (3-9)$$

where $\varphi(\mathbf{r}; \mathbf{x})$ is expressed in terms of the correlated wave $\varphi(\mathbf{r}; \mathbf{x}, \mathbf{y})$ incident on another nucleon at the site \mathbf{y} . Furthermore, since we know that there is a nucleon at \mathbf{x} we have restricted the location of \mathbf{y} by introducing the correlation function $G(\mathbf{x}, \mathbf{y})$ such that

$$G(\mathbf{x}, \mathbf{y}) \begin{cases} = -1 & |\mathbf{x} - \mathbf{y}| = 0 \\ \approx 0 & |\mathbf{x} - \mathbf{y}| > 0 \end{cases} \quad (3-10)$$

This procedure can be continued by constructing an integral equation for $\varphi(\mathbf{r}; \mathbf{x}, \mathbf{y})$ introducing a three-nucleon correlation function. In first approximation we may say that the full wave function $\Psi(\mathbf{r}) \approx \varphi(\mathbf{r}; \mathbf{x})$ which means that we neglect all correlations and interrupt the hierarchy at the earliest possible stage. We now specify the pion-nucleon scattering amplitude in the low energy region. In the impulse approximation, one treats the scattering of pions on bound nucleons as if it occurred on free nucleons. The free scattering amplitude in the pion-nucleon centre of mass system is given by [Eri 66, Eri 67]

$$f(\mathbf{k}, \mathbf{k}') = b_0 + b_1 \mathbf{t} \cdot \boldsymbol{\tau} + [c_0 + c_1 \mathbf{t} \cdot \boldsymbol{\tau}] \mathbf{k} \cdot \mathbf{k}' + i\sigma_1 \cdot (\mathbf{k}' \wedge \mathbf{k}) [d_0 + d_1 \mathbf{t} \cdot \boldsymbol{\tau}] \quad (3-11)$$

where \mathbf{k}' and \mathbf{k} are the momenta of the scattered and of the incident pion, \mathbf{t} is its isospin and $\boldsymbol{\tau}$ and $\boldsymbol{\sigma}$ are the nucleon isospin and spin. The coefficients b_0 , b_1 , c_0 , c_1 , d_0 and d_1 are related [Eri 66, Sch 83] to the s-wave isoscalar scattering lengths a_{21} and the p-wave isovector scattering volumes $a_{21,2J}$ (Partensky and Ericson [Par 67] have shown that higher partial waves can be neglected in the π -N scattering for energies below 50 MeV). The combinations for b , c and d are:

$$b_0 = \frac{1}{3} (a_1 + 2a_3), \quad b_1 = \frac{1}{3} (a_3 - a_1), \quad (3-12)$$

$$c_0 = \frac{1}{3} [4a_{33} + 2a_{31} + 2a_{13} + a_{11}], \quad c_1 = \frac{1}{3} [(2a_{33} + a_{31}) - (2a_{31} + a_{11})] \quad (3-13)$$

and

$$d_0 = \frac{1}{3} [(a_{11} + 2a_{31}) - (a_{13} + 2a_{33})], \quad d_1 = \frac{1}{3} [(a_{31} - a_{11}) - (a_{33} - a_{13})]. \quad (3-14)$$

If we restrict ourselves to the isoscalar part of the pion-nucleon amplitude, which means only b_0 and $c_0 \neq 0$, and apply the operator $(\Delta + k^2)\Psi(\mathbf{r}) = -2\mu V(\mathbf{r})\Psi(\mathbf{r})$ on eq. (3-8) we obtain the first order optical potential which was for the first time derived by Kisslinger [Kis 55]

$$V_S(\mathbf{r}) = -\frac{2\pi}{\mu} \{ b_0' \rho(\mathbf{r}) - c_0' \nabla \cdot \rho(\mathbf{r}) \nabla \}. \quad (3-15)$$

with

$$b_0' = \left(1 + \frac{m_\pi}{m_N}\right) b_0, \quad c_0' = \left(1 + \frac{m_\pi}{m_N}\right)^{-1} c_0. \quad (3-16)$$

The terms $(1 + m_\pi/m_N)$ and $(1 + m_\pi/m_N)^{-1}$ are kinematical factors, arising from the transformation of the scattering amplitude f in eq. (3-11) from the pion-nucleon center of mass to the pion-nucleus center of mass system. The first term between the brackets in eq. (3-15) is usually named the local part, the second term the (velocity dependent) non local part of the optical potential.

An improved set of equations is obtained by breaking off the iteration at the second step, putting $\varphi(\mathbf{r}; \mathbf{r}_j, \mathbf{r}_i) \approx \varphi(\mathbf{r}; \mathbf{r}_i)$ in eq. (3-9). As is shown in ref. [Sch 83] this gives the Ericson-Ericson optical potential in second order of the form

$$V_S(\mathbf{r}) = -\frac{2\pi}{\mu} \left[q(\mathbf{r}) - \nabla \cdot \frac{\alpha(\mathbf{r})}{1 + \frac{4}{3}\pi\xi\alpha(\mathbf{r})} \nabla \right] \quad (3-17)$$

with

$$q(\mathbf{r}) = b_0' \rho(\mathbf{r}) \quad \text{and} \quad \alpha(\mathbf{r}) = c_0' \rho(\mathbf{r}). \quad (3-18)$$

The second order effect contained in eq. (3-17) essentially renormalizes the p-wave interaction; this phenomenon reminds one of the Lorentz-Lorenz effect for light scattering in dense media. Comparison with eq. (3-15) shows that the introduction of short-range correlations renormalizes the p-wave part of the interaction but leaves the s-wave part unchanged. The new parameter ξ in eq. (3-17) depends on the range of the nucleon-nucleon correlations and the range of the pion-nucleon interaction. Usually, they both are assumed to be zero, in which case one obtains $\xi = 1$.

In order to account for an isospin dependence of the optical potential we should include the terms with b_1 and c_1 in eq. (3 - 11). Ericson and Ericson [Eri 66] show that these lead to a modified set of functions $q(\mathbf{r})$ and $\alpha(\mathbf{r})$:

$$q(\mathbf{r}) = b_0'\rho(\mathbf{r}) + b_1'\delta\rho(\mathbf{r}) \quad \text{and} \quad \alpha(\mathbf{r}) = c_0'\rho(\mathbf{r}) + c_1'\delta\rho(\mathbf{r}) \quad (3 - 19)$$

where b_1' and c_1' are related to b_1 and c_1 as in eq. (3 - 16) for b_0' and c_0' , and $\delta\rho(\mathbf{r})$ specifies the difference of the density functions for protons and neutrons in the nucleus (see below). The spin dependent terms with d_0 and d_1 in the scattering amplitude (eq. (3 - 11)) give a negligible contribution and are therefore left out of this discussion. So far, d_0 and d_1 have not been constrained by any pionic atom experiment.

The existence of absorption of pions in nuclear matter gives rise to the finite widths of pionic atom levels and indicates the need for an imaginary part in the optical potential. The absorption process $\pi + N \rightarrow N$ hardly takes place in the nucleus because of energy-momentum conservation: The absorption of a zero energy pion requires a nucleon momentum $p \approx (2m_\pi m_p)^{1/2} \approx 525 \text{ MeV}/c$. However, the Fermi momentum of nucleons in the nucleus is only about $250 \text{ MeV}/c$. Consequently a pion absorption process in nuclei involves the participation of at least two nucleons. One parameterizes it by including in eq. (3 - 17) terms that depend on the square of the nucleon density. This results in replacing the s- and p-wave parts of the optical potential by

$$q(\mathbf{r}) = \left(1 + \frac{m_\pi}{m_N}\right)(b_0\rho(\mathbf{r}) + b_1\delta\rho(\mathbf{r})) + \left(1 + \frac{m_\pi}{2m_N}\right)(B_0\rho^2(\mathbf{r}) + B_1\rho(\mathbf{r})\delta\rho(\mathbf{r})) \quad (3 - 20)$$

and

$$\alpha(\mathbf{r}) = \left(1 + \frac{m_\pi}{m_N}\right)^{-1}(c_0\rho(\mathbf{r}) + c_1\delta\rho(\mathbf{r})) + \left(1 + \frac{m_\pi}{2m_N}\right)^{-1}(C_0\rho^2(\mathbf{r}) + C_1\rho(\mathbf{r})\delta\rho(\mathbf{r})) \quad (3 - 21)$$

where the terms $(1 + m_\pi/2m_N)$ again are kinematic factors. The second terms in eq. (3 - 20) and (3 - 21) are introduced on a purely phenomenological basis. The constants B_0 , B_1 and C_0 , C_1 contain all the information on the complicated short-range pion absorption process in the nucleus. These terms parametrize pion absorption, their coefficients are complex numbers. The real parts represent dispersion effects, the imaginary part the absorption of a pion on a nucleon pair. As in the linear parts, the '0' labels the isoscalar terms, while '1' labels the isovector terms, which depend on the difference of the neutron and proton densities. The complex parameters B_1 and C_1 which represent the isovector part of the absorption process are usually taken equal to zero in the optical potential used for pionic atoms.

3.4 Coulomb potential and nuclear density distribution functions

As the pion reaches lower orbits, where it feels the strong interaction, it is important that the finite size of the nucleus is taken into account. We will treat its influence on the pion nucleus Coulomb potential V_C . For a nucleus of finite size, it is given by

$$V_C(\mathbf{r}) = -\alpha \int \frac{\rho_p(\mathbf{r}')}{|\mathbf{r} - \mathbf{r}'|} d^3 r' \quad (3-22)$$

For a spherical symmetric distribution this reduces to

$$V_C(r) = -4\pi\alpha \left\{ \frac{1}{r} \int_0^r r'^2 \rho_p(r') dr' + \int_r^\infty \rho_p(r') r' dr' \right\} \quad (3-23)$$

For the proton density distribution $\rho_p(\mathbf{r})$ we assume Fermi distributions

$$\rho(r) = \rho_0 \left[1 + e^{\frac{(4 \ln 3)rc}{t}} \right]^{-1} \quad (3-24)$$

in which c represents the radius and t is a measure for the skin thickness. We will assume that the neutron distribution needed for the strong interaction optical potential is also a Fermi distribution. The distribution functions $\rho_p(\mathbf{r})$ and $\rho_n(\mathbf{r})$ are normalized to Z and $A - Z$, respectively;

$$\int_0^\infty \rho_p(\mathbf{r}) d^3 r = Z, \quad \int_0^\infty \rho_n(\mathbf{r}) d^3 r = A - Z \quad (3-25)$$

We define the isoscalar and isovector densities as

$$\rho(\mathbf{r}) = \rho_n(\mathbf{r}) + \rho_p(\mathbf{r}), \quad \delta\rho(\mathbf{r}) = \rho_n(\mathbf{r}) - \rho_p(\mathbf{r}) \quad (3-26)$$

With these formula one can calculate the purely electromagnetic effect of the finite size of the nucleus. Examples of the results are shown in table 3.2.

3.5 Optical potential parameter fits

First attempts to describe the optical potential by using the free pion-nucleon scattering amplitude in eq. (3 - 11) were not successful. One therefore started to treat ξ , b_0 , b_1 , B_0 , c_0 , c_1 and C_0 as fit parameters.

If the impulse approximation, used to derive the optical potential from free pion-nucleon scattering, is a good one the parameters $\{\xi, b_0, b_1, c_0$ and $c_1\}$ in the potential can be derived from extrapolating low energy pion-nucleon scattering experiments to zero energy. Phase shift analyses of $\pi^\pm N$ scattering, compiled by Nagels et al. [Nag 76] gave for the different coefficients:

$$b_0 = (-0.013 \pm 0.003) m_\pi^{-1}, \quad b_1 = (-0.092 \pm 0.001) m_\pi^{-1}, \quad (3 - 27a)$$

$$c_0 = (0.209 \pm 0.005) m_\pi^{-3}, \quad c_1 = (0.177 \pm 0.003) m_\pi^{-3}, \quad (3 - 27b)$$

$$[d_0 = (0.189 \pm 0.003) m_\pi^{-3}, \quad d_1 = (0.070 \pm 0.002) m_\pi^{-3}]. \quad (3 - 27c)$$

The complex absorption parameters $\{B_0$ and $C_0\}$ must always be fit, because these are introduced on a phenomenological basis.

The number of fit parameters in the optical model is typically around 10. Solving the Klein Gordon equation with the optical potential using the parameters ξ , b_0 , b_1 , B_0 , c_0 , c_1 and C_0 results in complex energy eigenvalues giving the strong interaction level shifts ϵ_0 and widths Γ_0

$$E_{n,l} = \text{Re}(E_{n,l}) + i \text{Im}(E_{n,l}) = E_{n,l}^{\text{pnt}} - \epsilon_0 - \frac{i}{2} \Gamma_0. \quad (3 - 28)$$

The observed strong-interaction shifts and widths of the more peripheral levels in pionic atoms have successfully been fit by semi-phenomenological optical potentials. These levels are orbits where there is only a small overlap between the pion wave function and the nuclear matter distribution (eg. 4f levels in ^{241}Pt , ^{197}Au , 2p in ^{16}O). The used optical potentials all are variants of the potential given in eq. (3 - 17, 20 and 21). Some of the resulting sets are shown in table 3.1. One of the first to compare results derived from such a formula to pionic atom data were Krell and Ericson [Kre 69], making a fit to eleven 1s and fifteen 2p levels in light nuclei. On the whole they found the multiple scattering description to be quite successful as a framework for describing the pion-nucleus interaction. The fitted values from the pionic atom data remain in the neighborhood of their counterparts of pion-nucleon scattering, as can be seen in a comparison with table 3.1. Already in 1971 Tauscher [Tau 71] presented a more elaborate fit to the pionic atom data resulting in sets for the strong interaction parameters one with $\xi = 0$ (no Lorentz-Lorenz term) and one with $\xi = 1$. We use two sets of this author to compare with our data. The set with $\xi = 0$ is only taken to show the influence of the Lorentz-Lorenz effect. Including the effect ($\xi = 1$) improved the fit

Table 3.1: Strong interaction optical-potential parameter sets, used to calculate the strong interaction level shifts and widths (B_1 and C_1 are zero in these sets). Also given are results obtained from pion-nucleon scattering analysis.

	ξ	b_0 m_π^{-1}	b_1 m_π^{-1}	$\text{Re } B_0$ m_π^{-4}	$\text{Im } B_0$ m_π^{-4}	c_0 m_π^{-3}	c_1 m_π^{-3}	$\text{Re } C_0$ m_π^{-6}	$\text{Im } C_0$ m_π^{-6}
[Tau 71 $_{\xi=0}$]	0	-0.0293	-0.078	0	0.0428	0.172	0.22	0	0.036
[Tau 71 $_{\xi=1}$]	1	-0.0293	-0.078	0	0.0428	0.227	0.18	0	0.076
[Bat 79]	1	-0.017	-0.13	-0.0475	0.0475	0.255	0.17	0	0.090
[Sek 83]	1	0.003	-0.143	-0.15	0.046	0.21	0.18	0.11	0.090
[Nag 76]		-0.013	-0.092			0.209	0.177		

remarkably. The parameter set obtained by Batty et al. [Bat 79] is a modification of the second set in the table in which B_0 also has a real part. The set obtained by Seki and Masutani [Sek 83] is a further modification, including an extra s-wave repulsion. The latter authors performed fits on the largest set of data (59 atoms).

For completeness the rather different approach of Birbrair et al. [Bir 83, Bir 85] should be mentioned. They use a relativistic many-body approach to the pion-nucleus interaction, fitting the shifts and widths of π -atomic states, low-energy pion-nucleus scattering and coherent photo production of π^0 . The nucleus is considered as a relativistic system of nucleons in self-consistent scalar and vector fields, where they take the direct interaction of the pion with scalar nuclear fields into account. Their approach contains fewer adjustable parameters but the agreement with experiment is at least as good as that in the conventional theory. Yet, their predictions for the strong interaction shifts and widths of deeply-bound 3d states (eg. 3d level in ^{nat}Pt and ^{197}Au) also fail to describe the experimental values.

3.6 Deformation

Due to the spectroscopic quadrupole moment of the nuclear ground state, the levels of the pionic atom show a hyperfine splitting if the nuclear spin $I \geq 1$. To calculate this splitting Koch and Scheck [Koc 80] expanded the optical potential in terms of the non-spherical density

contributions. For a non-spherical nucleus of spin I , the single-particle matter density is given by the ground state expectation value with maximal magnetic quantum number $M = I$,

$$\begin{aligned} \rho(\mathbf{r}) &= \int d^3\mathbf{r}_1 \dots \int d^3\mathbf{r}_A \sum_{i=1}^A \phi_{I,I}^2(\mathbf{r}_1, \dots, \mathbf{r}_A) \delta(\mathbf{r} - \mathbf{r}_i) \\ &\equiv \rho_0(\mathbf{r}) + \sum_{k=1}^I \sqrt{\frac{4k+1}{16\pi}} \rho_{2k}(\mathbf{r}) Y_{2k,0}(\hat{\mathbf{r}}) . \end{aligned} \quad (3-29)$$

Analogous expansions in terms of multipole densities can be written down for the proton and neutron densities. These expansions are completely general and no model assumption is involved. In this discussion we limit ourselves to nuclei with only a quadrupole deformation

$$\rho(\mathbf{r}) = \rho_0(\mathbf{r}) + \sqrt{\frac{5}{16\pi}} \rho_2(\mathbf{r}) Y_{20}(\hat{\mathbf{r}}) . \quad (3-30)$$

This density function is chosen in such a way that the r^2 moment of ρ_2^p directly yields the spectroscopic quadrupole moment Q_s ,

$$Q_s = Z \int_0^\infty dr r^2 [r^2 \rho_2^p(r)] . \quad (3-31)$$

As a consequence of the fact that the ground state of the nucleus is no more spherically symmetric, the Coulomb and the strong interaction optical potential give rise to quadrupole interaction terms. Neither the nuclear spin I nor the meson's orbital angular momentum l are good quantum numbers. Instead, the atomic states must be classified by the total angular momentum $F = l + I$, which takes on the values $F = l + I, l + I - 1, \dots, |l - I|$. The unperturbed state l (defined for the monopole part of the interactions) is split in a series of hyperfine states which are characterized by the eigenvalues of F . Scheck [Sch 72] showed that the energy of a given member of such a hyperfine multiplet, with total angular momentum F , relative to the point-nucleus value, follows the pattern

$$E_{n,l}^{\text{pnt}} - E_{n,(l,I),F} = A_1 \gamma(I,l,F) + (\epsilon_0 + \frac{1}{2} i\Gamma_0) + (\epsilon_2 + \frac{1}{2} i\Gamma_2 - A_2) C(I,l,F) \quad (3-32)$$

in which the quantum numbers n,l are those of the unperturbed pionic orbit. $E_{n,l}^{\text{pnt}}$ is the energy of that state in the spherical Coulomb field of a point-like nucleus, A_2 is the electric hyperfine structure constant and A_1 represents the hyperfine interaction between the magnetic dipole moment of the nucleus and the magnetic field, created by the pion's orbital motion. For the strong

interaction monopole and quadrupole shifts ϵ_0 and ϵ_2 and widths Γ_0 and Γ_2 , see below. The angular momentum factor $C(I, l, F)$ for the quadrupole hyperfine structure is given by

$$C(I, l, F) = \frac{3\gamma(\gamma + 1) - 4I(I + 1)l(l + 1)}{2I(2I - 1)l(2l - 1)} \quad (3 - 33)$$

where γ in equation (3 - 31) and (3 - 32) is the familiar expression of the hyperfine interaction

$$\gamma(I, l, F) = F(F + 1) - I(I + 1) - l(l + 1) . \quad (3 - 34)$$

The value of $C(I, l, F)$ is equal to unity for the maximum value of F .

Koch and Scheck [Koc 80] show that the electric quadrupole hyperfine constant A_2 , due to the quadrupole part of the Coulomb potential for a nucleus with a density distribution $\rho(r)$ is given by

$$A_2 = \frac{1}{2} e^2 \frac{l}{2l + 3} \left\{ \int_0^\infty dr r^2 R_{n,l}^2(r) \left[\frac{1}{r^3} \int_0^r dr' r'^4 \rho_2^p(r') + r^2 \int_r^\infty dr' \frac{1}{r'} \rho_2^p(r') \right] \right\} \quad (3 - 35)$$

where $R_{n,l}(r)$ is the complex radial part of the mesonic bound state wave function normalized to unity. As a result of the complex $R_{n,l}(r)$ the electric quadrupole constant A_2 also becomes complex. The observable pionic orbits penetrate the nucleus very little. In first approximation this means, that the first integral in the square brackets on the right hand side of eq. (3 - 32) may be extended to infinity, while the second may be neglected. In this approximation A_2 becomes proportional to the spectroscopic quadrupole moment Q_s :

$$A_2 \approx \frac{1}{2} \alpha Q_s \frac{l}{2l + 3} \int_0^\infty dr r^2 R_{n,l}^2(r) \frac{1}{r^3} . \quad (3 - 36)$$

The quantity Q_s has been determined rather precisely by measuring transitions in pionic and muonic atoms (see e.g. chapter 5 of this thesis and refs. [Ebe 78, Kon 81]). A consequence of A_2 being complex is that not only the shifts but also the widths show a hyperfine pattern behaviour. The imaginary part is, however usually too small to be observed experimentally.

The monopole shift ϵ_0 is the difference between the real part of the actual average energy (centroid of the hyperfine multiplet) and the energy in the electric field of a point charge, which difference is model independent. For pionic atoms with a nuclear quadrupole moment the strong interaction will induce an additional strong interaction quadrupole shift $\epsilon_2(F)$ for each hyperfine level. We now define an effective electric quadrupole hyperfine constant A_2^{eff} (this is the observable in experiments) in analogy with the electric constant A_2 . In the quantity

$$A_2^{\text{eff}} = \text{Re } A_2 - \epsilon_2 \quad (3 - 37)$$

not only the calculated value for ϵ_2 but also that for $\text{Re } A_2$ depend on the optical model used. As was pointed out by Koch and Scheck [Koc 80], the model dependence of A_2 is mostly weak, especially for peripheral orbits. The strong interaction quadrupole shift ϵ_2 is therefore obtained in an analysis where the deformation parameters, taken from the muonic atom hyperfine splitting experiments, are used to calculate the electric quadrupole part (A_2) of the hyperfine splitting in pionic atoms of the same isotope, after which the difference with the experiments gives the ϵ_2 . For muonic atoms A_2 is real as the μ^- is not subject to strong interaction absorption.

The magnetic dipole interaction (the first term in on the right-hand side of eq. (3 - 32)) between a pion and a nucleus is relatively unimportant with respect to the electrostatic quadrupole interaction. In ordinary (electronic) atoms the magnetic and electric hyperfine effects are of the same order of magnitude. However, since the ratio of the strengths of both interactions in pionic atoms goes as the ratio of the electron mass to the pion mass the effect is rather small here. Therefore, in the case of pionic (and muonic) atoms, the magnetic splitting is buried in the electric quadrupole structure. The magnetic dipole hyperfine constant A_1 is proportional to the nuclear magnetic moment and a matrix element, which depends on nuclear and pion wave functions. In higher orbits there is no penetration of the pion wave functions in the nucleus and the matrix elements can be calculated model independently. A calculation of A_1 with non-relativistic wave functions leads to the following expression [Dey 75] for the magnetic hyperfine constant of a point nucleus

$$A_1 = g_I \alpha^4 Z^3 \frac{m_\pi^2}{2m_p} \frac{1}{n^3 l(l+1)(2l+1)} \quad (3 - 38)$$

where the gyromagnetic ratio g_I is the magnetic dipole moment (μ) given in units of nuclear magnetons, divided by the nuclear spin I . Since the correction is so small, we use the point nucleus value also for lower orbits.

3.7 Higher order corrections

Several higher order corrections have to be applied to obtain a good description of the pionic atom levels. All the corrections, mentioned below, are calculated in higher order perturbation theory, using the computer code PIATOM [Tau 78]. The applied corrections are described in this section. The influence of the various corrections on the calculated values for the presently measured pionic levels is presented in table 3.2 and appendix B.

1) Vacuum polarization

The vacuum polarization potential is due to virtual positron–electron pairs: The charge of the nucleus acts on the pion by the exchange of a virtual photon. The exchanged photon, through its quantum nature, can transform into all intermediate states which can annihilate and transform back into the same photon state again (e.g. positron–electron pairs). The net effect of such pairs is a modification of the photon propagator and, consequently, the pion-nucleus interaction.

In our calculations, vacuum polarization is taken into account for the orders $\alpha(\alpha Z)$, $\alpha^2(\alpha Z)$, $\alpha(\alpha Z)^3$, $\alpha(\alpha Z)^5$ and $\alpha(\alpha Z)^7$. The expressions for the vacuum polarization can be found in the references [Fri 69] and [Blo 72]. In light nuclei these corrections are very small, but they become non-negligible in heavy nuclei. Examples are given in table 3.2.

2) Electron Screening

The electron screening correction is due to the potential created by the atomic electron cloud of the pionic atom. Although the atomic electrons are far away, for orbits with principal quantum numbers $n \leq 10$ they slightly influence the energy levels of the exotic atom. The penetration of the pionic orbits by the electron cloud produces a substantial but slowly varying change in energy of the pionic state with respect to the pionic orbit principal quantum number (see table 3.2). The screening is produced almost entirely by the 1s electrons. The most accurate calculation of screening uses a relativistic Hartree Fock calculation [Vog 74] of the atomic electrons moving in the field of the nucleus and the pion. Such calculations assume full occupation of the lowest electron states and then give only an upper limit for the screening correction. Owing to the Auger transitions during the cascade of the pion, the electronic shells are actually depopulated and partly emptied. We performed cascade calculations, where the probability of these Auger transitions and the rate of refilling of vacancies were taken into account to obtain the mean populations of the K and L shells during the cascade. The results, of which examples are given in appendix B, table B.1, were used in the electron cloud screening calculations. The results of these screening calculations can be found in table 3.2 and B.5

3) Electromagnetic nuclear and pion polarization

The orbiting particle induces at the nuclear site a fluctuating electromagnetic field which affects the energy levels of the atom. This electric field polarizes the nucleus by separating the protons from the neutrons relative to the nuclear center of mass. This effect is named nuclear polarization and is taken into account in our calculations. Tauscher et al. [Tau 78]

calculate the energy shift for the pionic level in first order perturbation theory, using the nuclear polarization potential

$$V_{NP}(r) = \frac{e^2 \alpha_N}{2r^4} \quad r \geq R \quad (3-25a)$$

$$V_{NP}(r) = a - br^2 \quad r \leq R \quad (3-25b)$$

where R and α_N are the nuclear radius and polarizability, respectively. The parameters a and b are chosen to make the two expressions match at the nuclear surface. The accuracy of this correction is given by the uncertainties of α_N and those of the underlying model. An error estimate given by Tauscher [Tau 78] is 10% of the correction. Values for this correction are given in table 3.2.

Iachello and Landé [Iac 71] have investigated the effect of the finite size and polarizability of the pion due to the field of the nucleus. They find that the resulting level shift caused by finite size is a small fraction of the strong interaction shift and very difficult to separate from it. More interesting is the level shift due to the polarizability of the pion. A pion in the electric field produced by the nuclear charge obtains an induced electric dipole moment that leads to a change of the Hamiltonian of the total system. This effect was measured by Antipov et al. [Ant 83] and found it to be negligible for the transitions investigated in this work.

4) Relativistic reduced mass effect

When the pion nucleus centre of mass motion is separated in order to obtain eq. (3 - 11), relativistic nuclear recoil effects are neglected. The fully relativistic Klein Gordon equation is given by (3 - 11) by substituting [Fri 73, Fri 75 and Bar 73]:

$$V \rightarrow \frac{V}{\sqrt{1 - m_\pi^2/M^2}}, \quad \mu \rightarrow \left[\frac{m_\pi}{\sqrt{1 - m_\pi^2/M^2}} + \frac{m_\pi B}{M} \right] / (1 + m_\pi/M) \quad (3-26)$$

where M is the nuclear mass. The binding energy B is always much smaller than even the pion mass. For $m_\pi \ll M$ the expressions (3 - 26) reduce therefore to V and μ , respectively.

5) Lamb shift

The self energy of a bound pion manifests itself as the energy shift of a level due to its

interaction with the quantized radiation fields. According to quantum theory, even if there is no incident radiation present, the atomic level can emit and subsequently absorb a photon. This process results in a level shift, called the Lamb shift. Calculations show, that the Lamb shift only significantly influence s - states, which have non-vanishing wave functions at the origin [Sak 67]. For the investigated 4f and 3d levels in this work, no Lamb shift is expected, however, in measurements of pionic 1s orbits it is one of the most important corrections.

All these corrections are included in the computer code PIATOM, written by Tauscher [Tau 78]. The values of these corrections for some of the measured nuclei can be found in table 3.2. We checked the dependence on different sets of optical potential parameters of these corrections for the 3d and 4f states in ^{181}Ta . The variations for the different sets are negligible small in comparison to the experimental error in the shift of the corresponding level.

Table 3.2: Examples of higher order corrections terms for orbits with $l = n - 1$ for some of the investigated pionic levels (full results in appendix B). For the calculations the parameter set from ref. [Bat 79] was used. All values are in keV. The finite size is not included in the last column.

	n	finite size	vacuum polarisation				electron screening	nuclear polar.	reduced mass	Σ_{corr}
			$\alpha(\alpha Z)$	$\alpha^2(\alpha Z)$	$\alpha(\alpha Z)^3$	$\alpha(\alpha Z)^{5,7}$				
^{181}Ta	3	3.59	-11.83	-0.09	0.13	0.01	6.97	-0.17	-0.02	-4.99
	4	0.01	-4.33	-0.03	0.08	0.01	6.95	-0.01	-0.01	2.67
	5	0.00	-1.90	-0.01	0.04	0.01	6.92	-0.00	-0.00	5.06
^{209}Bi	3	10.10	-16.38	-0.12	0.19	0.03	8.78	-0.32	-0.03	-7.85
^{237}Np	4	0.18	-8.49	-0.06	0.22	0.04	11.24	-0.05	-0.01	2.89
	5	0.00	-3.81	-0.03	0.13	0.03	11.16	-0.01	-0.00	7.47
	6	0.00	-1.89	-0.01	0.08	0.02	11.04	-0.00	-0.00	9.22

The general conclusions from these calculations are the following (see also table B5):

- i. The corrections for Lamb shift and reduced mass are entirely and for nuclear polarization almost negligible.
- ii. The corrections for nuclear finite size and vacuum polarization grow as one goes to deeper lying orbits.
- iii. The correction due to electron screening on the level energies is a rather large effect for heavy targets, but does hardly change from level to level so that the correction on the X-ray transition energies is of minor importance.

3.8 Optical potential calculations

3.8.1 Strong interaction monopole shifts and widths

We now discuss our way of calculating the measurable quantities Γ_0 (width) and ϵ_0 (shift) in relation to values for the relevant parameters in the optical potential. This is done by solving the Klein-Gordon equation, using the computer codes PIATOM and MESON written by Tauscher [Tau 78] and Koch [Koc 73, Koc 80], respectively. These codes use the Numerov method [Bla 67] for integrating the Klein-Gordon equation with the optical and Coulomb potential. The higher order corrections and deformation effects are then calculated in perturbation theory.

Unfortunately, neither of the codes calculates all the higher order effects and deformation, but by using both programs one can obtain a complete picture. The code MESON calculates the strong interaction observables ϵ_0 and Γ_0 with respect to the point Coulomb value and includes finite size and deformation effects. This code, which follows the formalism introduced by Koch and Scheck [Koc 80] does not allow the incorporation of different radii for the proton and neutron distributions. The code PIATOM calculates all higher order terms like vacuum polarization, Lamb shift, electron screening and nuclear polarization. In this code, different radii for the proton and neutron distributions can easily be introduced. It can, in fact, even accommodate isovector absorption terms $\text{Im}B_1$ and $\text{Im}C_1$. The latter code, however, does not calculate deformation effects.

Some input values concerning the target nuclei used are given in table 3.3. The c and t values of the Fermi density distribution functions are taken from muonic atoms (see e.g. Engfer et al. [Eng 74] and electron scattering experiments [Vri 87]). The deformation parameter β is derived from values of measured nuclear quadrupole moments, using formula (5 - 10) given in chapter 5.

The following procedure has been adopted to calculate the strong interaction shifts and widths and higher order corrections (the detailed results of the calculations are presented in appendix B).

- i. The strong interaction monopole and quadrupole observables ϵ_0 , Γ_0 , ϵ_2 , $\text{Re}A_2$, finite size and nuclear deformation are calculated with the code MESON. For the nuclei ^{181}Ta , $^{\text{nat}}\text{Re}$ (nat \equiv natural abundance), $^{\text{nat}}\text{Pt}$, ^{197}Au , ^{208}Pb , ^{209}Bi and ^{237}Np the detailed results are given in appendix B for the 3d, 4f and 5g levels.
- ii. The population of the K and L electron shells during the pionic $5g \rightarrow 4f$ and $4f \rightarrow 3d$ transitions are calculated with the pionic cascade code STARKEF [Tau 78]. The results are listed in table B.1 and used as input for PIATOM to calculate the electron screening.
- iii. The higher order corrections terms like vacuum polarization, electron screening, Lamb shift, relativistic reduced mass effects and nuclear polarization are calculated as discussed in section 3.4 with the code PIATOM and listed in table B.5.
- iv. For the calculations with different neutron and proton density distributions the experimental values by Hofman et al. [Hof 80] for ^{208}Pb are used as a starting point of our calculations with the code PIATOM. The calculations are done twice for each pionic level and each parameter set: once for equal radii and once more for $c_n = c_p + 0.14$ fm (for the special case of ^{208}Pb we used some more Δc_{np} values). The changes in the results for ϵ_0 and Γ_0 are subsequently added to the results of the code MESON and presented in the discussion of chapter 4.
- v. The influence of a possible isovector absorption parameter $\text{Im}B_1$ and $\text{Im}C_1$ in the optical potential is also investigated with the computer code PIATOM in the same way as for the difference in radii.

The magnitude of nuclear finite size in the calculation of the pionic transition energies is listed in the table with higher order corrections in the appendix B. The parameter set dependence present in the higher order terms such as vacuum polarization, electron screening and nuclear polarization is negligible.

3.8.2 Quadrupole splitting

In the next chapter, we will determine shifts and widths of pionic X-rays for several nuclei. Among them the odd mass isotopes of Ta, Re and Np have a quadrupole splitting that cause deviations of the shifts and widths from the direct experimental results.

The formula in section 3.6 for calculating the strong interaction quadrupole interaction parameters show that e.g. the 5g orbit in pionic ^{181}Ta is eightfold split, the 4f level sevenfold and the 3d state fivefold. Taking selection rules for transitions between both the 5g and the 4f hyperfine complexes into account, the resulting X-ray pattern consists of twenty members, see figure 4.3. In the case of the Re isotopes and ^{237}Np the pionic 5g and 4f levels are sixfold split, the 3d state fivefold, and the 5g \rightarrow 4f X-ray pattern counts 15 members. The average distances between the components are smaller than the resolution (FWHM) of our detectors, and -more essentially- often even than the natural widths. We therefore adopt a procedure described below.

The main part of the splitting is due to electromagnetic interaction with the electric quadrupole moment Q which yields the term A_2 in eq. (3 - 32). These moments are known with sufficient precision (for ^{237}Np see chapter 5).

With sufficient accuracy, one can take equal values for the widths of all components of a multiplet. Thus, only four parameters are necessary to parametrize the expected natural shape of a multiplet for which we choose

- a) The energy (position of the centroid) of the hyperfine complex.
- b) The energy difference ΔE between two components with the highest intensity of the hyperfine complex.
- c) The intensity of the largest component of the multiplet.
- d) One Lorentzian width of the convoluted complex.

Corrections are applied for the following effects:

- i magnetic dipole interaction
- ii strong interaction quadrupole interaction

ad(i) The main part of the hyperfine splitting of the levels in electronic atoms is due to magnetic dipole interaction. In pionic and muonic atoms, however, these interactions have a minor effect, with a magnitude around 1% because they scale with a factor m_e / m_π and m_e / m_μ , respectively, compared to the electric quadrupole interaction.

ad(ii) We assume here the neutron distribution radius c_n is equal to the proton radius c_p . We further assume the nucleus to have mainly a quadrupole deformation with a density distribution $\rho(\mathbf{r})$ according to formula (3 - 30). These assumptions are sufficient for the purpose of taking quadrupole shifts into account.

We assume that the initial hyperfine levels are statistically populated. The relative intensity I_{rel} of an E1 hyperfine transition between levels of the total angular momentum quantum numbers F_i and F_f is then given by

$$I_{\text{rel}}(F_i \rightarrow F_f) \propto (2F_i + 1)(2F_f + 1) \left\{ \begin{matrix} l_f & F_f & I \\ F_i & l_i & 1 \end{matrix} \right\}^2 (\Delta E_{i \rightarrow f})^3 \quad (3 - 35)$$

where $\Delta E_{i \rightarrow f}$ is the energy difference between the levels F_i and F_f . The assumption of the statistical population seems justified since M1 Auger transitions between F levels are expected to be much slower than the E1 hyperfine transitions [Win 63].

The parametrized natural line shape obtained in this way is folded with the detector response function and compared with the experimental results. We will show in chapter 4 that excellent fits can be obtained, which we consider to be a confirmation of the correctness of the procedure described above.

Chapter 4

Systematics of pionic 3d and 4f levels in ^{181}Ta , natural Rhenium, natural Platinum, ^{197}Au , ^{208}Pb , ^{209}Bi and ^{237}Np

4.1 Introduction

In this chapter we discuss further experiments on the anomaly for some pionic-atom states in comparison with values obtained from calculations using the standard optical potentials for the pion-nucleus interaction as discussed in the preceding chapter.

The analysis of the strong interaction parameters has yielded information on the zero-energy π -nucleus interaction. Several parameters in a semi-phenomenological description of the pion-nucleus optical potential (based on the original Kisslinger form) containing terms linear and quadratic in the nuclear density, have through the years been determined from a large body of available pionic-atom data [Sek 83 and refs contained there in].

Besides fitting the available data on pionic atoms reasonably well, this potential has also been used successfully in predicting pion photo production cross sections near threshold. Furthermore, this potential has been shown to be consistent with the optical potential used for low-energy pion-scattering, in which process the magnitude of pion absorption is of the order of 50%. Since absorption is found to contribute to such an extent and also because the process is far from being understood (the absorption terms in the optical potential are based on a naive phenomenological picture) it is considered important to study in particular the absorption process in further detail.

In scattering experiments one can vary the energy and momentum transfer. These parameters are fixed in the case of pionic atoms. Yet by choosing the targets one still has a certain selection of angular momentum. Absorption is then the only open reaction channel for the pion so that the study of pionic atoms is the cleanest way to investigate the process. In light isotopes one observes absorption from the 1s orbit ($l = 0$) which is dominated by the repulsive local s-wave interaction term of the optical potential. In heavier nuclei the absorption takes place from 2p ($l = 1$), 3d ($l = 2$) and higher levels, where the non-local attractive p-wave interaction dominates the process. When the overlap between pion and nuclear wave functions becomes larger in deeper pionic orbits, the repulsive s-wave part in the interaction becomes increasingly important. This effect has been observed for the strong interaction shift ϵ_0 in the pionic 2p state by Abela et al. [Abe 77].

The rapid growth of absorption for increasingly deeper bound pions causes that information on states characterized by selected principal and orbital quantum numbers (e.g. 3d states) can only be

obtained up to a certain maximum Z -value. Beyond that value the intensity of the transition considered becomes prohibitively small. Before 1977, the limit was $Z=60$ for the pionic 3d level. For those data, the existing theory was able to describe strong-interaction effects rather satisfactory. In 1979 Konijn et al. [Kon 79], by using much improved detection techniques, could extend experiments to deeper bound orbits. Although the data in their experiments were only of moderate statistics, the results allowed a first glance at deeply-bound pionic orbits, with a large overlap between the pion wave function and the nuclear density. They thus found significant deviations from theory: the reported shifts and widths of these 3d levels are roughly a factor two smaller. Later results for the heaviest atoms for which the 1s (Na [Oli 78] and Mg [Taa 85]) and 2p (As [Abe 77]) levels have been measured, must also be taken as an indication of a similar systematic deviation for the deep-lying levels.

Systematic investigations of the anomalous shifts and widths in terms of the optical potential have been performed by Friedman and Gal [Fri 80], Ericson and Tauscher [Eri 82], Seki [Sek 82], Batty et al. [Bat 83], Tauscher et al. [Tau 84] and Olivier et al. [Oli 84]. The small experimental strong interaction monopole shifts ϵ_0 can qualitatively be understood, as well as the change of sign of the quadrupole shift ϵ_2 (see chapter 3) for deeply-bound pionic levels going from the pionic 4f to the 3d state, to be the result of the delicate balance between the (repulsive) local and the (attractive) non-local parts of the optical potential [Kon 79]. The discrepancy for the widths persists in all the fits. Qualitatively a strong enhancement of the repulsive s-wave potential is required [Sek 83, Oli 84].

Getting a better understanding of the pionic optical potential representing the strong pion-nucleus interaction requires systematic measurement of pion absorption from deeply-bound states, i.e. strong interaction effects for two subsequent strongly shifted and broadened transitions in a given nucleus. Such a study could give more information about a possible density dependence. We could also investigate the influence of the isovector part of the optical potential representing the difference in the radii of the distributions of protons and neutrons. It was therefore decided to reinvestigate some of the earlier studied atoms more accurately and to investigate some nuclei with Z -values around 80, where in some cases the more peripheral pionic 4f levels had already been investigated rather accurately (see e.g. Backenstoss [Bac 70]).

4.2 Experiments

The experimental set-up and data acquisition system for the measurement of pionic X-rays comprising two symmetric and two asymmetric BGO Compton suppression Ge spectrometers are described in chapter 2. The pionic X-ray spectra were studied for the isotopes ^{181}Ta , ^{187}Re , ^{195}Pt ,

^{197}Au , ^{208}Pb , ^{209}Bi and ^{237}Np , respectively. The experiments have been performed with pions of about 100 MeV/c. In the different experiments the number of stopped particles was between $(1 \text{ to } 6) \times 10^5 \pi^-/\text{s}$ at PSI (formerly SIN) and $1.5 \times 10^4 \pi^-/\text{s}$ at NIKHEF. The targets were metallic plates of the following elements and thicknesses (all in g/cm^2) ^{181}Ta (4.98), $^{\text{nat}}\text{Re}$ (2.10), $^{\text{nat}}\text{Pt}$ (4.29), ^{197}Au (3.86) and ^{209}Bi (4.87). The ^{208}Pb target consisting of 15 g of PbO and 20 g of $\text{Pb}(\text{NO}_3)_2$ was enriched to 99% in mass 208. The lead target is a powder kept in a plastic bag. The total target thickness as viewed from the γ -ray detector was about $4 \text{ g}/\text{cm}^2$. The ^{237}Np target was prepared and encapsulated in an Al casing by the European Institute for Transuranium Elements in Karlsruhe. The aluminum casing contained $0.92 \text{ g}/\text{cm}^2$ thick NpO_2 with a total of 9.981 g of ^{237}Np .

In the evaluation of the relative intensities of the pionic X-ray transitions, self-absorption in the different targets was taken into account. The energy calibration of the X-ray spectra were adjusted such that the energy scale was about 0.25 keV/channel, recorded over 8192 channels. In the final energy calibration, only nuclear γ -rays were used which were produced as a result of pion capture by the nucleus and occurring in coincidence with the prompt time window, this in order to avoid energy shifts. Also, pionic X-ray transitions not affected by the strong interaction have been used in the energy calibration.

4.2.1 Pionic atoms of the spherical nuclei $^{\text{nat}}\text{Pt}$, ^{197}Au , ^{208}Pb and ^{209}Bi

Ericson and Tauscher [Eri 82] suggested the possibility of a systematic underestimation of the experimental 3d widths in pionic ^{181}Ta and $^{185,187}\text{Re}$ as a consequence of these isotopes being strongly deformed nuclei. They assumed that the detailed hyperfine pattern and its distortion could not be correctly dealt with. Therefore, to study the strong interaction monopole parameters we selected nuclei with nuclear ground spins of $I^\pi < 1$, where no hyperfine splitting occurs. This requirement is fulfilled for all stable Pt isotopes and ^{208}Pb . In the case of the almost spherical nuclei ^{197}Au and ^{209}Bi the nuclear ground spins are $3/2^+$ and $9/2^-$, respectively. These spins in combination with the relatively small nuclear ground state quadrupole moments in these nuclei ($Q = 0.59 \text{ b}$ for Au, -0.37 b for Bi) yield a hyperfine splitting of the pionic X-ray transitions. The calculated electromagnetic hyperfine splitting (see section 3.6) between the main components of the $5g \rightarrow 4f$ and $4f \rightarrow 3d$ hyperfine complexes are 0.90 keV and 2.3 keV in ^{197}Au and 0.38 keV and 2.8 keV in ^{209}Bi . The contribution of the strong interaction to the splitting of those can be neglected for the present analysis.

4.2.1.1 Pionic ^{nat}Pt and ^{197}Au

The experiments on pionic ^{nat}Pt and ^{197}Au were performed at NIKHEF using pions of about 140 MeV/c. We do not show here pictures of the full X-ray spectra of pionic Pt and ^{197}Au since they closely resemble that of ^{208}Pb fully shown below; they can be found in our paper [Ach 84b]. For further details of the experiment we also refer to this paper.

The data for ^{197}Au have been reanalyzed with our new fit program described in chapter 2. Except for the pionic X-rays mainly γ -rays from $^{190-194}\text{Pt}$ isotopes occur in the spectrum coincident with the prompt time window. Many of these nuclear transitions are known to high precision (in the case of ^{192}Pt with an accuracy of about 15 meV). We used them to improve the energy calibration. For the gold target the $5g \rightarrow 4f$ and $4f \rightarrow 3d$ transitions were fit with and without hyperfine splitting to determine its influence on the analysis. The difference was found to be small compared to the experimental errors, which can be understood from the fact that the hyperfine splitting in the $4f \rightarrow 3d$ transition (of the order of 2.3 keV, see ref [Ach 84b] and fig 4.1) is only about half the experimental uncertainty in the value for the strong interaction width Γ_0 . We list the results of our fits for the strong interaction shifts and widths in table 4.1 and 4.2. To obtain the strong interaction width Γ_0 on the final pionic level the radiative width of initial and final states and the strong interaction width of the initial level have to be subtracted from the analyzed width of the pionic X-ray transition. The strong interaction shift of the final level is obtained by subtracting the calculated value for the transition energy of a point nucleus from the

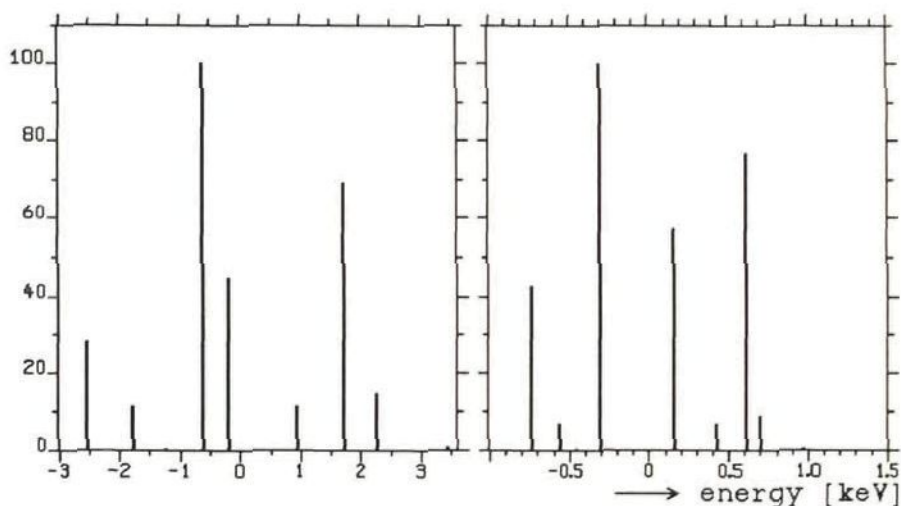


Fig. 4.1 Calculated relative intensities and positions in the hyperfine patterns of the pionic $4f-3d$ and $5g-4f$ transitions in ^{197}Au .

experimental result and adding the shift of the initial state to this value. We list the results of our fits for the strong interaction shifts and widths in tables 4.1 and 4.2. From the recorded spectra, also the X-ray intensities of the pionic cascade are derived. The relative X-ray intensities intensities for platinum and gold, corrected for the self-absorption in the targets, are also presented in tables 4.1 and 4.2, respectively.

Table 4.1: Data on pionic X-rays in ^{194}Pt , being calculated and experimental pionic transition energies, intensities and widths populating and depopulating the pionic 4f level. The calculations are for a point nucleus and include higher order corrections. The shifts and widths given for the 3d level have been corrected for the shifts and widths of the 4f level. The experimental widths in after correction for the radiative widths (see table 4.7) are presented in the last column.

transition $n_i - n_f$	energy		shift	relative intensity	Lorentzian width	
	E_{cal} keV	E_{exp} keV	ϵ keV	Y_{exp} %	Γ_{exp} keV	Γ_{corr} keV
4f - 3d	1137.64	1159.3 ± 1.7	22.8 ± 1.7	17.0 ± 0.8	38 ± 5	37 ± 5
5g - 4f	518.28	519.37 ± 0.04	1.09 ± 0.04	100 ± 7	0.74 ± 0.05	0.59 ± 0.05
6g - 4f	796.25	797.37 ± 0.08	1.12 ± 0.08	9.3 ± 0.5		
7g - 4f	963.96	964.4 ± 0.8	0.4 ± 0.8	4.1 ± 0.3		
8g - 4f	1072.75	1072.2 ± 1.5	-0.6 ± 1.5	0.8 ± 0.2		
9g - 4f	1147.25	1148.1 ± 1.5	0.9 ± 1.5	0.6 ± 0.2		
10g - 4f	1200.45			0.4 ± 0.2		

Table 4.2: Data on pionic X-rays in ^{197}Au . Explanation see table 4.1.

transition $n_i - n_f$	energy		shift	relative intensity	Lorentzian width	
	E_{cal} keV	E_{exp} keV	ϵ keV	Y_{exp} %	Γ_{exp} keV	Γ_{corr} keV
4f - 3d	1167.92	1187.3 ± 1.9	20.6 ± 1.9	14.4 ± 1.0	36 ± 4	34 ± 4
5g - 4f	531.88	533.13 ± 0.07	1.25 ± 0.07	100 ± 7	0.93 ± 0.04	0.77 ± 0.04
6g - 4f	817.05	818.38 ± 0.09	1.33 ± 0.09	10.9 ± 1.1		
7g - 4f	989.12	990.37 ± 0.15	1.25 ± 0.15	3.5 ± 0.4		
8g - 4f	1100.74	1101.4 ± 0.5	0.7 ± 0.5	1.3 ± 0.2		
9g - 4f	1177.17	1178.0 ± 0.8	0.8 ± 0.8	0.4 ± 0.2		
10g - 4f	1231.75	1233 ± 3	1.4 ± 2.6	0.08 ± 0.02		

4.2.1.2 Pionic ^{208}Pb

The investigation on the doubly-closed shell nucleus ^{208}Pb avoids the complication possibly introduced by deformed nuclei, discussed by Ericson and Tauscher [Eri 82], as it has a spherical shape without any nuclear deformation. The results on pionic ^{208}Pb have already been published separately [Laa 85]. Preliminary data on pionic ^{208}Pb from a TRIUMF group [Oli 85] had been presented at the PANIC conference in Heidelberg just after the completion of the present experiment at PSI.

In figure 4.2 we show the prompt part of the pionic X-ray spectrum up to 1600 keV on a logarithmic scale. This Compton suppressed spectrum is essentially free from delayed neutron-induced γ -ray background. Most other γ -rays are nuclear transitions in Tl isotopes occurring after pion capture in the ^{208}Pb nucleus. In figures 4.3 and 4.4 we display details of the same spectrum,

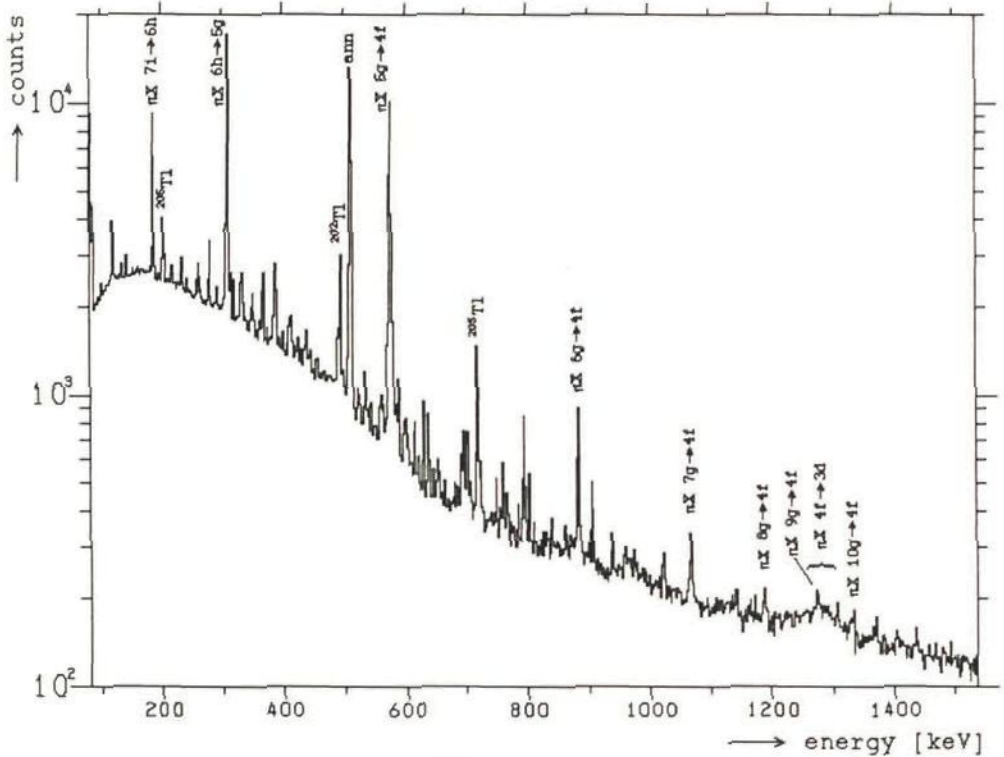


Fig. 4.2 The X-ray spectrum of pionic ^{208}Pb in the prompt part of the time distribution. The spectrum is thus essentially free from neutron induced γ -ray background. The main pionic X-rays have been indicated in the figure.

regarding the energy regions of the $5g \rightarrow 4f$ and the $4f \rightarrow 3d$ X-ray transitions, respectively. The solid lines represent the fits to the data points. Contrary to the analysis of ref. [Oli 85] we include in our fits all the transitions in the energy region of interest. This enables us to reduce systematic errors in the fits considerably. We estimate our systematic error to be 1.4 keV in the width of the $4f \rightarrow 3d$ transition as compared to 4.6 keV in ref. [Oli 85]. Our error is mainly caused by the uncertainty in the fit of the background.

Our data have been reanalyzed with our new fit program [Laa 88] described in chapter 2. The energy calibration was improved with respect to the one used in reference [Laa 85], where lines from a spectrum with a time cut on the neutrons were used. In the present calibration only γ -rays occurring in the prompt spectrum were used to avoid energy shifts due to time dependence of energy spectra (see par. 3.4 and ref. [Mat 80]). In table 4.3 the results of the pionic X-ray transitions are presented. The experimental energies of the pionic X-rays not influenced by the strong interaction are in good agreement with the calculated values.

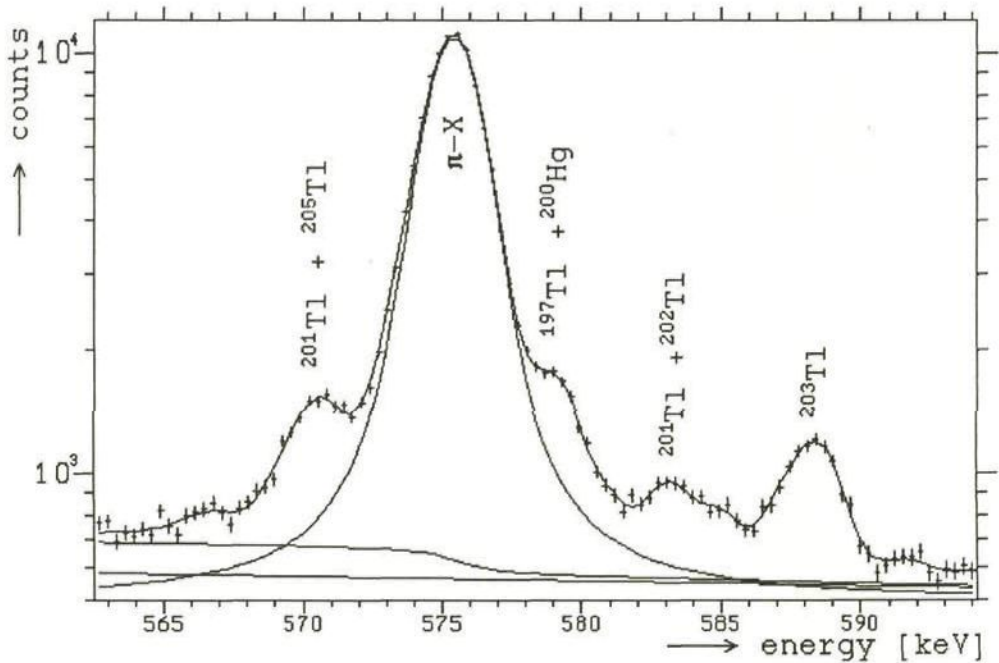


Fig. 4.3 The pionic $5g \rightarrow 4f$ transition in the X-ray spectrum from pions stopped in a ^{208}Pb target. The fit to the experimental points is represented by the solid line. The background including the step function is also displayed by a solid line in the figure.

In table 4.3 we also present the strong interaction shifts of the $4f$ and $3d$ levels, determined from the X-ray spectrum using a Lorentzian line-shape folded with the response function of the Ge detector. Leaving out the step function (see chapter 2) in the line shape makes in this particular case only a small difference of 4% in the width of the $4f \rightarrow 3d$ transition as no intense nuclear γ -rays disturb the fit. The background in the analysis of the $4f \rightarrow 3d$ transition was obtained by a fit of an exponential function over a large energy interval below and above (up to 2.5 MeV) the transition energy. On the high energy side (between 1330 and 1745 keV) the prompt spectrum shape is purely an exponential slope without any prominent peaks. This background was then used in the fits of the X-ray transition. We simultaneously made a fit of the $9g \rightarrow 4f$ and $10g \rightarrow 4f$ pionic X-rays and some nuclear Tl transitions, which coincided with the energy interval chosen for the fit. The result is shown in fig. 4.4. The reduced χ^2 of the fit is 1.02. The relative intensities of the pionic ^{208}Pb X-rays, given in table 4.3, were obtained in the same way as

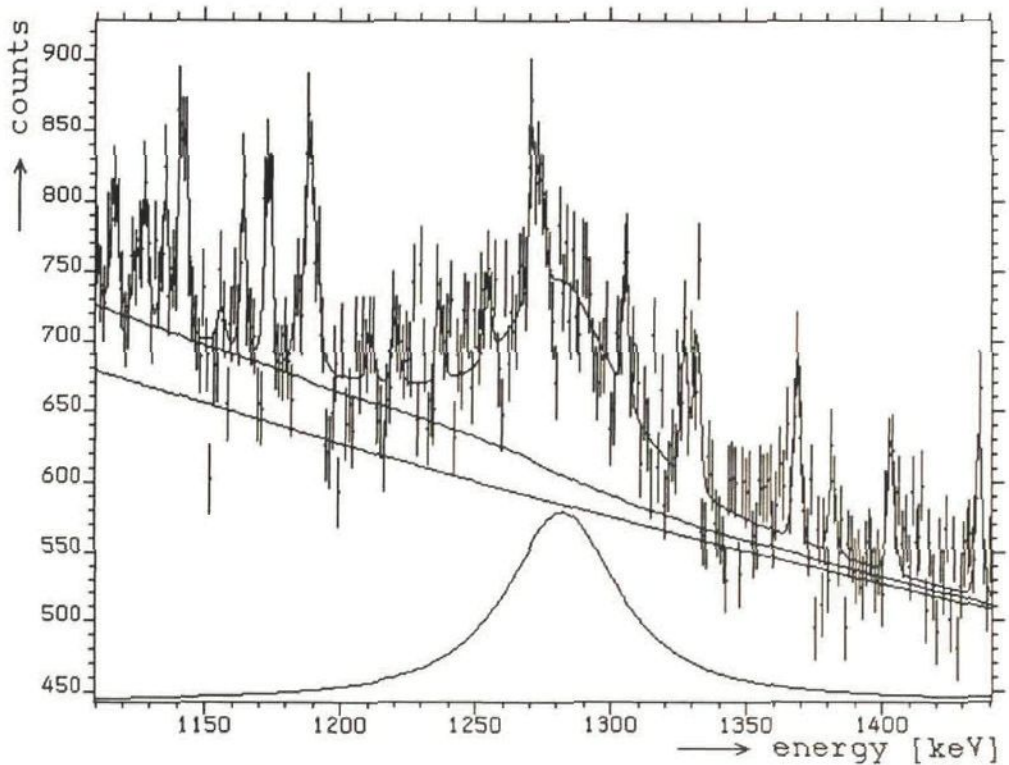


Fig. 4.4 This figure displays the energy region of the $4f \rightarrow 3d$ transition of the prompt pionic X-ray ^{208}Pb spectrum. The solid line represents the fit to the data points. The various γ -rays also included in the fitting procedure have been identified as transitions mainly in Tl isotopes in the mass region $A=200-205$.

described earlier taking the target self-absorption into account. From the intensity balance for the 4f level an independent strong interaction absorption width of this level was derived which agrees with the value given here (see table 4.8).

Table 4.3: Data on pionic X-rays in ^{208}Pb . Explanation see table 4.1. As an illustration, we here added data on higher transitions.

transition $n_i - n_f$	energy		shift	relative intensity	Lorentzian width	
	E_{cal} keV	E_{exp} keV	ϵ keV	Y_{exp} %	Γ_{exp} keV	Γ_{corr} keV
4f - 3d	1261.23	1282.3 \pm 2.2	22.7 \pm 2.2	8.7 \pm 0.6	48.8 \pm 3.6	47.1 \pm 3.6
5g - 4f	573.78	575.46 \pm 0.04	1.68 \pm 0.04	67.2 \pm 1.5	1.17 \pm 0.05	0.98 \pm 0.05
6g - 4f	881.14	882.93 \pm 0.12	1.79 \pm 0.12	5.7 \pm 0.5	1.16 \pm 0.10	0.97 \pm 0.10
7g - 4f	1066.62	1068.5 \pm 0.3	1.9 \pm 0.3	1.96 \pm 0.08		
8g - 4f	1186.94	1188.8 \pm 0.8	1.9 \pm 0.8	9.57 \pm 0.09		
9g - 4f	1269.33	1271.2 \pm 0.9	1.9 \pm 0.9	0.44 \pm 0.07		
8j - 7i	120.13	120.2 \pm 0.03				
7i - 6h	185.66	185.63 \pm 0.02		123 \pm 20		
9j - 7i	201.97	201.95 \pm 0.08		14 \pm 6		
9i - 7h	202.50	203.3 \pm 0.4		1.82 \pm 0.17		
6h - 5g	309.21	309.22 \pm 0.02		60.9 \pm 1.2		
7h - 5g	494.05	493.99 \pm 0.04		8.49 \pm 0.09		
8h - 5g	613.96	614.17 \pm 0.16		0.71 \pm 0.06		

4.2.1.3 Pionic ^{209}Bi

The π X-ray spectrum of pionic ^{209}Bi obtained by selecting the events from the prompt part of the time distribution is essentially free from neutron-induced γ -ray background as a consequence of the good separation in time-of-flight between neutrons and γ -rays. Most of the γ -rays are nuclear transitions in Pb isotopes occurring after pion capture in the ^{209}Bi nucleus.

Since the ^{209}Bi nucleus has an almost spherical shape, it has only a very small negative spectroscopic quadrupole moment of about -0.37 b [Bee 78]. In view of the rather large ground state spin $I^\pi = 9/2^+$ of ^{209}Bi the hyperfine splitting of the 4f and 3d levels are calculated as outlined in paragraph 3.8.2. The results, see fig. 4.5 and table B.8, were taken into account when fitting the data. Also the small corrections for the magnetic hyperfine structure have been applied.

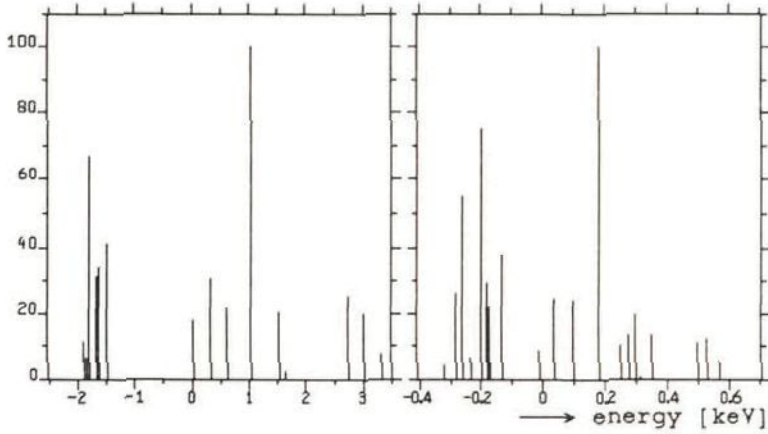


Fig. 4.5 Calculated relative intensities and positions in the hyperfine patterns of the pionic $4f-3d$ and $5g-4f$ transitions in ^{209}Bi .

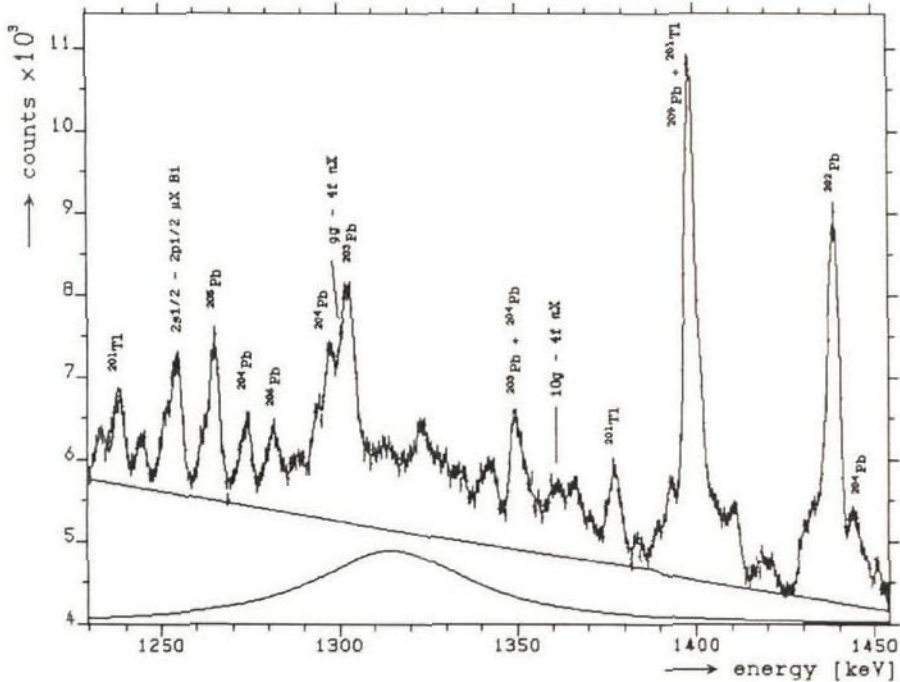


Fig. 4.6 This figure displays the $4f \rightarrow 3d$ hyperfine complex of the prompt pionic ^{209}Bi X-ray spectrum. The solid line represents the fit to the data points. Also shown are the background (see text) and the resulting $4f-3d$ line. The various γ -rays have been identified as transitions mainly in Pb and Tl isotopes in the mass region $A=200-208$ resulting from pion and muon capture.

The pionic $4f \rightarrow 3d$ transition in Bi has been fit over a rather large energy interval: 1230 keV - 1460 keV. We include the rather strong γ -rays at about 1400 and 1440 keV (see fig 4.6). The calculated quadrupole splitting between the dominant $^{15/2}(4f) \rightarrow ^{13/2}(3d)$ and $^{13/2}(4f) \rightarrow ^{11/2}(3d)$ transitions is 2.1 keV, much smaller than the line width of 50 keV and was therefore kept constant throughout the analysis. There are strong nuclear γ -rays present in the spectrum at about 1608 keV from ^{204}Pb and ^{209}Bi , which have their Compton edges in the energy region of the pionic $4f \rightarrow 3d$ transition. The shape of these Compton edges and their intensities as a fraction of the full energy peaks have been studied carefully as a function of energy in the calibration runs. These Compton edges have been included in the fit as a fixed background function. The inclusion of this background in the fit decreases the width of the pionic $4f - 3d$ transition by about 8%. This Compton edge is not taken into account by Olin et al [Oli 85], who do not include any nuclear γ -rays in their fit which extends up to an energy of only 1397 keV. These features help to explain why we feel justified in attaching a so much smaller error to our result for the 3d-width (see table 4.4).

Table 4.4: Data on pionic X-rays in ^{209}Bi . Explanation see table 4.1.

transition $n_i - n_f$	energy		shift	relative intensity	Lorentzian width	
	E_{cal} keV	E_{exp} keV	ϵ keV	Y_{exp} %	Γ_{exp} keV	Γ_{corr} keV
4f - 3d	1293.23	1311.5 ± 3.0	20.1 ± 3.0	4.59 ± 0.32	54 ± 4	52 ± 4
5g - 4f	588.11	589.89 ± 0.06	1.78 ± 0.06	42.10 ± 0.10	1.44 ± 0.09	1.24 ± 0.09
6g - 4f	903.06	904.77 ± 0.06	1.71 ± 0.06	4.8 ± 0.5		
7g - 4f	1093.11	1094.9 ± 0.6	1.81 ± 0.60	1.02 ± 0.15		
8g - 4f	1216.41	1217.24 ± 0.26	0.82 ± 0.26	0.44 ± 0.02		
9g - 4f	1300.84	1303.3 ± 0.3	2.5 ± 0.3	0.24 ± 0.02		
10g - 4f	1361.12	1362.1 ± 0.7	1.0 ± 0.7	0.10 ± 0.02		

4.2.2 Pionic atoms of the strongly deformed nuclei ^{181}Ta , $^{\text{nat}}\text{Re}$ and ^{237}Np

The isotopes ^{181}Ta , $^{\text{nat}}\text{Re}$ and ^{237}Np have strongly deformed nuclei with large nuclear ground state spins. The spectroscopic quadrupole moment of the nuclear ground state have been determined most accurately using muonic and pionic atoms [Kon 81, chapter 5]. By comparing the observed effective hyperfine splitting in pionic atoms with the electromagnetic hyperfine splitting in muonic atoms, the strong interaction quadrupole shift, ϵ_2 , about which very little information is available, can be obtained.

4.2.2.1 Pionic ^{181}Ta

In this case the influence of the hyperfine structure on the analysis is considerable, as a result of the large quadrupole moment. The spectroscopic quadrupole moment of the nuclear ground state in ^{181}Ta has been reported as $Q = 3.28 \pm 0.06$ b and 3.30 ± 0.06 b [Kon 81] from the measurements of the hyperfine splitting of the muonic and pionic $5g \rightarrow 4f$ complexes, respectively. The average value has been used to derive the relative intensities and electromagnetic energy differences of the individual members of the $5g \rightarrow 4f$ and $4f \rightarrow 3d$ multiplets. The resulting π X-ray patterns consist of twenty and fifteen members for the $5g \rightarrow 4f$ and $4f \rightarrow 3d$ multiplets, respectively (see fig. 4.7 and table B.9).

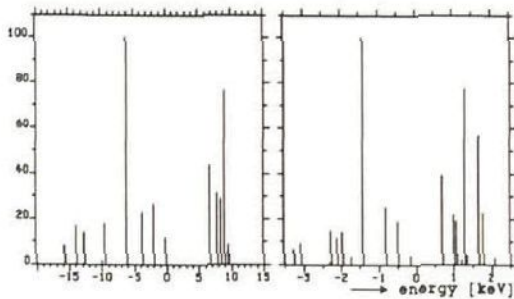


Fig. 4.7 Calculated hyperfine patterns of the pionic $4f - 3d$ and $5g - 4f$ transitions in ^{181}Ta .

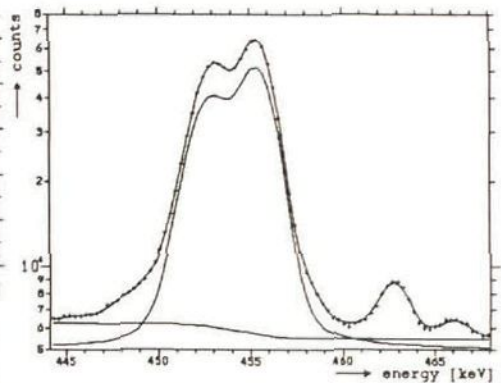


Fig. 4.8 The X-ray spectrum of the pionic $5g \rightarrow 4f$ hyperfine complex from pions stopped in a ^{181}Ta target.

The hyperfine complex of the $4f - 3d$ transition, causing it to extend over a large energy range where many Hafnium lines are present, makes Tantalum a very difficult target to measure. The prompt pionic X-ray spectrum from ^{181}Ta in the regions of the pionic $5g \rightarrow 4f$ and $4f \rightarrow 3d$ are shown in the figures 4.8 and 4.9. The neutron induced ^{70}Ge 1040 keV transition (generated by neutrons in the detector), which if not suppressed will disturb the analysis of the 1008 keV $4f \rightarrow 3d$ π X-ray transition, is effectively removed by the time of flight techniques.

The spectrum has been fit with the program described in chapter 2. To ensure the correct background and to extract the correct transition intensity of the hyperfine complex, the rather wide pionic $4f \rightarrow 3d$ multiplet was fit over an energy interval, ranging from 880 keV up to 1170 keV. The solid lines in the figures represent the fits to the data points. Large energy intervals have been used below and above the X-ray transitions to obtain a proper parametrization of the background. The energy calibration and the instrumental line shape as a function of energy was obtained from the study of nuclear γ -rays present in the same prompt spectrum.

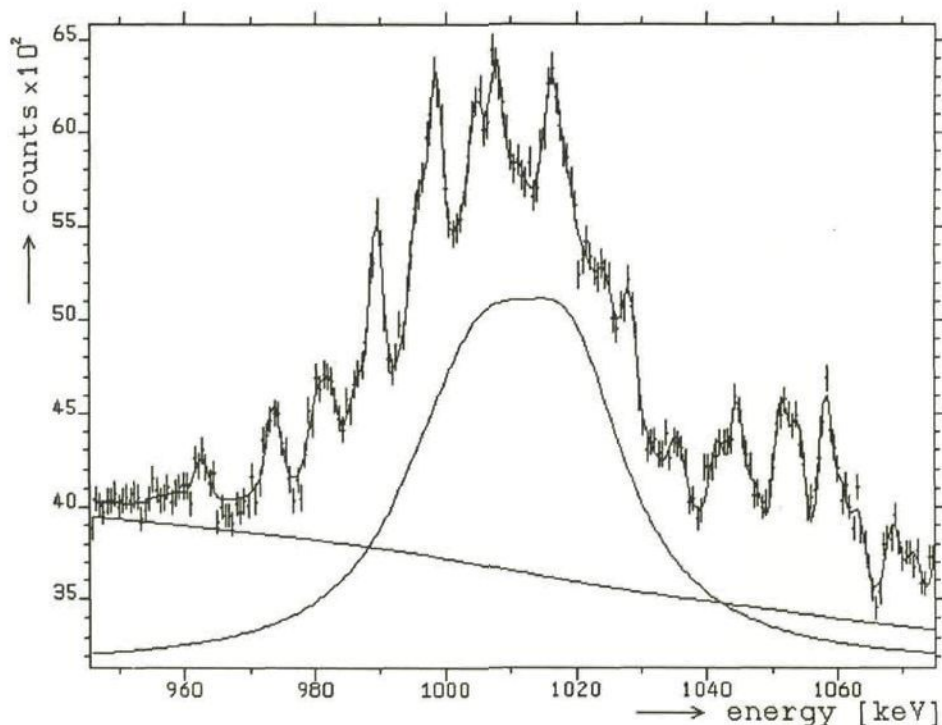


Fig. 4.9 The $4f \rightarrow 3d$ hyperfine complex of the prompt pionic ^{181}Ta X-ray spectrum. The solid line represents the fit to the data points. Also shown are the background (see text) and the resulting $4f-3d$ line. The various γ -rays have been identified as transitions mainly in Hf isotopes in the mass region $A=170-180$ resulting from pion capture.

From the energy calibration, as described above, we have determined the energies of the different pionic X-ray transitions. The ϵ_0 is then derived from a comparison between the experimental values and the calculated point Coulomb energy including higher order corrections as described above. The strong interaction widths of the 4f and 3d levels are extracted from the fit to the data of the pionic 5g \rightarrow 4f and 4f \rightarrow 3d transitions. Subtracting the radiative widths of initial and final level as well as the strong interaction width of the initial level, we obtain the strong interaction width Γ_0 of the final pionic level. The results are shown in table 4.5. A fit to the data was also made using the theoretical strong interaction width $\Gamma_0(3d) = 39$ keV. The χ^2 of the best fit deteriorated by more than a factor of two for this theoretically predicted level width.

Table 4.5: Data on pionic X-rays in ^{181}Ta . Explanation see table 4.1.

transition $n_i - n_f$	energy		shift	relative intensity	Lorentzian width	
	E_{cal} keV	E_{exp} keV	ϵ keV	Y_{exp} %	Γ_{exp} keV	Γ_{corr} keV
4f - 3d	992.75	1008.4 ± 1.3	16.2 ± 1.3	14.82 ± 0.66	20.9 ± 1.5	20.1 ± 1.5
5g - 4f	453.05	453.61 ± 0.04	0.56 ± 0.04	56.99 ± 2.60	0.43 ± 0.05	0.31 ± 0.05
6g - 4f	696.36	696.92 ± 0.06	0.56 ± 0.06	7.66 ± 0.23	0.44 ± 0.06	0.33 ± 0.06
7g - 4f	843.14	843.75 ± 0.14	0.61 ± 0.14	1.91 ± 0.56		
8g - 4f	938.35	938.5 ± 0.4	0.15 ± 0.4	0.87 ± 0.18		

To calculate the relative intensities of a hyperfine complex, the assumption is made that the pionic sublevels are statistically populated (see section 3.6). From the excellent fit of the hyperfine complexes to the data one may conclude that this assumption acceptable. The energy splitting ΔE between the two most intense (main) members of each hyperfine complex allows a determination of A_2^{eff} , the effective hyperfine structure constant. As the strong interaction is negligibly small for the pionic 5g level, we use the calculated value for $A_2^{\text{eff}}(5g)$ to evaluate the experimental value for $A_2^{\text{eff}}(4f)$, which in turn is used to derive $A_2^{\text{eff}}(3d)$.

The electromagnetic part of the quadrupole constant A_2 is calculated using eq. (3-35) and (3-36) and the above mentioned spectroscopic quadrupole moment Q , determined from muonic atoms. These values for A_2 and the experimental values are collected in table 4.14. The strong interaction quadrupole parameters $\epsilon_2(4f) = -0.18 \pm 0.03$ keV and $\epsilon_2(3d) = 1.9 \pm 0.3$ keV are then determined by using eq. (3-37). For the 4f level A_2 is practically unchanged from its point nuclear value (see appendix B, table 3) and the resulting $\epsilon_2(4f)$ does of course not depend on the

particular optical model chosen. The indicated errors in A_2^{eff} for the pionic 3d level also accounts for the experimental uncertainty and not for the variation of about 5% among the different models (see table 4.2) and the uncertainty in the value for the electromagnetic hyperfine splitting constant A_2 , due to the experimental error in the value for Q .

4.2.2.2 Pionic ^{nat}Re

Natural Re consists of the isotopes ^{185}Re and ^{187}Re with abundances 37.4% and 62.6%, respectively. Both isotopes have a nuclear ground state spin $I^\pi = 5/2^+$. The spectroscopic nuclear quadrupole moments have been determined using muonic and pionic atoms [Kon 81]. The ratio of the quadrupole moments of the two isotopes has been determined to a high precision with resonance methods, first by Semin and Bryukhova [Sem 68] and later by Segel [Seg 78], to be $^{185}Q/^{187}Q = 1.056709 \pm 0.000017$. Assuming the strong interaction quadrupole effects do effectively scale in the same way, the data have been fit with two hyperfine complexes which have the same centroid position but the above mentioned ratio for the splitting parameters. The 5g-4f and 4f-3d hyperfine complexes consists of 15 members each for both isotopes (see fig. 4.10).

The intensities and energy difference of the individual members of the pionic 5g \rightarrow 4f and 4f \rightarrow 3d multiplets relative to the $^{13/2} \rightarrow ^{11/2}$ and $^{11/2} \rightarrow ^{9/2}$ transitions, respectively, are given in table B.10. In Re the splitting between the $^{13/2}(5g) \rightarrow ^{11/2}(4f)$ and the $^{11/2}(5g) \rightarrow ^{9/2}(4f)$ hyperfine lines have been fit to be 1.98 ± 0.04 keV, while for the $^{11/2}(4f) \rightarrow ^{9/2}(3d)$ and the $^{9/2}(4f) \rightarrow ^{7/2}(3d)$

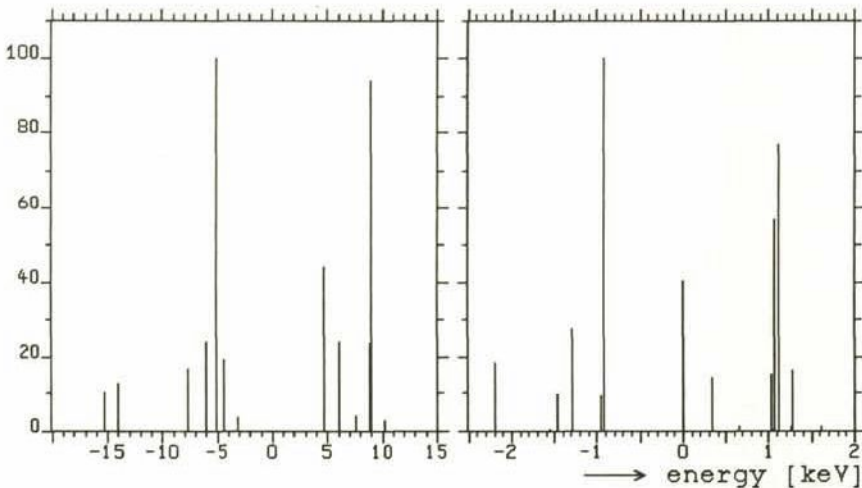


Fig. 4.10 Calculated hyperfine patterns of the pionic 4f - 3d and 5g - 4f transitions in ^{187}Re .

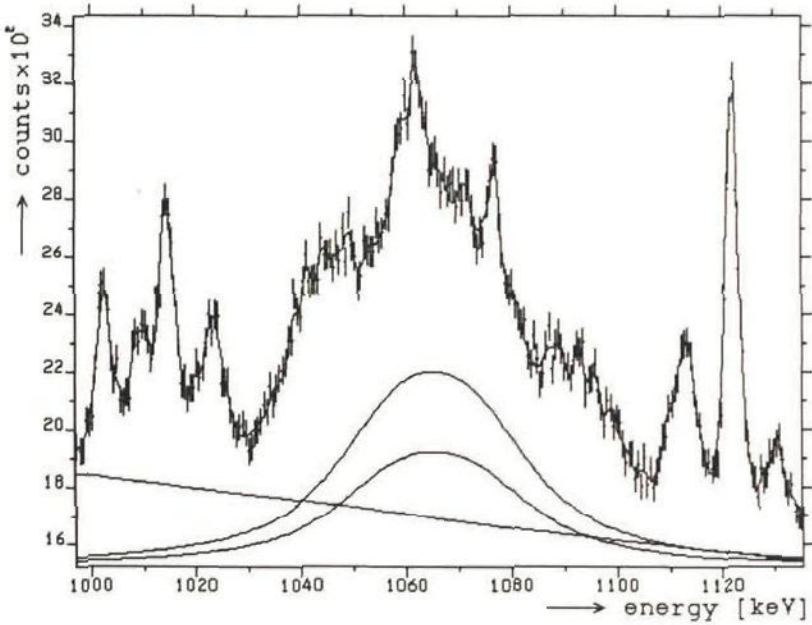


Fig. 4.11 Part of the prompt pionic X-ray ^{nat}Re spectrum, showing the energy region of the $4f \rightarrow 3d$ hyperfine complex. The solid line represents the fit to the data points. For each of the two Re isotopes, the corresponding Lorentzian function (actually hyperfine complex) is drawn. The various γ -rays also included in the fitting procedure have been identified as transitions mainly in W isotopes in the mass region $A=176-185$.

we obtain 13.8 ± 1.2 keV. In the same way as in the case of pionic ^{181}Ta , effective electric quadrupole constants $A_2^{\text{eff}}(4f) = 1.141 \pm 0.010$ keV and $A_2^{\text{eff}}(3d) = 5.97 \pm 0.19$ keV are evaluated from the least-squares fit to these complexes. From these we determine the strong interaction quadrupole constants $e_2(4f) = -0.024 \pm 0.015$ keV and $e_2(3d) = 0.51 \pm 0.34$ keV.

The prompt pionic X-ray spectrum in the region of the pionic $4f - 3d$ transition from ^{nat}Re is presented in fig. 4.11. The neutron induced transition in ^{70}Ge at 1040 keV is effectively eliminated by the time cut in the off-line data replay and does not disturb the analysis of the 1065 keV $4f \rightarrow 3d$ π X-ray transition. The pionic $4f \rightarrow 3d$ transition was fit over an energy interval, ranging from 1000 keV up to 1160 keV. On top of the broad hyperfine complex a large number of low intensity nuclear γ -ray transitions are situated most of which are identified as transitions in different Hf isotopes. From the energy calibration the energies of the different X-ray transitions are determined. The ϵ_0 is then derived from a comparison between the calculated point Coulomb energies with higher order corrections and the experimental values. The results of our fits for the strong interaction shifts and widths are presented in table 4.6.

Table 4.6: Data on pionic X-rays in ^{nat}Re . Explanation see table 4.1.

transition $n_i - n_f$	energy		shift	relative intensity	Lorentzian width	
	E_{cal} keV	E_{exp} keV	ϵ keV	Y_{exp} %	Γ_{exp} keV	Γ_{corr} keV
4f - 3d	1049.45	1065.3 ± 1.3	16.6 ± 1.3	7.8 ± 0.5	23.4 ± 1.5	22.5 ± 1.5
5g - 4f	478.59	479.35 ± 0.04	0.76 ± 0.04	49.1 ± 1.4	0.54 ± 0.06	0.41 ± 0.06
6g - 4f	735.49	736.30 ± 0.15	0.81 ± 0.15	4.95 ± 0.38		
7g - 4f	890.47	891.41 ± 0.40	0.94 ± 0.40	1.33 ± 0.10		
8g - 4f	991.01	992.63 ± 0.60	1.62 ± 0.60	0.52 ± 0.03		
9g - 4f	1059.85	1061.18 ± 0.80	1.33 ± 0.80	0.13 ± 0.02		

4.2.2.3 Pionic ^{237}Np

From the hyperfine splitting of muonic X-rays the spectroscopic nuclear quadrupole moment value $Q = 3.886 \pm 0.006$ b was derived, see chapter 5 and [Laa 87a]. Here we report on a measurement of the pionic $5g \rightarrow 4f$ X-ray complex in ^{237}Np (see fig. 4.12). The pionic ^{237}Np X-ray spectrum has not been investigated before.

The ^{237}Np nucleus is strongly deformed, which permits a valuable study of the π -nucleus strong interaction quadrupole effects. We can only analyze the hyperfine structure of the pionic $5g \rightarrow 4f$ complex since the transitions to the 3d level cannot be seen. The fit is made in the same way as described above. Subtracting from the fitted values the radiative widths of initial and final levels, we obtain a width $\Gamma_0(4f) = 3.88 \pm 0.26$ keV. The strong interaction monopole shift is $\epsilon_0(4f) = 5.26 \pm 0.14$ keV (with respect to the point Coulomb energy).

The other quantity that can be studied in strongly deformed nuclei interaction like the present one is the strong interaction quadrupole shift, $\epsilon_2(4f)$, a parameter about which very little information is available. We obtain an effective electric quadrupole constant value $A_2^{\text{eff}}(4f) = 3.80 \pm 0.08$ keV from the analysis of the observed hyperfine splitting of the pionic $5g \rightarrow 4f$ transition of the strongly deformed ^{237}Np nucleus. This quantity is directly proportional to the effective spectroscopic quadrupole moment, Q^{eff} . From the difference with the value $A_2(4f) = 4.295$ keV calculated from the electromagnetic quadrupole moment, a strong interaction quadrupole shift value $\epsilon_2(4f) = +0.49 \pm 0.08$ keV is obtained. The formulae for calculating the quadrupole moment from experimental data for muonic and pionic atoms can be found in chapter 3, section 3.6. In table 4.14 we compare our experimental values with theory.

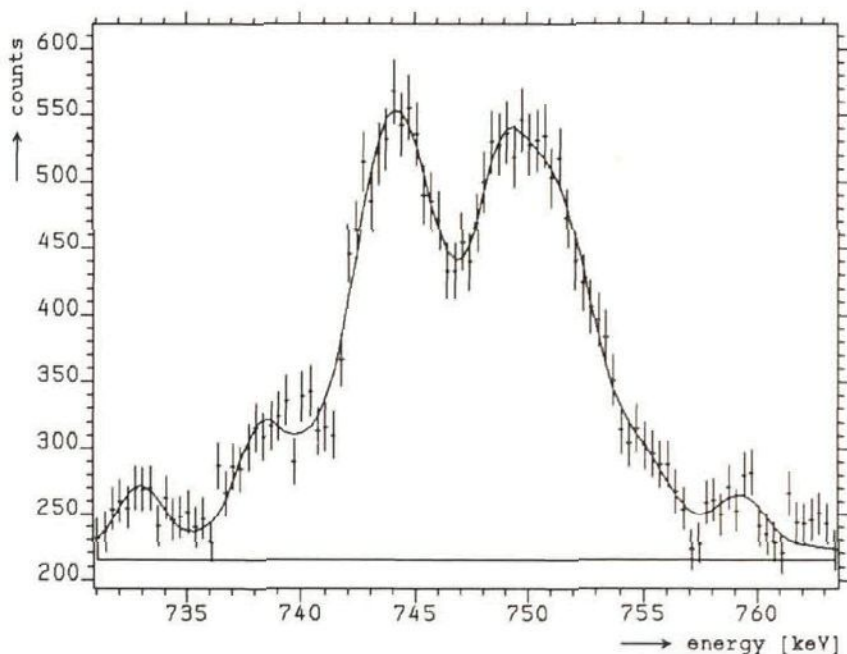


Fig. 4.12 Part of the prompt pionic X-ray ^{237}Np spectrum, showing the energy region of the $5g \rightarrow 4f$ hyperfine complex. The solid line represents the fit to the data points.

4.3 Strong interaction level widths from intensity balances

From the recorded spectra, we obtained the X-ray intensities of the transitions of the pionic cascade (see tables 4.1 - 4.6). These intensities have been obtained by using the efficiency curve discussed in chapter 2, corrected for self-absorption in the target. Since the solid angle of the Ge-detector viewing the target is only about 2 msr, the variation of the target thickness with respect to viewing angle can be neglected. The observed relative pionic X-ray intensities are usually in good agreement with predictions from the cascade computer code STARKEF [Tau 78]. The intensity balance of a pionic level is obtained from these intensities, except for intensities of the weaker not observed transitions feeding into the level which are approximated from cascade calculations. Given the relative intensities I of the pionic X-rays populating and depopulating a certain orbit, the strong interaction width Γ_0 of the (n, l) level can be determined by looking at the level's intensity balance, using the following relation

$$\Gamma_0^{n,l} = \Gamma_{\text{rad}}^{n,l} \left\{ \frac{\sum_{n',l'} I[(n',l') \rightarrow (n,l)] - I[(n,l) \rightarrow (n-1,l-1)]}{I[(n,l) \rightarrow (n-1,l-1)]} \right\} \quad (4-1)$$

where $\Gamma_{\text{rad}}^{n,l}$ is the electromagnetic radiative width given in table 4.7 for the investigated atoms. In our cases the Auger rates can be neglected as compared to the radiative width of the 5g and 4f levels. The strong interaction widths obtained in this fashion for the 4f levels are shown in tables 4.8. They are in good agreement with the widths determined directly from line shapes.

Table 4.7: Radiative width Γ_{rad} of the pionic levels in the isotopes investigated.

Nucleus	$\Gamma_{\text{rad}}(5g)$ eV	$\Gamma_{\text{rad}}(4f)$ eV	$\Gamma_{\text{rad}}(3d)$ eV
^{181}Ta	25.7	90.9	369.9
$^{\text{nat}}\text{Re}$	28.8	101.4	411.9
$^{\text{nat}}\text{Pt}$	33.8	120.9	481.7
^{197}Au	35.7	126.1	507.1
^{208}Pb	41.5	146.8	587.6
^{209}Bi	43.7	156.2	617.3
^{237}Np	70.9	207.3	-

Table 4.8: Comparison of strong interaction widths obtained from intensity balance with direct measurements.

nucleus	level	from intensity balance keV	from direct measurement keV
^{181}Ta	4f	0.33 ± 0.02	0.31 ± 0.05
$^{\text{nat}}\text{Re}$	4f	0.47 ± 0.04	0.41 ± 0.06
$^{\text{nat}}\text{Pt}$	4f	0.69 ± 0.10	0.59 ± 0.05
^{197}Au	4f	0.89 ± 0.13	0.77 ± 0.04
^{208}Pb	4f	1.18 ± 0.09	0.98 ± 0.05
^{208}Pb	5g	0.002 ± 0.001	0.003 (from theory)
^{209}Bi	4f	1.50 ± 0.20	1.24 ± 0.09

4.4 Discussion and conclusions

4.4.1 Strong interaction monopole shifts and widths

The results of our analysis for the strong interaction shifts, ϵ_0 , and widths, Γ_0 , are presented in table 4.9 and 4.10. In figs 4.13 and 4.14 we illustrate the Z dependence of ϵ_0 and Γ_0 for the pionic 3d level and compare these data with calculated values using different parameter sets for the optical potential.

For the pionic 4f states, the parameter set of Batty et al. [Bat 79] agrees reasonably well with the observed data as can be seen in table 4.9 and 4.10. These 4f states are dominated by the velocity-dependent non-local term of the optical potential. On the other hand, the picture is completely different for 3d states where an anomaly is observed, see also figs 4.13 and 4.14. We observe that the data establish a clear discrepancy between theory and experiment for the deeply bound 3d states whereas the 4f levels agree reasonably well. The results of experiments on pionic 1s orbits [Dav 87] demonstrate that Γ_0 for Mg, Al and Si also shows similar discrepancies as those in the 3d case.

Olivier et al. [Oli 84] have made an attempt to relate these anomalous narrow widths to an increase in s-wave repulsion in the optical potential. The parameter set of Seki and Masutani [Sek 83] essentially describes the same s-wave repulsion as suggested by Olivier et al. The result of these parameter sets are also included in the tables and figures. The result of their calculations come closest to the experimental widths for the 3d levels. Recently Wright et al. [Wri 87] at the PANIC 1987 conference in Kyoto reported on low-energy elastic scattering experiments of π^\pm on ^{58}Ni and ^{40}Ca at 30 and 20 MeV at LAMPF. They obtain a better agreement between the π^- scattering data and theory if the parameter set [Sek 83] used in the optical potential is adjusted so that it confirms the data presented in this work. They conclude that the evidence of pionic-atom anomalies agrees with that of in the π^- scattering data. We must remark, however, that this set destroys the agreement for the pionic 4f data on the shifts.

In contrast to the 4f levels, the deeply bound 3d levels in e.g. Pt, Au, ^{208}Pb and ^{209}Bi are influenced not only by the p-wave interaction but also to a large extent by the local s-wave interaction. This can best be illustrated as follows. We calculate that the contribution to ϵ_0 from s- and p wave terms for the case of ^{208}Pb are $\epsilon_0(\text{s-wave}) = -71.6$ keV and $\epsilon_0(\text{p-wave}) = +110.5$ keV, respectively, showing a somewhat delicate balance between the two terms.

The agreement between the present experimental values for pionic ^{208}Pb and those reported by Olin et al. [Oli 85] is reasonably good. Yet, they report that their values agree with theory. The reason is that they not only claim comparatively large systematic errors (0.05 keV and 1.0 keV for

Table 4.9: Strong interaction monopole shifts for pionic 4f and 3d levels with respect to the calculated point Coulomb energy. In the calculations the values of c_p and c_n for the Fermi distributions are taken to be equal. For Er a value of $c_p = c_n = 6.174$ was taken.

Nucleus	ref.	experiment keV	optical potential calculation			
			[Tau 71] _{$\xi=0$}	[Tau 71] _{$\xi=1$}	[Bat 79]	[Sek 83]
$\epsilon_0(4f)$ in keV						
^{166}Er	[Tan 84]	0.30 ± 0.03	0.288	0.274	0.292	0.265
^{168}Er	[Tan 84]	0.30 ± 0.03	0.288	0.274	0.292	0.265
^{181}Ta	[Bat 81]	0.54 ± 0.03	0.568	0.524	0.539	0.473
^{181}Ta	[Kon 81]	0.50 ± 0.11	0.568	0.524	0.539	0.473
^{181}Ta	this work	0.56 ± 0.04	0.568	0.524	0.539	0.473
$^{\text{nat}}\text{Re}$	[Kon 81]	0.67 ± 0.04	0.743	0.680	0.700	0.618
$^{\text{nat}}\text{Re}$	this work	0.76 ± 0.04	0.743	0.680	0.700	0.618
$^{\text{nat}}\text{Pt}$	[Ach 84b]	1.09 ± 0.04	1.095	1.020	1.064	0.956
^{197}Au	[Ach 84b]	1.25 ± 0.07	1.217	1.132	1.178	1.054
^{208}Pb	[Oli 85]	$1.66 \pm 0.02 \pm 0.05$	1.779	1.613	1.657	1.480
^{208}Pb	this work	1.68 ± 0.04	1.779	1.613	1.657	1.480
^{209}Bi	[Oli 85]	$1.79 \pm 0.05 \pm 0.04$	1.960	1.794	1.850	1.651
^{209}Bi	[Bat 81]	1.74 ± 0.06	1.960	1.794	1.850	1.651
^{209}Bi	[Kon 81]	1.77 ± 0.15	1.960	1.794	1.850	1.651
^{209}Bi	this work	1.78 ± 0.06	1.960	1.794	1.850	1.651
^{237}Np	this work	5.26 ± 0.14	5.279	4.681	4.541	3.792
$\epsilon_0(3d)$ in keV						
^{166}Er	[Tan 84]	15.6 ± 0.3	20.7	17.4	16.6	13.6
^{168}Er	[Tan 84]	14.6 ± 0.3	20.7	17.4	16.6	13.6
^{181}Ta	this work	16.2 ± 1.3	27.0	21.2	17.8	11.1
$^{\text{nat}}\text{Re}$	this work	16.6 ± 1.3	32.1	24.8	21.0	13.7
$^{\text{nat}}\text{Pt}$	[Ach 84b]	22.8 ± 1.7	38.1	29.6	26.0	18.7
^{197}Au	[Ach 84b]	20.6 ± 1.9	39.5	30.5	26.5	18.3
^{208}Pb	[Oli 85]	$16.1 \pm 0.6 \pm 1.0$	46.8	33.5	27.2	17.5
^{208}Pb	[Laa 85]	22.7 ± 2.2	46.8	33.5	27.2	17.5
^{209}Bi	[Oli 85]	$20.6 \pm 1.8 \pm 3.0$	47.6	34.5	28.2	17.7
^{209}Bi	this work	20.1 ± 3.0	47.6	34.5	28.2	17.7

Table 4.10: Strong interaction absorption widths for pionic 4f and 3d levels.

Nucleus	ref.	experiment keV	optical potential calculation			
			[Tau 71 $_{\xi=0}$]	[Tau 71 $_{\xi=1}$]	[Bat 79]	[Sek 83]
$\Gamma_0(4f)$ in keV						
^{181}Ta	this work	0.31 ± 0.05	0.378	0.324	0.339	0.287
$^{\text{nat}}\text{Re}$	this work	0.41 ± 0.06	0.517	0.430	0.444	0.377
$^{\text{nat}}\text{Pt}$	[Ach 84b]	0.59 ± 0.05	0.739	0.624	0.664	0.551
^{197}Au	[Ach 84b]	0.77 ± 0.04	0.85	0.715	0.736	0.626
^{208}Pb	[Oli 85]	$1.11 \pm 0.03 \pm 0.08$	1.351	1.085	1.091	0.926
^{208}Pb	this work	0.98 ± 0.05	1.351	1.085	1.091	0.926
^{209}Bi	[Oli 85]	$1.29 \pm 0.02 \pm 0.04$	1.485	1.217	1.228	1.038
^{209}Bi	this work	1.24 ± 0.09	1.485	1.217	1.228	1.038
^{237}Np	[Laa 86]	3.88 ± 0.26	5.070	4.133	4.006	3.235
$\Gamma_0(3d)$ in keV						
^{166}Er	[Tan 84]	19.4 ± 1.0	29.0	24.6	23.3	19.4
^{181}Ta	this work	20.1 ± 1.5	50.0	42.1	38.5	30.4
$^{\text{nat}}\text{Re}$	this work	22.5 ± 1.5	60.9	50.2	45.4	36.2
$^{\text{nat}}\text{Pt}$	[Ach 84b]	37 ± 5	73.0	61.5	55.3	45.1
^{197}Au	[Ach 84b]	34 ± 4	80.3	67.3	60.4	48.8
^{208}Pb	[Oli 85]	$47.4 \pm 2.6 \pm 4.6$	104.4	84.3	73.9	60.4
^{208}Pb	[Laa 85]	47.1 ± 3.6	104.4	84.3	73.9	60.4
^{209}Bi	[Oli 85]	$71.2 \pm 8.4 \pm 21$	109.9	90.5	79.4	64.3
^{209}Bi	this work	52 ± 4	109.9	90.5	79.4	64.3

the shifts and 0.08 keV and 4.6 keV for the widths of the 4f and 3d levels, respectively) but also add statistical and systematic errors to obtain a standard deviation, and then state that the experimental values for the 3d level are only three standard deviations off the theoretical value. In our opinion, multiplication of a systematic error by a factor of three, in this case 4.6 keV for the error in $\Gamma_0(3d)$, is not correct. We claim, therefore, that the data of Olin et al. [Oli 85] also disagree with theory. Also, due to our better way of analyzing the data (see above) we feel justified to claim much smaller systematic errors.

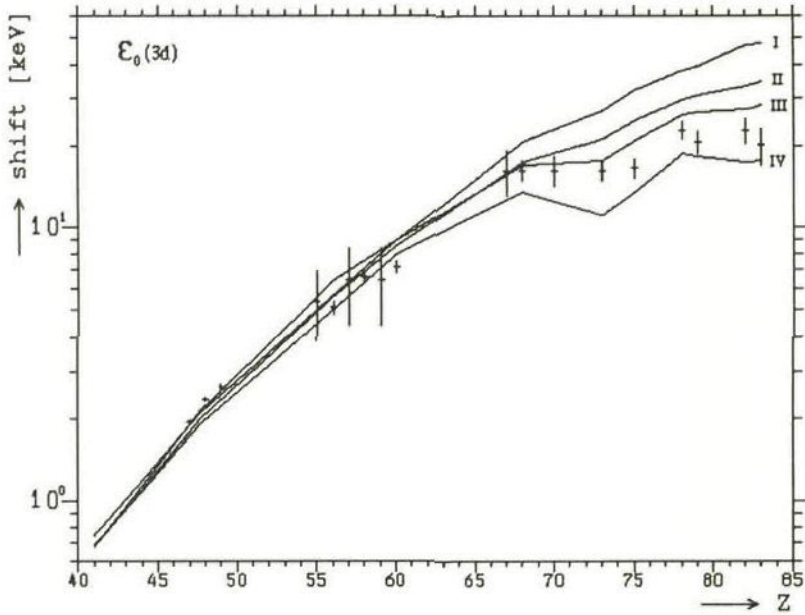


Fig. 4.13 The strong interaction shifts ϵ_0 versus atomic charge Z . The lines represent the different parameter sets: I = [Tau 71 $\xi_{=0}$], II = [Tau 71 $\xi_{=1}$], III = [Bat 79], IV = [Sek 83].

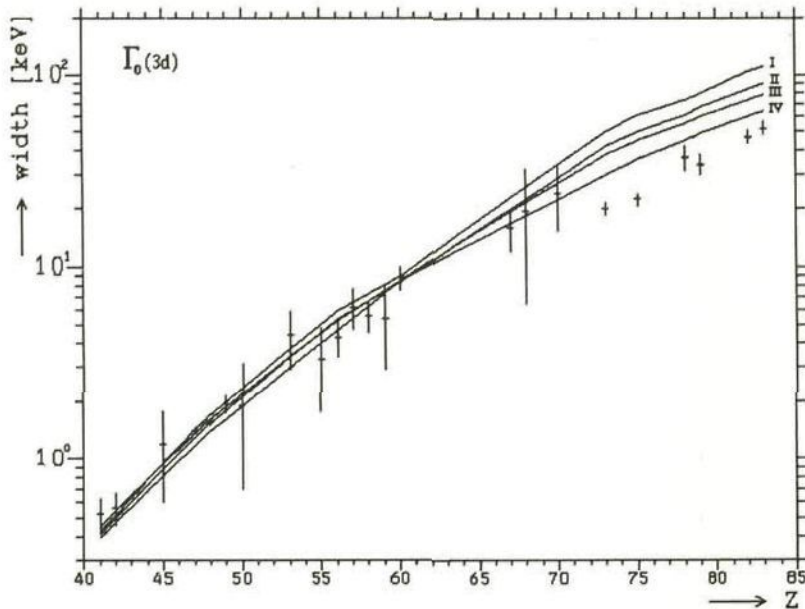


Fig. 4.14 Strong interaction widths Γ_0 versus atomic charge Z . The lines represent the different parameter sets: I = [Tau 71 $\xi_{=0}$], II = [Tau 71 $\xi_{=1}$], III = [Bat 79], IV = [Sek 83].

4.4.2 Extension of optical potential terms

In the theoretical considerations, the parameter c_p for the proton and c_n for the neutron Fermi distributions in the nucleus have until now been taken equal. For light nuclei, for which the semi-empirical optical potential has been used to fit the strong interaction shifts and widths, the differences between proton and neutron density distributions are indeed small and hardly influence the parameters in these nuclei. We will here investigate whether taking these quantities into account for our heavier elements may explain the "discrepancy". In the formalism given in chapter 3 the expressions for the radial neutron and proton distributions $\rho_n(r)$ and $\rho_p(r)$ are therefore kept distinct. In general $\rho_p(r)$ is deduced from experimental charge distributions obtained in muonic atom and electron-scattering experiments by unfolding the nucleon charge form factors.

The difference of the neutron and proton matter distribution has been investigated by Hoffman et al. [Hof 80] using the results from scattering of 1 GeV protons. The values for the half-density radii in the Fermi distributions of the protons and neutrons, c_p and c_n respectively, result in a difference of rms radii $\Delta r_{np} = 0.14 \pm 0.04$ fm. Hartree-Fock calculations by Angeli et al. [Ang 80] gave a somewhat larger value for the difference of about 0.20 fm. The calculations by Negele and Vautherin [Neg 72] also result in a difference of about 0.20 fm. In table 4.11 we compare the strong interaction monopole shifts and widths with respect to the standard optical potential calculations for pionic 4f and 3d levels for the different parameter sets, using Fermi distributions with $c_p = c_n$ and with $c_p - c_n = 0.14$ fm, respectively. One notices that shifts and widths are indeed reduced, resulting in a better agreement with experiment.

In table 4.11 we also give the χ^2 values between the experimental and theoretical values for the strong interaction shifts ϵ_0 and widths Γ_0 for the parameter sets [Tau 71 $_{\xi=0}$], [Tau 71 $_{\xi=1}$], [Bat 79] and [Sek 83] with $c_p = c_n$ (case A) and for $c_p - c_n = 0.14$ fm (case B). In this table one finds the χ^2 for each parameter set as well as for each pionic level. For the 4f level shifts there is no preference between the cases A and B, except for set [Seki 83] (the largest contribution to χ^2 originates from the ^{237}Np values, which may be due to the somewhat arbitrarily chosen difference of $\Delta c_{np} = 0.14$ fm being not optimal for this nucleus). For the 4f level widths we calculate an improvement in χ^2 for set [Tau 71 $_{\xi=0}$], while the other sets show no preference. For the 3d orbits the largest improvements in χ^2 are observed. In total, a better agreement of the calculated values with the experimental results by almost a factor of two for $c_p - c_n = 0.14$ fm. For a special case, ^{208}Pb , we show in fig. 4.15 the influence of increasing values of Δc_{np} in a plot of shifts versus widths. Though indeed a somewhat better agreement is reached for Δc_{np} , the situation is still not satisfactory.

Table 4.11: Strong interaction monopole shifts and widths compared to the two models, one where $c_n=c_p$ and one where $c_n=c_p+0.14$.

experiment	$c_n=c_p$		$c_n=c_p+0.14$					
	[Tau 71 $\xi_{=0}$]	[Tau 71 $\xi_{=1}$]	[Bat 79]	[Sek 83]				
$\epsilon_0(4f)$	^{181}Ta	0.56 \pm 0.04	0.57	0.54	0.47	0.57	0.53	0.46
	^{nat}Re	0.76 \pm 0.04	0.74	0.68	0.70	0.62	0.75	0.69
	^{nat}Pt	1.09 \pm 0.04	1.10	1.02	1.06	0.96	1.09	1.04
	^{197}Au	1.25 \pm 0.07	1.22	1.13	1.18	1.05	1.22	1.14
	^{208}Pb	1.68 \pm 0.04	1.78	1.61	1.66	1.48	1.77	1.61
	^{209}Bi	1.78 \pm 0.06	1.96	1.79	1.85	1.65	1.95	1.80
	^{237}Np	5.26 \pm 0.14	5.28	4.68	4.54	3.79	5.20	4.32
	^{181}Ta	16.2 \pm 1.3	27.0	21.2	17.8	11.1	23.5	13.8
	^{nat}Re	16.6 \pm 1.3	32.1	24.8	21.0	13.7	27.9	16.2
	^{nat}Pt	22.8 \pm 1.7	38.1	29.6	26.0	18.7	32.8	26.0
$\epsilon_0(3d)$	^{197}Au	20.6 \pm 1.9	39.5	30.5	26.5	18.3	33.8	26.6
	^{208}Pb	22.7 \pm 2.2	46.8	33.5	27.2	17.5	39.5	28.3
	^{209}Bi	20.1 \pm 3.0	47.6	34.5	28.2	17.7	39.7	29.0
	^{181}Ta	0.31 \pm 0.05	0.378	0.324	0.339	0.287	0.347	0.314
	^{nat}Re	0.41 \pm 0.06	0.517	0.430	0.444	0.377	0.473	0.429
$\Gamma_0(4f)$	^{nat}Pt	0.59 \pm 0.05	0.739	0.624	0.664	0.551	0.683	0.610
	^{197}Au	0.77 \pm 0.04	0.850	0.715	0.736	0.626	0.785	0.699
	^{208}Pb	0.98 \pm 0.05	1.351	1.085	1.091	0.926	1.241	1.060
	^{209}Bi	1.24 \pm 0.09	1.485	1.217	1.228	1.038	1.369	1.186
	^{237}Np	3.88 \pm 0.26	5.070	4.133	4.006	3.235	4.676	3.850
	^{181}Ta	20.1 \pm 1.5	50.0	42.1	38.5	30.4	44.8	40.4
	^{nat}Re	22.5 \pm 1.5	60.9	50.2	45.4	36.2	54.4	48.1
$\Gamma_0(3d)$	^{nat}Pt	37 \pm 5	73.0	61.5	55.3	45.1	66.3	58.9
	^{197}Au	34 \pm 4	80.3	67.3	60.4	48.8	72.6	64.6
	^{208}Pb	47.1 \pm 3.6	104.4	84.3	73.9	60.4	93.4	80.6
	^{209}Bi	52 \pm 4	109.9	90.5	79.4	64.3	99.0	86.7
	$\Sigma\chi^2(\epsilon_0^{4f})$	2.2	4.4	4.4	4.6	25	2.0	4.4
	$\Sigma\chi^2(\epsilon_0^{3d})$	99	99	24	6.3	5.6	49	8.3
$\Sigma\chi^2(\Gamma_0)$	$\Sigma\chi^2(\epsilon_0)$	47	14	14	5.4	16	24	6.2
	$\Sigma\chi^2(\Gamma_0^{4f})$	14	1.1	1.1	1.3	3.8	6.3	0.9
	$\Sigma\chi^2(\Gamma_0^{3d})$	283	141	141	90	28	192	118
	$\Sigma\chi^2(\Gamma_0)$	139	66	66	42	15	92	55
	$\Sigma\chi^2$	93	40	40	24	16	58	31

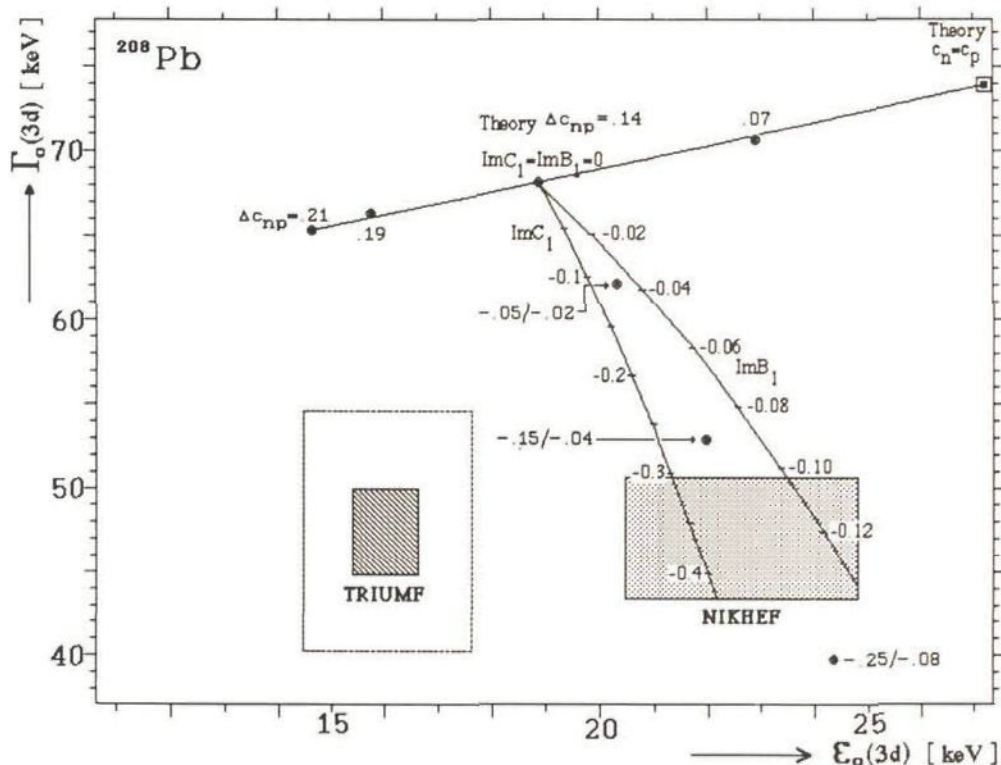


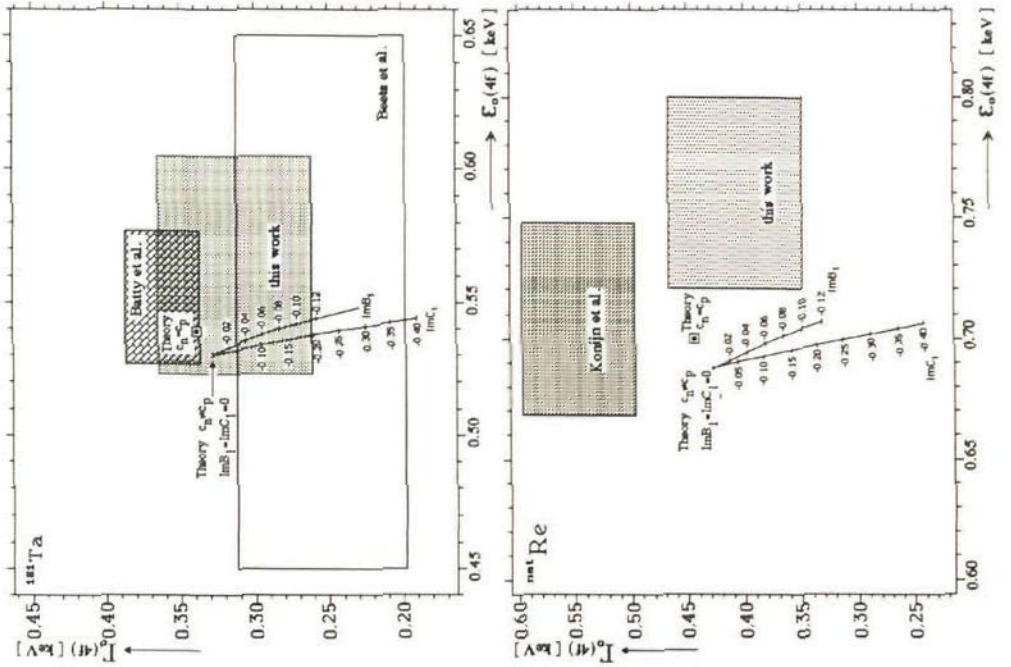
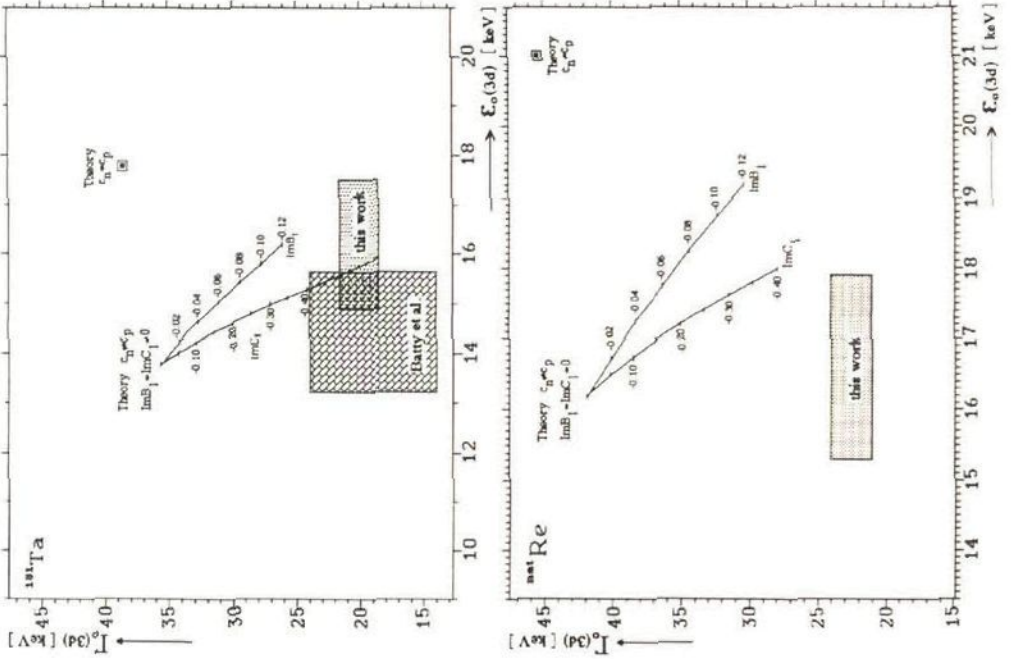
Fig. 4.15 Experimental and theoretical data on pionic ^{208}Pb , in a plot of widths versus shifts. The square point gives the theoretical value for $c_n = c_p$ (using the parameter set of Batty et al. [Bat 79]). The horizontal line shows the linear behaviour of the results for different c_n and c_p values but zero isovector absorption terms. Starting from the calculation for $c_n - c_p = 0.14$ fm the influences for non zero $\text{Im}B_1$ and $\text{Im}C_1$ are shown (lines for only one of both differing from zero, points for three combinations of non-zero terms). The inner rectangle of the TRIUMF data represents their data + statistical error, the outer represents data + statistical + systematical error.

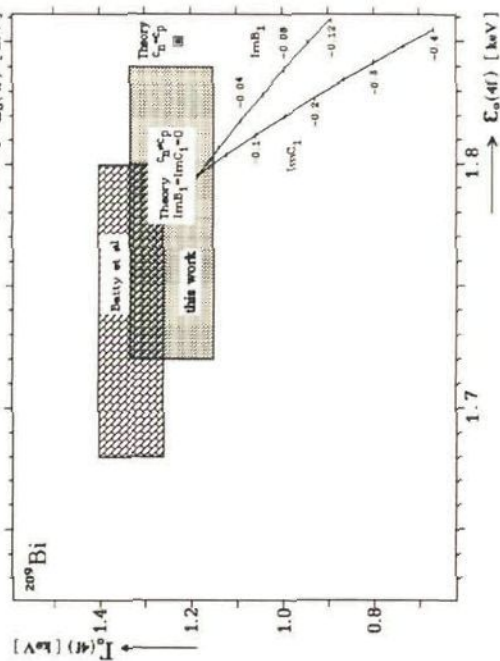
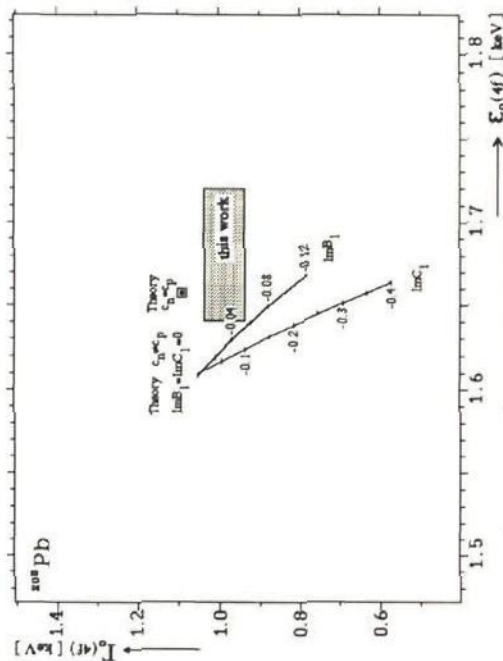
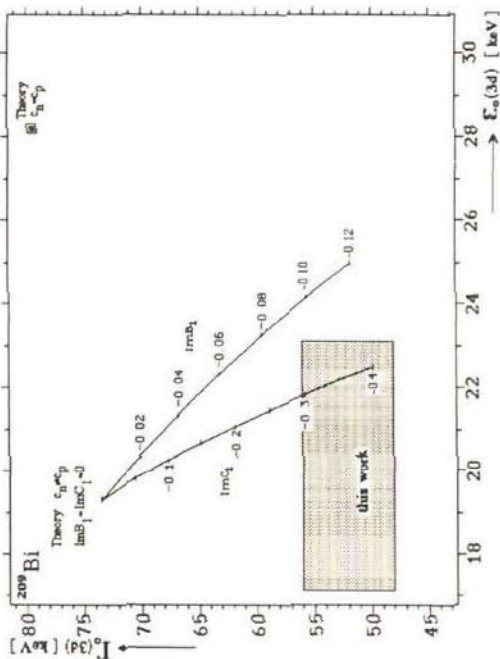
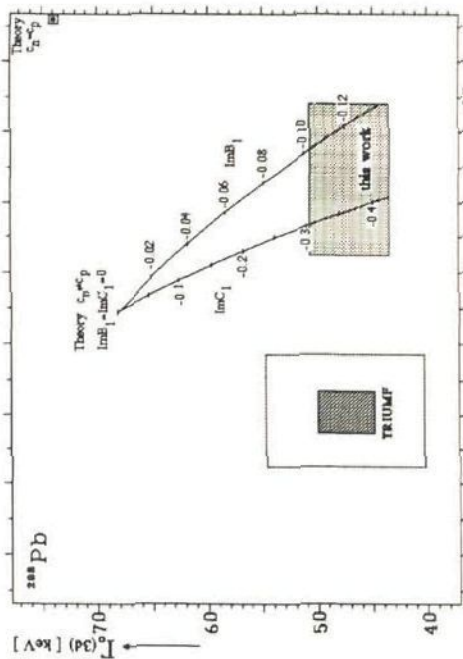
Making use of the non-zero difference in these radii, a further improvement can be reached by adding isovector absorption terms for heavier nuclei in the standard optical potentials, being the terms with the parameters B_1 and C_1 in eq. (3 - 20) and (3 - 21); both constants being imaginary if we only consider absorption by them. Kunselman et al. [Kun 83] in an attempt to determine neutron radii for nuclei with $20 \leq Z \leq 26$ already used non-zero (positive) terms of the type $\text{Im}B_1$ and $\text{Im}C_1$ in the optical potential. Their calculations did not show any improvement. Seki and Masutani [Sek 83] point out that the isovector density distribution is quite sensitive to the choice of the radial dependences of $\rho_n(r)$ and $\rho_p(r)$. The values of the isovector parameters thus varies among the different analysis and their determination requires extra care. We have tried to explain our results with additional isovector absorption terms $\text{Im}B_1$ and $\text{Im}C_1$. The result is shown in fig. 4.15 for the 3d case in of ^{208}Pb . The situation is definitely improved for negative values of both $\text{Im}B_1$ and $\text{Im}C_1$. In reality, a combination of the two might occur which results in a deviation from the $\text{Im}B_1 = \text{Im}C_1 = 0$ point which is essentially the vector sum of the deviations for each of the two quantities separately. The influence of introducing isovector terms in the calculated values for the other cases investigated is presented in fig. 4.16. In table 4.12 and 4.13 we show the results of the calculations for different values for $\text{Im}B_1$ and $\text{Im}C_1$. We also present chi-squares to compare the calculations with our experimental results. Clearly a remarkable improvement can be obtained for the 3d cases whereas the result for the 4f case in the same isotopes remains acceptable. We observe the following two main features:

- i. The improvement in the calculated values from only choosing different c_n and c_p values is clear but not impressive. Our choice of $\Delta c_{np} = 0.14$ fm is somewhat arbitrary. The change of the calculated value is to a very good approximation linear with Δc_{np} (see fig. 4.15).
- ii. The use of a non-zero isovector term $\text{Im}B_1$ or $\text{Im}C_1$ or a combination of both can bring the theory in almost complete agreement with the observed 3d data. The most overall agreement is reached with a value $\text{Im}B_1 = -0.08$ or $\text{Im}C_1 = -0.20$, or some combination of both.

In the case of the deeply bound 1s orbit in light nuclei the $\text{Im}B_1$ -term has hardly any effect as the proton and neutron distributions are there almost equal. We have also investigated accurately measured isotopes such as $^{16,18}\text{O}$, $^{40,42,44,48}\text{Ca}$, $^{46,48,50}\text{Ti}$ and $^{50,52,54}\text{Cr}$ with this potential and found that its influence is acceptable.

Fig. 4.16 (next three pages) Experimental and theoretical data on pionic atom levels studied in this thesis, in a plot of widths versus shifts. The square point gives the theoretical value for $c_n = c_p$ (using the parameter set of Batty et al. [Bat 79]) the lines the values resulting from assuming indicated non-zero values for the imaginary part of either the constant B_1 or the constant C_1 in the optical potential combined with a value $c_n - c_p = 0.14$ fm.





4.4.3 Strong interaction quadrupole shifts

A quantity much more sensitive than the monopole shift to the interplay between s- and p-waves in the π -nucleus interaction is the strong interaction quadrupole shift ϵ_2 about which very little information is available. The analysis of the observed hyperfine splitting of the pionic $5g \rightarrow 4f$ and $4f \rightarrow 3d$ transitions of strongly deformed nuclei yields the effective electric quadrupole constant, A_2^{eff} . This quantity is directly proportional to the effective spectroscopic quadrupole moment, Q^{eff} . From the difference of A_2^{eff} with the calculated electromagnetic quadrupole constant A_2 , a value is obtained for the strong interaction quadrupole shift ϵ_2 (eq. (3 - 37)). The formulae for calculating the quadrupole moment from experimental data for muonic and pionic atoms can be found in chapter 3 and ref. [Koc 80]. In table 4.14 we present in addition to our results experimental values that we collected or calculated from other experiments.

The agreement of $\epsilon_2(4f)$ with standard optical calculations, $\epsilon_2(4f)=0.0\pm 0.1$, is rather poor. The sign of both the calculated and experimental values for the strong interaction quadrupole shift ϵ_2 is different for 4f and 3d level, whereas they are all positive for the monopole shift ϵ_0 (i.e. attractive). In the case of ^{237}Np we observe, for the first time, that the sign for the experimental value of $\epsilon_2(4f)$ is opposite to that of the calculated one and to that of the other elements in the same pionic shell (see table 4.14). This effect is very similar to the change of sign of the strong interaction monopole shift ϵ_0 observed in the pionic 2p level in the region around $Z = 33$ by Abela et al. [Abe 77]. The effect of changing sign in both cases can be ascribed to the increasing importance of the repulsive s-wave part in the strong interaction when the overlap between pion and nuclear wave functions becomes larger in deeper pionic orbits (see also the anomalous Γ_0 in 3d and 1s pionic orbits). This change of sign is predicted to occur by theory for both ϵ_0 and ϵ_2 . The experimental values are, however, not reproduced correctly.

The individual contributions to the $\epsilon_2(4f)$ in ^{237}Np for the pionic 4f state are calculated to be $\epsilon_2(s) = +0.901$ keV and $\epsilon_2(p) = -0.919$ keV^{*}). As pointed out by Koch and Scheck [Koc 80] the p-wave part is less important in ϵ_2 than in ϵ_0 . Therefore, when in going to heavier nuclei the pionic 4f level is more deeply bound and the repulsive s-wave interaction will become increasingly important, a change of sign in ϵ_2 is expected before it occurs in ϵ_0 . A similar cancellation effect could also be the reason for the smaller theoretical values of $\epsilon_0(4f)$ in comparison with the experiment in ^{238}U and ^{237}Np .

*) The sign definition [Koc 80] of the strong interaction quadrupole shift ϵ_2 , $A_2^{\text{eff}} = A_2 - \epsilon_2$, yields a negative value of ϵ_2 for an attractive interaction (p-wave), opposite to the definition of the monopole shift ϵ_0 .

Table 4.14: Strong interaction quadrupole shifts for the pionic 3d and 4f levels of some heavy deformed nuclei. The theoretical values are calculated using Batty's parameter set.

Nucleus	$A_2^{eff}(\text{exp})$ keV	Re A_2^{theory} keV	ϵ_2^{exp} keV	$\epsilon_2^{\text{theory}}$ keV	Ref
Pionic 4f level					
^{165}Ho	1.389 ± 0.027	1.336	-0.053 ± 0.027	-0.020	[Ebe 74]
^{165}Ho	1.419 ± 0.009	1.336	-0.083 ± 0.009	-0.020	[Bat 81]
^{175}Lu	1.698 ± 0.029	1.609	-0.089 ± 0.029	-0.028	[Ebe 78]
^{181}Ta	1.724 ± 0.011	1.643	-0.081 ± 0.011	-0.031	[Bat 81]
^{181}Ta	1.750 ± 0.016	1.643	-0.107 ± 0.016	-0.031	[Kon 81]
^{181}Ta	1.818 ± 0.011	1.643	-0.175 ± 0.011	-0.031	This work
$^{\text{nat}}\text{Re}$	1.163 ± 0.010	1.117	-0.046 ± 0.010	-0.023	[Kon 81]
$^{\text{nat}}\text{Re}$	1.141 ± 0.010	1.117	-0.024 ± 0.010	-0.023	This work
^{209}Bi	-0.37 ± 0.05	-0.302	-0.07 ± 0.05	-0.009	[Bee 78]
^{237}Np	3.80 ± 0.08	4.295	$+0.49 \pm 0.08$	-0.018	This work
Pionic 3d level					
^{181}Ta	9.1 ± 0.5	9.610	$+0.5 \pm 0.5$	+4.55	[Kon 81]
^{181}Ta	7.67 ± 0.16	9.610	$+1.94 \pm 0.16$	+4.55	This work
$^{\text{nat}}\text{Re}$	5.4 ± 0.6	6.479	$+1.1 \pm 0.6$	+3.24	[Kon 81]
$^{\text{nat}}\text{Re}$	5.97 ± 0.19	6.479	$+0.51 \pm 0.19$	+3.24	This work

4.5 Summary

New or improved values have been found for widths and energies of strongly bound pionic atom levels. To explain the values found, the theory of these levels has been extended in two ways. On one hand, the known difference between the distributions of neutrons and protons in the nucleus has been taken into account. This gave a noticeable but far from sufficient improvement in the relation between theory and experiment. A further and almost completely satisfactory agreement could be obtained by adding some isovector absorption terms to the optical potential.

For the first time a change of sign for the strong interaction quadrupole shift $\epsilon_2(4f)$ was observed. The standard optical model calculations are in disagreement with the experimental value for $\epsilon_2(4f)$, while the strong interaction monopole parameters $\Gamma_0(4f)$ and $\epsilon_0(4f)$ agree reasonably well with these calculations.

Chapter 5

The Quadrupole Moment of $^{237}\text{Np}^\dagger$

5.1 Introduction

From the study of muonic and pionic atoms of a deformed heavy actinide, several interesting aspects can be learnt about nuclear structure, weak, electromagnetic and strong interactions and fission. Fission processes using negatively charged muons have now been studied for about 25 years. Among others, these experiments confirmed Wheeler's prediction [Whe 49], that several channels lead to such fission of heavy nuclei. The binding energy of the muon depends sensitively on the nuclear deformation and thus strongly influences the fission barrier.

A wealth of other data, bearing directly on nuclear shapes, can be obtained from the study of muon induced fission and the muonic X-ray spectra. Quantities of interest are the deformed Fermi charge distribution parameters, the spectroscopic nuclear quadrupole and hexadecapole moments of nuclear ground states, the root-mean-square (rms) radii and the transition matrix elements involving the low-lying states of the ground state rotational band. Earlier experiments, where the ratios of prompt to delayed muon induced fission have been studied [Ach 84a], demonstrated that this ratio was large in ^{237}Np in comparison to that of neighbouring heavy actinides. A study of the role of radiationless transitions in muonic ^{237}Np is therefore interesting; its result is reported in an appendix. Until now, the muonic ^{237}Np X-ray spectrum has never been investigated.

Normally, nuclear ground-state quadrupole moments are obtained from the measurement of hyperfine splitting of electronic atoms. Since the size of the electronic orbit is large compared to nuclear dimensions, the quadrupole splitting for an isolated atomic state depends on the quadrupole hyperfine splitting (hfs) constant A_2 which is a product of the spectroscopic quadrupole moment Q and the electric field gradient of the atomic electrons at the nucleus. The hfs constant can usually be measured precisely by several techniques such as atomic beam experiments, nuclear quadrupole resonance, optical spectroscopy etc. Despite the high precision inherent to these experiments, the quadrupole moments extracted from those data have generally large systematic errors. They reflect the uncertainties with which the field gradient of a multi-electron system can be calculated, which can be as large as 50% or more [Ful 69]. Muonic atoms do not have this problem since they essentially are one-particle systems. On the other hand, the

[†] This chapter has been published in a reduced form as part of a paper [Laa 87].

orbit size for low-lying levels of heavy muonic atoms (1s and 2p states) is comparable to the nuclear size. The quadrupole matrix elements then do not factorize as in the case of electronic atoms and the quadrupole splitting depends on the spatial distribution of the nuclear charge rather than on an integral property like the quadrupole moment. Moreover, for heavy deformed nuclei the energy of the first excited state(s) is (are) of the same order of magnitude as the 2p or 3d fine structure (fs) splitting, giving rise to dynamic nuclear excitations. Yet, in each exotic atom (muonic or pionic) a domain exists of energy states whose orbit size is large compared to the nuclear dimensions and yet small compared to the orbits of the atomic electrons. In this intermediate domain, the exotic atom is 'hydrogen-like'. The data in this domain can be analyzed in a nuclear model independent fashion and then produce a precise value for the spectroscopic quadrupole moment. For deformed nuclei it is then possible (e.g. by relating Q to B(E2) as obtained from Coulomb excitation experiments) to test the predictions of the rotational model concerning the diagonal and off diagonal E2 matrix elements.

In this chapter we report on a measurement on of the hyperfine splitting of the 5g→4f complexes in muonic ^{237}Np , where uncertainties in the calculation of multi-electron systems and estimating the electric field inhomogeneity at the nucleus as well as the effect of the polarization of the electron core do not contribute.

5.2 Muonic X-rays and nuclear structure effects

The dominant hf splitting is due to the nuclear quadrupole effect, but we also include a small magnetic dipole splitting in our analysis. The shift of each member away from the central value of the hf multiplet can then be written as

$$\Delta E_{\text{hfs}} = A_1^{(n,I,j)} \gamma(I,j,F) + A_2^{(n,j)} C(I,j,F) \quad (5-1)$$

where $I, j, F = I + j$ are the nuclear, atomic and total spins and n is the atomic orbit number and

$$\gamma(I,j,F) = F(F+1) - I(I+1) - j(j+1) \quad (5-2)$$

and

$$C(I,j,F) = \frac{3\gamma(\gamma+1) - 4I(I+1)j(j+1)}{2I(2I-1)j(2j-1)} \quad (5-3)$$

(compare with eq. 3.30 and 3.31 for the pionic case)

The magnetic hyperfine structure constant $A_1^{(n,l,j)}$ is proportional to the nuclear magnetic moment μ_I . For a point nucleus we have [Dey 75, Dey 79]

$$A_1^{\text{point}} = \frac{\mu_I}{I} \alpha^4 Z^3 \frac{m_\mu^2}{2m_p} \frac{1}{n^3 j(j+1)(2l+1)} \quad (5-4)$$

The constant $A_2^{(n,j)}$ in formula (5-1) is the quadrupole hyperfine structure constant, which for a point-like nucleus can be written as:

$$A_2^{(\text{point})} = e^2 Q \frac{j}{2j+3} \frac{\kappa^3}{s(s+1)(2s+1)} \quad (5-5)$$

with

$$\kappa = \bar{m}_\mu \frac{Z\alpha}{\sqrt{(n-j+s)^2 + (Z\alpha)^2}} \quad (5-6)$$

where \bar{m}_μ is the reduced mass of the muon and

$$s = -\frac{1}{2} + \sqrt{\left(j + \frac{1}{2}\right)^2 - (Z\alpha)^2} \quad (5-7)$$

The ratios for the spectroscopic (Q) and the intrinsic (Q_0) quadrupole moments are related in the framework of the rotational model by

$$\frac{Q}{Q_0} = \frac{3K^2 - I(I+1)}{(I+1)(2I+3)} \quad (5-8)$$

which is the expectation value of $P_2(\cos\theta)$ in the substate $m = I$ and reflects the averaging of the charge eccentricity associated with the rotational motion. The K in this formula represents the projection of the nuclear spin on the long symmetry axis of the nucleus. Thus, $|Q|$ is always smaller than $|Q_0|$; for the particular case of $I = K$, which usually applies to the ground state, one obtains

$$Q = \frac{I(2I-1)}{(I+1)(2I+3)} Q_0 \quad (5-9)$$

The intrinsic quadrupole moment Q_0 is related to the deformation of the nucleus by the following relations [Ack 66, Kon 87]

$$Q_0 = \sqrt{\frac{16\pi}{5}} N_{\text{def}} \beta c^5 \left\{ 1 + 2\left(\frac{\pi a}{c}\right)^2 + \frac{2}{7} \sqrt{\frac{5}{11}} \beta \left[1 + \left(\frac{\pi a}{c}\right)^2 \right] + \frac{\beta^2}{2\pi} \left[3 + \left(\frac{\pi a}{c}\right)^2 \right] \right\} \quad (5-10)$$

where β is the nucleus deformation parameter,

$$N_{\text{def}} = \frac{3Z}{4\pi c^3} \left[1 + \frac{3\beta^2}{4\pi} + \left(\frac{\pi a}{c} \right)^2 \right]^{-1} \quad (5-11)$$

The nuclear charge distribution is taken to be characterized by the average radius c and the surface thickness t which is connected to the parameter a above by $a = ct / 4\pi \ln 3$.

5.3 Experimental details and results

The experiment was performed at PSI (formerly SIN), Switzerland. The muon beam was tuned to a momentum of 50 MeV/c. Approximately $10^5 \mu^-/s$ were stopped in a 0.92 g/cm^2 thick NpO_2 target[†], containing 9.981 g of ^{237}Np . The experimental set-up and measuring technique, which include one BGO Compton suppression spectrometer, have been described in chapter 2. The energy calibration was taken from muonic X rays and energies of accurately known nuclear γ -transitions induced in the target and its aluminum encapsulation by the incident particle beam. The neutron induced background transitions were well separated in time from the prompt X-rays, by using a time-of-flight path of about 60 cm between target and the detector. The line shape of the detector as a function of energy and the linearity of the ADC's were calibrated with sources such as ^{152}Eu , ^{137}Cs and ^{60}Co .

The muonic $2p \rightarrow 1s$, $3d \rightarrow 2p$ and $4f \rightarrow 3d$ complexes are somewhat complicated for our purpose since several states belonging to the rotational band of the Nilsson ground state configuration $5/2^+[642]\uparrow$ in ^{237}Np are mixed appreciably with the muonic $3d$, $2p$ and $1s$ states. We therefore derived the spectroscopic nuclear quadrupole moment by fitting the observed hyperfine splitting in both the muonic $6g \rightarrow 4f$ and $5g \rightarrow 4f$ complexes, which have transition energies in the region of about 0.86 and 0.55 MeV, respectively. The K, L and M X-ray data were used to determine nuclear charge Fermi distribution parameters, which came out to be $c = 7.00 \pm 0.02 \text{ fm}$ and $t = 2.3 \pm 0.1 \text{ fm}$, respectively.

In fig. 5.1, we present the hyperfine splitting of the $5g^{9/2} \rightarrow 4f^{7/2}$ and $5g^{7/2} \rightarrow 4f^{5/2}$ muonic X-rays, which are rather more intense than the $6g \rightarrow 4f$ complexes. The energies of the main E1 transitions in the $4f^{5/2} \rightarrow 3d^{3/2}$, $4f^{7/2} \rightarrow 3d^{5/2}$, $6g^{7/2} \rightarrow 4f^{5/2}$, $6g^{9/2} \rightarrow 4f^{7/2}$, $5g^{7/2} \rightarrow 4f^{5/2}$ and $5g^{9/2} \rightarrow 4f^{7/2}$, listed in table 5.1, have been obtained by fitting the various muon complexes using the program FIT, described in chapter 2. The results have been evaluated using the Los Alamos

[†] We gratefully acknowledge the production and preparation of the ^{237}Np target by the European Institute for Transuranium Elements, JRC Karlsruhe, W.Germany.

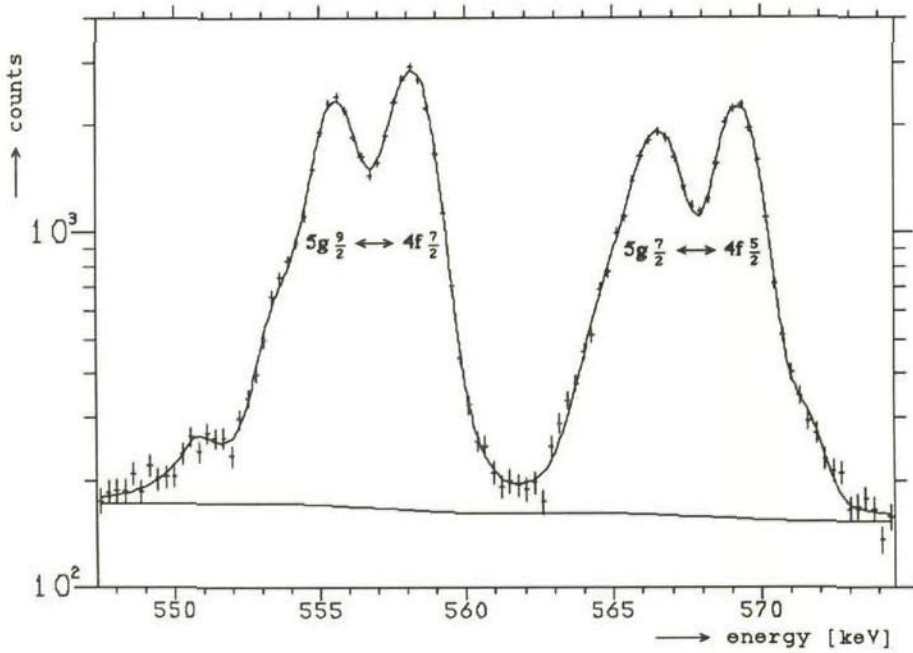


Fig. 5.1 The muonic $5g \rightarrow 4f$ hyperfine complexes of ^{237}Np . The hyperfine splitting in each of the two complexes is pronounced. The solid line is the fit to the experimental data of the hyperfine complex, including some weak background nuclear γ -ray transitions produced in ^{236}U and ^{237}U .

National Laboratory computer codes MUON2 and XRAY2, written by Y. Tanaka. The computer code MUON2 is a program for muonic atoms, where muonic level energies are calculated, corrected for vacuum polarization effects, self energy effect, electron screening and relativistic recoil. The program also provides for hyperfine splitting energies, nuclear polarization energies and relative intensities of E1 cascade transitions between the muon-nuclear coupled states. XRAY2 is a computer program which gives the best-fit charge parameters by fitting experimental muonic X-ray energies, using routines from the computer code MINUIT.

A moderately accurate value of $Q = 3.86 \pm 0.06$ b can be obtained from the measured energy splitting of 2.83 ± 0.06 keV and 3.25 ± 0.07 keV for the $6g^{9/2} \rightarrow 4f^{7/2}$ and $6g^{7/2} \rightarrow 4f^{5/2}$ muonic X-ray complexes, respectively. The energy splitting for the two main components of the $5g^{9/2} \rightarrow 4f^{7/2}$ and $5g^{7/2} \rightarrow 4f^{5/2}$ muonic X-ray transitions are 2.608 ± 0.019 keV and 2.863 ± 0.021 keV for the two different complexes, respectively. From these values, a spectroscopic nuclear quadrupole moment $Q = 3.886 \pm 0.006$ b is derived for the ground state

of ^{237}Np . The energy distance between the main two peaks of the two $5g^{9/2} \rightarrow 4f^{7/2}$ and $5g^{7/2} \rightarrow 4f^{5/2}$ muonic X-ray complexes is 10.864 ± 0.019 keV.

Table 5.1: Energies of the main transitions in the muonic $4f \rightarrow 3d$, $6g \rightarrow 4f$ and $5g \rightarrow 4f$ hyperfine split X-ray complexes

X-ray complex	Energy keV	transition $F_{\text{initial}} \rightarrow F_{\text{final}}$
$4f^{5/2} \rightarrow 3d^{3/2}$	1282.06 ± 0.06	$4^- \rightarrow 3^+$
	1269.96 ± 0.06	$5^- \rightarrow 4^+$
$4f^{7/2} \rightarrow 3d^{5/2}$	1221.32 ± 0.04	$5^- \rightarrow 4^+$
	1217.59 ± 0.05	$6^- \rightarrow 5^+$
$6g^{7/2} \rightarrow 4f^{5/2}$	870.23 ± 0.10	$5^+ \rightarrow 4^-$
	866.98 ± 0.07	$6^+ \rightarrow 5^-$
$6g^{9/2} \rightarrow 4f^{7/2}$	857.23 ± 0.08	$6^+ \rightarrow 5^-$
	854.40 ± 0.06	$7^+ \rightarrow 6^-$
$5g^{7/2} \rightarrow 4f^{5/2}$	569.12 ± 0.02	$5^+ \rightarrow 4^-$
	566.26 ± 0.02	$6^+ \rightarrow 5^-$
$5g^{9/2} \rightarrow 4f^{7/2}$	558.00 ± 0.02	$6^+ \rightarrow 5^-$
	555.39 ± 0.02	$7^+ \rightarrow 6^-$

5.4 Discussion

The present experimental result, $Q = 3.886 \pm 0.006$ b, is an improvement in accuracy of more than an order of magnitude for the value of the spectroscopic nuclear quadrupole moment. Earlier measurements not involving muonic data are the following. Veyssi re et al. [Vey 73] have obtained a value $Q = 4.0 \pm 0.4$ b by analyzing the splitting of the giant dipole resonance peak. From the $B(E2)$ value derived from the Coulomb excitation [New 58] of the 33.195 keV rotational level, but using a value 188 for the conversion coefficient (see Ellis [Ell 78]), one obtains $Q = 3.7 \pm 0.8$ b. Interesting is the following comparison with data derived from muonic ^{241}Am , following a method first suggested by Dunlap and Kalvius [Dun 69] who combined measurements from M ssbauer-effect, optical spectroscopy and Coulomb excitation data. They notice that the

ground state of ^{241}Am and the 59.537 keV excited state of ^{237}Np have the same Nilsson quantum numbers $5/2^- [523] \downarrow$, and therefore the same quadrupole moment, except for a small correction due to a change in nuclear deformation and a size correction proportional to $A^{2/3}$. Nuclear γ -ray resonance measurements [Dun 68, Sto 67] yield a value 0.99 ± 0.02 for the ratio of the quadrupole moment of the 59.537 keV excited state to that of the ground state. Dunlap and Kalvius combined these data with a value $Q = 4.9$ b [Man 56] for the ^{241}Am quadrupole moment and thus arrived at a value $Q = 4.1 \pm 0.7$ b for the ^{237}Np ground state. Using the new value 4.34 ± 0.05 b for ^{241}Am , derived from muonic ^{241}Am [Joh 85], one finds $Q = 3.9 \pm 0.2$ b, which agrees excellently with the present value given above.

Reversely, new $B(E2) \downarrow$ -values from the first and the second excited states could be derived from the transition energies of the muonic $4f \rightarrow 3d$, $6g \rightarrow 4f$ and $5g \rightarrow 4f$ transitions (see table 5.1). The results, 3.17 ± 0.08 e^2b^2 and 2.77 ± 0.10 e^2b^2 respectively, confirm and improve the old Coulomb excitation results [New 58], 3.1 ± 0.8 and $2.4 \pm e^2b^2$. The $B(E2) \downarrow$ -value from the second to the first excited state was deduced as 0.23 ± 0.04 e^2b^2 and the quadrupole moment of the first excited state as $Q(7/2^+) = 2.55 \pm 0.12$ b.

References

- Abe 77 R. Abela et al.; Zeit. für Physik **A282** (1977) 93
- Ach 84a J.F.M. d'Achard van Enscht et al.; SIN Newsletter **16** (1984) 67
- Ach 84b J.F.M. d'Achard van Enscht et al.; Physics Letters **136B** (1984) 24
- Ach 85 J.F.M. d'Achard van Enscht; Nucl. Instr. and Meth. **A238** (1985) 98
- Ack 66 H.L. Acker; Nuclear Physics **87** (1966) 153
- Ang 80 I. Angeli et al.; J. of Phys. **G6** (1980) 303
- Ant 83 Yu. Antipov et al; Physics Letters **121B** (1983) 445
- Bac 70 G. Backenstoss; Ann. Rev. Nucl. Sci **20** (1970) 467
- Bar 73 R.C. Barrett et al.; Physics Letters **47B** (1973) 297
- Bat 76 C.J. Batty et al.; Nucl. Instr. and Meth. **137** (1976) 179
- Bat 79 C.J. Batty et al.; Nuclear Physics **A322** (1979) 445
- Bat 81 C.J. Batty et al.; Nuclear Physics **A355** (1981) 383
- Bat 83 C.J. Batty et al.; Nuclear Physics **A402** (1983) 411
- Bee 78 R. Beetz et al.; Zeit. für Physik **A286** (1978) 215
- Bev 69 P.R. Bevington; Data reduction and error analysis for the Physical Sciences.(Mc Graw-Hill, New York, 1969)
- Bir 83 B.L. Birbrair et al.; J. Phys. G: Nuclear Physics **9** (1983) 1473
- Bir 85 B.L. Birbrair et al.; J. Phys. G: Nuclear Physics **11** (1985) 471
- Bla 67 J.M. Blatt; J. of Computational Physics **1** (1967) 382
- Blo 72 J. Blomqvist, Nuclear Physics **B48** (1972) 95
- Dav 87 P. David et al.; Sin newsletter **19** (1987) 60
- Dey 75 W. Dey; Messung von spektroskopischen kerngrundzustandsquadrupolmomenten mit myonischen atomen am beispiel von ^{175}Lu , thesis ETH-Zürich (1975) 30
- Dey 79 W. Dey et al.; Nuclear Physics **A326** (1979) 418
- Dun 68 B.D.Dunlap et al.; Physical Review **171** (1968) 316
- Dun 69 B.D.Dunlap and G.M.Kalvius; Physical Review **186** (1969) 1296
- Ebe 74 P. Ebersold et al.; Physics Letters **53B** (1974) 48
- Ebe 78 P. Ebersold et al.; Nuclear Physics **A296** (1978) 493
- Ell 78 Y.A.Ellis; Nuclear Data Sheets **23** (1978) 71
- Eng 74 R. Engfer et all.; At. Nucl. Data Tables **14** (1974) 409
- Eri 66 M. Ericson and T.E.O. Ericson; Ann. of Phys. **36** (1966) 323
- Eri 67 T.E.O. Ericson; Proc. Int. School of Physics 'Enrico Fermi' course XXXVIII, Ac. Press. New York 1967, p 253

- Eri 82 T.E.O. Ericson and L. Tauscher; Physics Letters **112B** (1982) 425
- Fri 69 B. Fricke; Z. Physik **218** (1969) 495
- Fri 73 B. Fricke; Phys. Rev. Lett. **30** (1973) 119
- Fri 75 J.L. Friar and J.W. Negele; Physics Letters **46B** (1975) 5
- Fri 80 E. Friedman and A. Gal; Nuclear Physics **A345** (1980) 457
- Ful 69 G.H. Fuller and V.W. Cohen; Nucl. Data Tables **A5** (1969) 433
- Gau 69 W. Gautschi; S.I.A.M. J. Numer. Anal. **12** (1969) 465
- Har 86 Harshaw Scintillation Detectors and Nuclear Systems, folder (1986)
- Hof 80 G.W. Hoffman et al.; Physical Review **C21** (1980) 1488
- Iac 71 F. Iachello and A Landé; Physics Letters **35B** (1971) 205
- Jec 86 B. Jeckelmann et al.; Phys. Rev. Lett. **56** (1986) 1444
- Joh 85 M.W. Johnson et al.; Physics Letters **161B** (1985) 75
- Kas 82 J. Kasagi et al.; Nucl. Instr. & Meth. in Phys. Res. **A193** (1982) 557
- Kis 55 L. Kisslinger; Phys. Rev. **98** (1955) 761
- Koc 73 J.H. Koch and M.M. Sternheim; Los Alamos Scientific Laboratory, report LA-5110, (1973)
- Koc 80 J.H. Koch and F. Scheck; Nuclear Physics **A340** (1980) 221
- Kol 69 D.S. Koltun; Advances in Nuclear Physics, **3** (1969) 71
- Kon 79 J. Konijn et al.; Nuclear Physics **A326** (1979) 401
- Kon 81 J. Konijn et al.; Nuclear Physics **A360** (1981) 187
- Kon 87 J. Konijn, private communications
- Kre 69 M. Krell and T.E.O. Ericson; Nuclear Physics **B11** (1969) 521
- Kun 83 R. Kunselman et al.; Nuclear Physics **A405** (1983) 627
- Laa 85 C.T.A.M. de Laat et al.; Physics Letters **162B** (1985) 81
- Laa 87 C.T.A.M. de Laat et al.; Physics Letters **189B** (1987) 7
- Laa 88 C.T.A.M. de Laat; NIKHEF-K, "fit manual", internal report, in preparation
- Man 56 T.E. Manning et al.; Physical Review **102** (1956) 1108
- Mar 63 D.W. Marquardt; J. Soc. Ind. Appl. Math. **11- 2** (1963) 431
- Mat 80 N. Matsushita et al.; Michigan State University, internal report MSUCL-305 and MSUNC-207 (1980)
- Men 84 L.I. Men'shikov and L.I. Ponomarev; Pis'ma Zh. Eksp. Teor. Fiz. **39, no 12** (1984) 542
- Nag 76 M.M. Nagels et al.; Nuclear Physics **B109** (1976) 1
- Neg 72 J.W. Negele and D. Vautherin.; Physical Review **C5** (1972) 1472
- New 58 J.O. Newton ; Nuclear Physics **5** (1958) 218
- Oli 78 A. Olin et al.; Nuclear Physics **A312** (1978) 361

- Oli 85 A. Olin et al.; Nuclear Physics **A439** (1985) 589
- Oli 84 J.G.J. Olivier et al., Nuclear Physics **A429** (1984) 477
- Par 67 A. Partensky and M. Ericson; Nuclear Physics **B1** (1967) 382
- Rou 69 J.T. Routti and S.G. Prussin; Nucl. Instr. and Meth. **72** (1969) 125
- Sak 67 J.J. Sakurai, Advanced Quantum Mechanics. Addison-Wesley Publishing Company, Reading, Massachusetts, 1967
- Sch 72 F. Scheck, Nuclear Physics **B42** (1972) 573
- Sch 83 F. Scheck, Leptons, Hadrons and Nuclei. North-Holland Publishing Company, Amsterdam, 1983
- Seg 78 S.L. Segel; Phys. Rev. **C18** (1978) 2430
- Sek 82 R. Seki; Physical Review **C26** (1982) 1342
- Sek 83 R. Seki and K. Masutani; Physical Review **C27** (1983) 2799
- Sem 68 G.K. Semin and E.V. Bryukhova; Sov. J. Nucl. Phys. **7** (1968) 797
- Sto 67 J.A. Stone and W.L. Phillinger; Symp. Faraday Soc. **1** (1967) 77
- Taa 85 A. Taal et al.; Physics Letters **156B** (1985) 296
- Tan 84 Y. Tanaka et al.; Physics Letters **143B** (1984) 347
- Tau 71 L. Tauscher; Proc. Int. Sem. " π -Meson Nucleus Interaction" Strasbourg 1971 CNRS-Strasbourg p. 45
- Tau 78 L. Tauscher et al.; Zeit. für Physik **A285** (1978) 139
- Tau 84 L. Tauscher et al.; Nuclear Physics **A415** (1984) 333
- Vey 73 A. Veysseyère et al.; Nuclear Physics **A199** (1973) 45
- Vog 74 P. Vogel; Atom. Nucl. Data tables **14** (1974) 599
- Vri 87 H. de Vries et al.; Atomic Data and Nuclear Data Tables **36** (1987) 495
- Whe 49 J.A. Wheeler; Rev. Mod. Phys. **21** (1949) 133
- Win 63 R. Winston; Physical Review **129** (1963) 2766
- Wri 87 D.H. Wright et al.; Physical Review **C35** (1987) 2258
also reported on at the Int.Conf. PANIC 1987, April 1987 in Kyoto, Japan

(This appendix has been reproduced from Physics Letters **180B** (1986) 324-328 North-Holland, Amsterdam.)

Appendix A

In the course of our work on ^{238}Np we also obtained results on the radiationless transitions in muonic Neptunium. These results are essential to get a complete picture for the prompt muon induced fission process in Neptunium. The results of this investigation were published in a letter reproduced below.

**THE PROBABILITY OF NON-RADIATIVE DECAY
OF THE 3d LEVEL IN MUONIC ^{237}Np**

P. DAVID, J. HARTFIEL¹, H. JANSZEN², T. MAYER-KUCKUK, R. VON MUTIUS³

Institut für Strahlen- und Kernphysik der Universität Bonn, D-5300 Bonn, Fed. Rep. Germany

C.T.A.M. DE LAAT, A. TAAL, W. DUINKER, J. KONIJN

NIKHEF-K, NL-1009 DB Amsterdam, The Netherlands

J.F.M. D'ACHARD VAN ENSCHUT⁴

Physics Department, Delft University of Technology, NL-2629 JB Delft, The Netherlands

C. GUGLER, L.A. SCHALLER, L. SCHELLENBERG

Institut de Physique, Université de Fribourg, CH-1700 Fribourg, Switzerland

T. KROGULSKI

University of Warsaw, Branch in Białystok, 15-424 Białystok, Poland

C. PETITJEAN, H.W. REIST

SIN, CH-5234 Villigen, Switzerland

and

W. MÜLLER

European Institute for Transuranium Elements, JRC Karlsruhe, Fed. Rep. Germany

Received 27 June 1986

The X-ray spectrum of muonic ^{237}Np has been investigated with stopped muons in a NpO_2 target, containing about 10 g of ^{237}Np . The probability of the radiationless muonic $3d \rightarrow 1s$ transition in ^{237}Np , $(9 \pm 4)\%$, was obtained by comparing the relative intensities of the main muonic X-ray transitions in singles and coincidence spectra. The coincidences were gated by the $2p \rightarrow 1s$ transitions.

The role of quadrupole $3d \rightarrow 1s$ radiationless transitions in nuclear excitation, leading to prompt processes like γ decay, neutron emission or fission [1-4],

has been discussed in several papers [5-8].

There are two theoretical descriptions of the non-radiative width of the 3d level in heavy muonic atoms. A microscopical one [5] emphasizes the role of the compound nucleus mechanism, and a phenomenological one [8] describes it in terms of the isoscalar giant quadrupole resonance as an entrance channel for nuclear excitation accompanied by the radiationless $3d \rightarrow 1s$ transition.

If the phenomenological approach is correct, the probability of the radiationless $3d \rightarrow 1s$ transition,

¹ Present address: Bopp und Reuther, D-6800 Mannheim, Fed. Rep. Germany

² Present address: Physikalisch-Technische Bundesanstalt, D-3300 Braunschweig, Fed. Rep. Germany.

³ Present address: Rheinmetall GmbH, D-4000 Düsseldorf, Fed. Rep. Germany.

⁴ Present address: Philips I & E Laboratories, Eindhoven, The Netherlands.

calculated by Teller and Weiss [8] for muonic ^{238}U to be about 15%, should be quite similar for muonic atoms of neighbouring nuclei such as ^{232}Th , ^{235}U or ^{237}Np . For ^{238}U this probability is found [5] to agree with the prediction [8]. However, so far no other experimental data are available. To provide such data was one of the motivations to perform the present experiment.

Experimentally there is a systematic and rapid increase in the probability of prompt fission with the value of the fissility parameter [1,3]. Regarding prompt fission of muonic ^{238}U , about 75% of all events are due to the $3d \rightarrow 1s$ radiationless transition [7]. The question then arises how the yield of prompt fission is shared between the $3d \rightarrow 1s$ and the $2p \rightarrow 1s$ radiationless transitions in muonic ^{237}Np , where the total prompt fission rate per stopped μ^- is about 10 times higher than the corresponding figure for ^{238}U . In order to clarify these points, we performed a measurement on ^{237}Np to determine the probability of the radiationless muonic $3d \rightarrow 1s$ transition, using the same experimental method as was used to determine the non-radiative decay of the $3d$ level in muonic ^{238}U [6,7].

From a comparison of X-ray singles spectra with coincidence spectra, in which the coincidence rate between the $2p \rightarrow 1s$ transition and other cascade lines is measured, the fraction of missing $3d \rightarrow 2p$ muonic X-rays is obtained, giving the total decay probability of the $3d$ level not populating the $2p$ level. Correcting this value for the radiative width of the $3d \rightarrow 1s$ transition and disregarding the very weak ($\leq 0.1\%$) $3d \rightarrow 2s$ transition, one obtains the non-radiative width of the $3d$ level.

The experiment was performed at the SiN cyclotron with a beam of negative muons, having a momentum of 85 MeV/c. The beam intensity, measured as the number of coincidences between the first two counters of the beam telescope, was about $7 \times 10^5 \mu^-/\text{s}$. The muons were slowed down to stop in the ^{237}Np target by using a beryllium/polyethylene degrader. The target consisted of NpO_2 , containing 9.981 g of ^{237}Np , with a thickness of about 0.92 g/cm². To avoid pile-up, events in which two muons arrived within a time interval of 200 ns of each other were rejected.

The previous measurement [6] on ^{238}U has shown the necessity to take care of the unfavourable inten-

sities of the weak $5 \rightarrow 4$ and $4 \rightarrow 3$ transitions and of the components in the $2p \rightarrow 1s$ complex as compared to the high Compton background. To match this problem the muonic ^{237}Np X-ray spectra were registered in a large volume (28%) intrinsic Ge detector, provided with a BGO-shield (13 cm \times 13 cm \times 15 cm) for Compton suppression. The suppression factor for the Compton background in the measurement was about five. The maximum energy registered (in 8192 channels) by the Ge counter, was about 10 MeV. Two large-volume scintillation counters, a CsF and a NaI(Tl) crystal, were used to record the $2p \rightarrow 1s$ transition in the muonic ^{237}Np cascade. In the off-line analysis these detectors were set to gate an energy interval from 4 to 8 MeV, which includes the $2p \rightarrow 1s$ transitions. The muonic ^{237}Np spectra were registered in both singles mode and in coincidence with the CsF and/or NaI(Tl) counters. All three detectors were mounted around the target at 90° with respect to the μ -beam direction. The data acquisition system is described in ref. [9].

In figs. 1–3 selected parts of the muonic ^{237}Np X-ray spectrum are presented. In the coincidence spectra of the Ge counter we observed a small amount of the $2p \rightarrow 1s$ transitions, due to accidental coincidences with the counting rate in the scintillation crystals. The observed yield of the $2p \rightarrow 1s$ transition corresponds to an admixture of the singles spectrum into the coincident spectrum of about 10–15%. After applying a correction for this effect the ratio of the gated to the non-gated L X-ray complexes are normalized to unity, using the summed contents of the main components of these transitions in the two energy intervals 3070–3095 keV and 3280–3360 keV (fig. 1). This correction on the coincidence spectrum gives an uncertainty in the final result that is negligible in comparison to the quoted accuracies. The above energy intervals, chosen for the summed components of the L X-rays, are selected to minimize the influence of the background and possible systematic errors. A change of less than 0.3% occurs in the normalization, when choosing the energy interval to be 2950–3410 keV.

In fig. 2, superimposed on each other, the gated and non-gated spectra of the $4f \rightarrow 3d$ transitions are shown and normalized as just discussed (this normalization value, obtained from the ratio of the total sum of the L X-ray complex in the singles to that of the

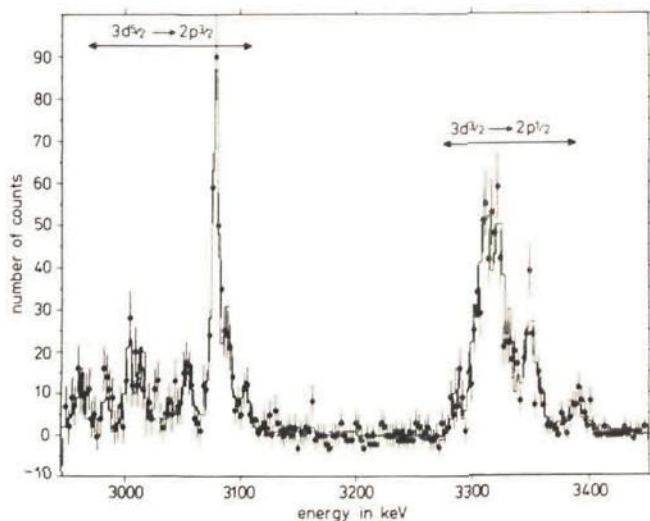


Fig. 1. The muonic ^{237}Np $3d \rightarrow 2p$ transition measured in coincidence with the $2p \rightarrow 1s$ transition. The solid line (histogram) represents the singles spectrum normalized to the coincidence data. The background has been subtracted. The left-hand side muonic complex represents the $3d_{5/2} \rightarrow 2p_{3/2}$ hyperfine complex and the right-hand side complex represents the $3d_{3/2} \rightarrow 2p_{1/2}$ hyperfine complex.

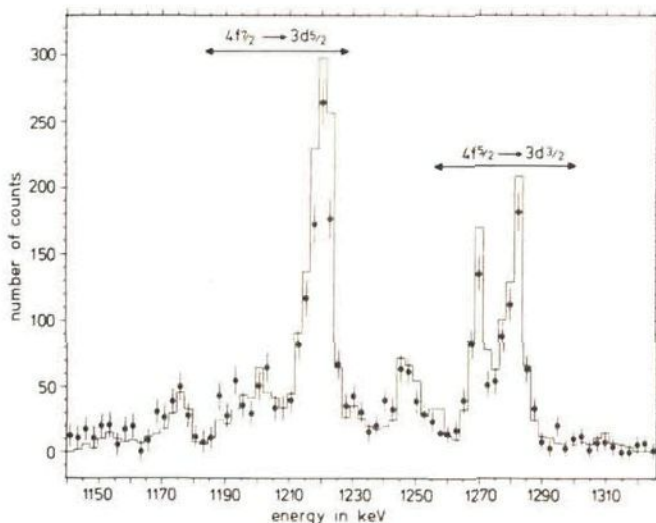


Fig. 2. The muonic ^{237}Np $4f \rightarrow 3d$ transition measured in coincidence with the $2p \rightarrow 1s$ transition. The singles spectrum (solid line histogram) was normalized to the coincidence data by multiplying the content of the original spectrum with the normalization factor, obtained from the ratio of gated to non-gated spectra of the $3d \rightarrow 2p$ transition. The background has been subtracted (see text). The left-hand side muonic complex represents $4f_{7/2} \rightarrow 3d_{5/2}$ hyperfine complex and the right-hand side complex represents the $4f_{5/2} \rightarrow 3d_{3/2}$ hyperfine complex.

coincidence spectrum, was used for all the other complexes). In a similar way, fig. 3 presents both spectra for the $5g \rightarrow 4f$ transitions. The background for the different X-ray transitions has been defined by a step-function as described e.g. by Taal et al. [10]. However, the data have also been analysed with a linearly decreasing background. The difference in the results for the two cases was within the quoted errors.

The suppression of the $4f \rightarrow 3d$ and $5g \rightarrow 4f$ transitions in the muonic ^{237}Np X-ray cascade, when measured in coincidence with the $2p \rightarrow 1s$ transition, is clearly observed. For the separate L X-ray components in ^{237}Np the differences in yield between singles and coincidence spectra are negligibly small within the limits of the errors (fig. 1), whereas they were significantly different in the case of ^{238}U [6]. Because of the high background of the natural γ -ray activity of ^{237}Np , the $6 \rightarrow 5$ transition was obscured and could not be used for the analysis.

Based on the $4f \rightarrow 3d$ and $5g \rightarrow 4f$ results, the $2p$ level is bypassed by $(13 \pm 5)\%$ and $(10 \pm 6)\%$, respectively, or on the average by $(12 \pm 4)\%$. The quoted errors include inaccuracies due to background estimation.

The radiative, relative width of the $3d$ level in muonic ^{237}Np , is obtained from a comparison of the singles X-ray spectra of ^{237}Np and ^{208}Pb , resulting in a value of $(3 \pm 1)\%$ [14] and in good agreement with the calculated value for muonic ^{238}U [6]. As a consequence, the observed suppression of the $4f \rightarrow 3d$ transition in the coincidence spectrum corresponds to a probability of $(9 \pm 4)\%$ for a radiationless $3d \rightarrow 1s$ transition in muonic ^{237}Np .

Due to the rather large relative errors in both measurements, the smaller value of the radiationless $3d \rightarrow 1s$ transition in muonic ^{237}Np as compared to ^{238}U , where it was found to be $(14 \pm 5)\%$ [6], might not be statistically significant. These results show that the phenomenological model predictions [8] are quite good.

As the muonic $2p \rightarrow 1s$ transition energies are almost the same in these nuclei, the reason for the difference in the ratios of prompt to delayed muon induced fission yield, namely $(28.3 \pm 0.3)\%$ and $(8.8 \pm 0.3)\%$ [11-14] for ^{237}Np and ^{238}U , respectively, must be explained by the difference in height of fission barriers: $E_b(^{237}\text{Np}) = 5.50$ MeV and $E_b(^{238}\text{U}) = 6.35$ MeV [11-13]. In the case of ^{237}Np ,

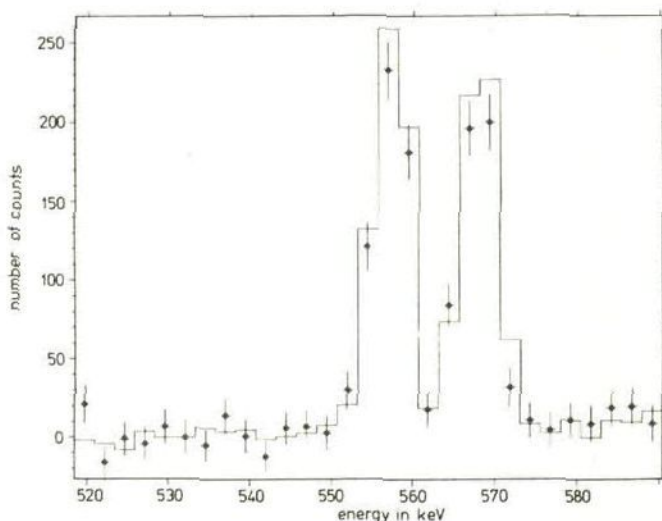


Fig. 3. The $5g \rightarrow 4f$ transition in muonic ^{237}Np , treated as mentioned in the caption of fig. 2. The left-hand side muonic complex represents the $5g_{7/2}^2 \rightarrow 4f_{7/2}^2$ hyperfine complex and the right-hand side complex represents the $5g_{5/2}^2 \rightarrow 4f_{5/2}^2$ hyperfine complex.

(22.0 ± 0.2)% of all fission can be ascribed to prompt fission, resulting in a prompt fission probability of (2.7 ± 0.3)% for ^{237}Np , when using a value of (12.4 ± 1.0)% for the amount of total fission per μ -stop [3]. Assuming most of the radiationless $3d \rightarrow 1s$ transition probability to give rise to prompt neutron events, as in the case in ^{238}U [7], one may conclude that the radiationless $2p \rightarrow 1s$ transition plays a much more important role for prompt fission in ^{237}Np than is in the case in ^{238}U . This has, however, to be verified in a separate fission-X-ray coincidence experiment.

We thank Professor Dr. J.P. Blaser and his staff for the encouraging support and for the excellent working conditions at SIN. This work is part of the research programme of, and made financially possible by, the following institutes and financially supporting organizations: Bundesministerium für Forschung und Technologie der Bundesrepublik Deutschland, Technische Hogeschool Delft, Foundation for Fundamental Research on Matter (FOM) and the Netherlands' Organization for the Advancement of Pure Research (ZWO), Swiss National Foundation and the University of Warsaw. For preparing the target we thank Mr. K. Richter and his coworkers at the European Institute for Transuranium, K.F.Z. Karlsruhe, W. Germany.

References

- [1] J.A. Diaz, S.N. Kaplan and R.V. Pyle, Nucl. Phys. 40 (1963) 54.
- [2] D. Chultem, V. Cojocaru, Dz. Ganzorig, Kim Si Chwan, T. Krogulski, V.D. Kuznetsov, H.G. Ortlepp, S.M. Polikanov, B.M. Sabirov, U. Schmidt and W. Wagner, Nucl. Phys. A 247 (1975) 452.
- [3] B.M. Aleksandrov, G.V. Buklanov, W.D. Fromm, Dz. Ganzorig, A.S. Krivokhatski, T. Krogulski, S.M. Polikanov and B.M. Sabirov, Phys. Lett. B 57 (1975) 238.
- [4] C.K. Hargrove, E.P. Hincks, G.R. Mason, R.J. McKee, D. Kessler and S. Ricci, Phys. Rev. Lett. 23 (1969) 215.
- [5] K.P. Lohs, G.W. Wolschin and J. Hüfner, Nucl. Phys. A 236 (1974) 457.
- [6] T. Johansson, J. Konijn, T. Krogulski, S. Polikanov, H.W. Reist and G. Tibell, Phys. Lett. B 116 (1982) 402.
- [7] T. Johansson, J. Konijn, T. Krogulski, S. Polikanov, H.W. Reist and G. Tibell, Phys. Lett. B 97 (1980) 29.
- [8] E. Teller, and M.S. Weiss, Trans. N.Y. Acad. Sci. 40 (1980) 222.
- [9] C.T.A.M. de Laat and J.G. Kromme, Nucl. Instrum. Methods; Phys. Res. A 239 (1985) 556.
- [10] A. Taal, J.F.M. d'Achard van Enschut, J.B.R. Berkhout, W. Duinker, C.W.E. van Eijk, W.H.A. Hesselink, P.J. van den Hoek, T.J. Ketel, J.H. Koch, J. Konijn, C.T.A.M. de Laat, W. Lourens, G. van Middelkoop, W. Poeser, T. Prins and A.H. Wapstra, Phys. Lett. B 156 (1985) 296.
- [11] H. Janszen, Thesis University of Bonn, (1983).
- [12] P. David et., to be published.
- [13] J. Hartfiel, Thesis University of Bonn, (1985).
- [14] R. von Mutius, Thesis University of Bonn, (1985).

Appendix B

Details of pionic atom calculations

In this appendix detailed results are given of the calculations for the pionic atoms mentioned above, this in order to allow easier comparison with possible future experiments. Table B.1 gives the input values, used in the computer codes MESON, PIATOM and PIONDELTA. The important part of the output of MESON is given in tables B.2 - B.4. In table B.5 the results for the higher order corrections calculated with the code PIATOM are given. Table B.6 shows, how the pionic transition energies are calculated. The hyperfine complexes, calculated with our own written program PIONDELTA, are given in table B.7 - B.11.

Table B.1: Proton and neutron fermi distribution (c,t) and deformation (β) parameters and the average number of electrons in the K and L shells at the moment of the pionic transitions. The most recent value of the pion mass 139.56871 MeV [Jec 86] has been used.

Nucleus	c fm	t fm	β	Γ^π	N_K	N_L
^{181}Ta	6.347	2.15	0.278 \pm 0.005	$7/2^+$	1.69	5.63
$^{\text{nat}}\text{Re}$	6.40	2.15	0.220 \pm 0.002	$5/2^+$	1.70	5.65
$^{\text{nat}}\text{Pt}$	6.554	2.30	0	0	1.72	5.66
^{197}Au	6.5542	2.30	0.105 \pm 0.002	$3/2^+$	1.73	5.69
^{208}Pb	6.6516	2.286	0	0	1.77	5.83
^{209}Bi	6.6867	2.30	-0.025 \pm 0.002	$9/2^-$	1.77	5.83
^{237}Np	7.001	2.30	0.282 \pm 0.001	$5/2^+$	1.84	6.48

Table B.2: Calculated strong interaction monopole and quadrupole shifts, widths and the electromagnetic quadrupole constant A_2 for the 5g level in ^{237}Np with optical potential parameter sets from table 3.1. All values in keV.

parameters	$\epsilon_0^{\text{deform}}$	$\epsilon_0^{\text{total}}$	Γ_0^{deform}	Γ_0^{total}	$\text{Re } A_2$	
[Tau 71 $_{\xi=1}$]	-0.002	0.043	0.002	0.019	1.053	
[Tau 71 $_{\xi=0}$]	-0.000	0.045	0.003	0.022	1.053	
[Bat 79]	-0.003	0.045	0.002	0.020	1.053	
[Sek 83]	-0.004	0.040	0.001	0.017	1.053	
	$\epsilon_2^{\text{s-wave}}$	$\epsilon_2^{\text{p-wave}}$	$\epsilon_2^{\text{total}}$	$\Gamma_2^{\text{s-wave}}$	$\Gamma_2^{\text{p-wave}}$	Γ_2^{total}
[Tau 71 $_{\xi=1}$]	0.004	-0.009	-0.005	-0.001	-0.003	-0.003
[Tau 71 $_{\xi=0}$]	0.004	-0.009	-0.005	-0.000	-0.003	-0.003
[Bat 79]	0.005	-0.010	-0.005	-0.000	-0.003	-0.003
[Sek 83]	0.005	-0.009	-0.004	0.000	-0.003	-0.003

Table B.3: Calculated strong interaction monopole and quadrupole shifts, widths and the electromagnetic quadrupole constant A_2 for the 4f levels with optical potential parameter sets from table 3.1. All values in keV.

Parameters	$\epsilon_0^{\text{deform}}$	$\epsilon_0^{\text{total}}$	Γ_0^{deform}	Γ_0^{total}	$\epsilon_2^{\text{S-wave}}$	$\epsilon_2^{\text{P-wave}}$	$\epsilon_2^{\text{total}}$	$\text{Re } A_2$	$\Gamma_2^{\text{S-wave}}$	$\Gamma_2^{\text{P-wave}}$	Γ_2^{total}
^{181}Ta:	[Tau 71] $_{\xi=1}$	-0.026	0.524	0.027	0.324	0.069	-0.105	1.642	-0.009	-0.034	-0.043
	[Tau 71] $_{\xi=0}$	-0.004	0.568	0.036	0.378	0.075	-0.114	1.643	-0.005	-0.038	-0.043
	[Bat 79]	-0.044	0.539	0.024	0.339	0.086	-0.117	1.643	-0.002	-0.039	-0.041
	[Sek 83]	-0.055	0.473	0.015	0.287	0.094	-0.115	1.641	0.004	-0.038	-0.033
^{187}Re:	[Tau 71] $_{\xi=1}$	-0.022	0.680	0.023	0.430	0.056	-0.083	1.117	-0.005	-0.028	-0.033
	[Tau 71] $_{\xi=0}$	-0.004	0.743	0.031	0.517	0.062	-0.091	1.118	0.000	-0.033	-0.033
	[Bat 79]	-0.037	0.700	0.019	0.444	0.069	-0.092	1.117	0.002	-0.032	-0.030
	[Sek 83]	-0.046	0.618	0.011	0.377	0.075	-0.091	1.116	0.006	-0.031	-0.025
natP:	[Tau 71] $_{\xi=1}$	0	1.020	0	0.624	0	0	0	0	0	0
	[Tau 71] $_{\xi=0}$	0	1.095	0	0.739	0	0	0	0	0	0
	[Bat 79]	0	1.064	0	0.644	0	0	0	0	0	0
	[Sek 83]	0	0.956	0	0.551	0	0	0	0	0	0
^{197}Au:	[Tau 71] $_{\xi=1}$	-0.008	1.132	0.008	0.715	0.026	-0.036	0.379	-0.001	-0.013	-0.013
	[Tau 71] $_{\xi=0}$	-0.002	1.217	0.011	0.850	0.028	-0.040	0.380	0.002	-0.015	-0.014
	[Bat 79]	-0.013	1.178	0.007	0.736	0.031	-0.040	0.380	0.002	-0.015	-0.012
	[Sek 83]	-0.016	1.054	0.003	0.626	0.032	-0.040	0.379	0.004	-0.014	-0.010
^{208}Pb:	[Tau 71] $_{\xi=1}$	0	1.613	0	1.085	0	0	0	0	0	0
	[Tau 71] $_{\xi=0}$	0	1.779	0	1.351	0	0	0	0	0	0
	[Bat 79]	0	1.657	0	1.091	0	0	0	0	0	0
	[Sek 83]	0	1.480	0	0.926	0	0	0	0	0	0
^{209}Bi:	[Tau 73] $_{\xi=1}$	-0.001	1.794	0.001	1.217	-0.027	0.037	-0.302	-0.001	0.014	0.013
	[Tau 71] $_{\xi=0}$	0.000	1.960	0.001	1.485	-0.030	0.042	-0.303	-0.005	0.018	0.013
	[Bat 79]	-0.001	1.850	0.001	1.228	-0.033	0.041	0.009	-0.302	0.016	0.011
	[Sek 83]	-0.002	1.651	0.000	1.038	-0.033	0.041	0.007	-0.301	0.016	0.010
^{237}Np:	[Tau 71] $_{\xi=1}$	-0.312	4.681	0.330	4.133	0.734	-0.833	4.295	0.015	-0.370	-0.355
	[Tau 71] $_{\xi=0}$	-0.080	5.279	0.469	4.076	0.808	-0.926	4.312	0.107	-0.465	-0.358
	[Bat 79]	-0.535	4.541	0.256	4.000	0.901	-0.919	4.295	0.104	-0.398	-0.294
	[Sek 83]	-0.709	3.792	0.115	3.235	0.971	-0.906	4.270	0.145	-0.366	-0.220

Table B.4: Calculated strong interaction monopole and quadrupole shifts, widths and the electromagnetic quadrupole constant A_2 for the 3d levels with optical potential parameter sets from table 3.1. All values in keV.

Parameters	E_0^{deform}	E_0^{total}	Γ_0^{deform}	Γ_0^{total}	$e_2^{\text{s-wave}}$	$e_2^{\text{p-wave}}$	e_2^{total}	Re A_2	$\Gamma_2^{\text{s-wave}}$	$\Gamma_2^{\text{p-wave}}$	Γ_2^{total}
^{181}Ta											
[Tau 71 $_{\xi=1}$]	-2.056	21.245	2.964	42.134	7.640	-3.909	3.732	9.708	0.908	-1.474	-0.566
[Tau 71 $_{\xi=0}$]	-0.833	26.991	4.031	49.956	8.522	-4.429	4.093	9.910	1.796	-1.615	0.182
[Bat 79]	-3.890	17.805	2.015	38.459	9.030	-4.479	4.550	9.610	1.766	-1.672	0.093
[Sek 83]	-5.944	11.111	3.000	30.365	9.825	-4.702	5.123	9.408	2.252	-1.843	0.410
^{187}Re											
[Tau 71 $_{\xi=1}$]	-1.582	24.771	2.215	50.236	5.575	-2.830	2.745	6.562	0.980	-1.080	-0.100
[Tau 71 $_{\xi=0}$]	-0.700	32.128	3.094	60.942	6.324	-3.302	3.022	6.732	1.843	-1.243	0.601
[Bat 79]	-2.951	20.979	1.440	45.373	6.504	-3.263	3.240	6.479	1.577	-1.276	0.300
[Sek 83]	-4.475	13.738	0.080	36.213	6.963	-3.440	3.524	6.328	1.873	-1.458	0.415
^{197}Au											
[Tau 71 $_{\xi=1}$]	0	29.643	0	61.473	0	0	0	0	0	0	0
[Tau 71 $_{\xi=0}$]	0	38.070	0	72.997	0	0	0	0	0	0	0
[Bat 79]	0	26.024	0	55.325	0	0	0	0	0	0	0
[Sek 83]	0	18.708	0	45.117	0	0	0	0	0	0	0
^{208}Pb											
[Tau 71 $_{\xi=1}$]	-0.452	30.582	0.626	67.340	2.017	-0.999	1.018	2.169	0.504	-0.394	0.110
[Tau 71 $_{\xi=0}$]	-0.210	39.532	0.885	80.270	2.283	-1.196	1.087	2.231	0.826	-0.456	0.369
[Bat 79]	-0.837	26.470	0.389	60.362	2.294	-1.156	1.138	2.136	0.678	-0.476	0.202
[Sek 83]	-1.269	18.296	0.006	48.764	2.373	-1.214	1.159	2.081	0.712	-0.551	0.161
^{209}Bi											
[Tau 71 $_{\xi=1}$]	0	33.542	0	84.280	0	0	0	0	0	0	0
[Tau 71 $_{\xi=0}$]	0	46.846	0	104.415	0	0	0	0	0	0	0
[Bat 79]	0	27.243	0	73.902	0	0	0	0	0	0	0
[Sek 83]	0	17.470	0	60.358	0	0	0	0	0	0	0
^{209}Bi											
[Tau 71 $_{\xi=1}$]	-0.034	34.502	0.046	90.525	-1.728	0.847	-0.881	-1.674	-0.559	0.331	-0.228
[Tau 71 $_{\xi=0}$]	-0.018	47.556	0.067	109.882	-1.986	1.061	-0.925	-1.732	-0.911	0.416	-0.494
[Bat 79]	-0.062	28.189	0.027	79.389	-1.929	0.985	-0.944	-1.641	-0.679	0.422	-0.258
[Sek 83]	-0.094	17.747	-0.005	64.292	-1.961	1.039	-0.922	-1.593	-0.676	0.511	-0.165

Table B.5: Higher order corrections to the pionic level energies. Though nearly independent of parametersets, the set from ref. [Bat 79] was used since its predictions come closest to the measured values. All values, in keV, apply to levels with $l = n - 1$.

	n	finite size	$\alpha(\alpha Z)$	$\alpha^2(\alpha Z)$	$\alpha(\alpha Z)^3$	$\alpha(\alpha Z)^{5,7}$	el-screen	Lamb shift	nuc.pol.	redmass	Σ corr	Σ corr *)
^{181}Ta:	3	3.594	-11.8305	-0.0856	0.1270	0.0141	6.9736	-0.0002	-0.1703	-0.0190	-1.3969	-4.9909
	4	0.011	-4.3307	-0.0303	0.0796	0.0088	6.9539	0	-0.0110	-0.0046	2.6767	2.6657
	5	0.000	-1.8975	-0.0134	0.0441	0.0049	6.9215	0	-0.0014	-0.0019	5.0563	5.0563
^{187}Re:	3	4.330	-12.6951	-0.0920	0.1381	0.0163	7.2821	-0.0002	-0.1966	-0.0205	-1.2379	-5.5679
	4	0.014	-4.6680	-0.0327	0.0893	0.0105	7.2604	0	-0.0130	-0.0050	2.6555	2.6415
	5	0.000	-2.0528	-0.0144	0.0497	0.0058	7.2249	0	-0.0017	-0.0020	5.2095	5.2095
^{195}Pt:	3	6.128	-14.0162	-0.1019	0.1567	0.0202	7.7686	-0.0003	-0.2388	-0.0230	-0.3067	-6.4347
	4	0.022	-5.2057	-0.0364	0.1053	0.0136	7.7433	0	-0.0166	-0.0056	2.6199	2.5979
	5	0.000	-2.2999	-0.0161	0.0590	0.0076	7.7026	0	-0.0021	-0.0023	5.4488	5.4488
^{197}Au:	3	6.787	-14.4985	-0.1055	0.1621	0.0215	7.9597	-0.0003	-0.2551	-0.0241	0.0468	-6.7402
	4	0.025	-5.3926	-0.0378	0.1112	0.0147	7.9330	0	-0.0178	-0.0058	2.6299	2.6049
	5	0.000	-2.3861	-0.0167	0.0624	0.0083	7.8902	0	-0.0023	-0.0024	5.5534	5.5534
^{208}Pb:	3	9.077	-15.8718	-0.1158	0.1826	0.0264	8.6163	-0.0004	-0.3053	-0.0265	1.5825	-7.4945
	4	0.038	-5.9802	-0.0419	0.1300	0.0188	8.5849	0	-0.0227	-0.0064	2.7205	2.6825
	5	0.000	-2.6565	-0.0186	0.0736	0.0106	8.5350	0	-0.0028	-0.0026	5.9387	5.9387
^{209}Bi:	3	10.095	-16.3793	-0.1197	0.1896	0.0282	8.7827	-0.0004	-0.3234	-0.0270	2.2457	-7.8493
	4	0.044	-6.1850	-0.0434	0.1366	0.0203	8.7497	0	-0.0243	-0.0067	2.6912	2.6472
	5	0.000	-2.7506	-0.0193	0.0776	0.0115	8.6975	0	-0.0030	-0.0027	6.0110	6.0110
^{237}Np:	4	0.181	-8.4921	-0.0598	0.2179	0.0423	11.2430	0	-0.0493	-0.0094	3.0736	2.8926
	5	0.001	-3.8046	-0.0266	0.1275	0.0247	11.1552	0	-0.0059	-0.0038	7.4675	7.4665
	6	0.000	-1.8930	-0.0134	0.0765	0.0148	11.0357	0	-0.0012	-0.0018	9.2176	9.2176

*) Sum of all corrections except the finite size, one of which is customarily incorporated into ϵ_0 since also dependent on the distribution parameters c and t .

Table B.6: Theoretical predictions for the electromagnetic part of the pionic levels including the higher order corrections from table B.5 but without strong interaction and finite size effects.

n	l	Bohr radius fm	$E_{pt}(\text{Coulomb})$ keV	$\Sigma\text{corrections}$ keV	$E_{pt}+\Sigma\text{corr}$ keV	$E_{\text{transition}}$ keV
¹⁸¹Ta						
3	2	23.91	-2230.484	-4.9909	-2235.475	992.747
4	3	42.50	-1245.394	2.6657	-1242.728	
5	4	66.41	-794.739	5.0563	-789.683	
^{nat}Re						
3	2	23.27	-2356.361	-5.5679	-2361.929	1049.447
4	3	41.37	-1315.123	2.6415	-1312.482	
5	4	64.63	-839.098	5.2095	-833.889	
^{nat}Pt						
3	2	22.37	-2551.960	-6.4347	-2558.395	1137.639
4	3	39.77	-1423.354	2.5979	-1420.756	
5	4	62.15	-907.923	5.4488	-902.474	
¹⁹⁷Au						
3	2	22.09	-2618.972	-6.7402	-2625.712	1167.916
4	3	39.27	-1460.401	2.6049	-1457.796	
5	4	61.36	-931.473	5.5534	-925.920	
²⁰⁸Pb						
3	2	21.28	-2825.556	-7.4945	-2833.051	1261.231
4	3	37.83	-1574.502	2.6825	-1571.820	
5	4	59.11	-1003.979	5.9387	-998.040	
²⁰⁹Bi						
3	2	21.02	-2896.230	-7.8493	-2904.079	1293.227
4	3	37.38	-1613.500	2.6472	-1610.853	
5	4	58.40	-1028.751	6.011	-1022.740	
²³⁷Np						
4	3	33.35	-2030.673	2.8926	-2027.780	741.785
5	4	52.12	-1293.462	7.4665	-1285.996	
6	5	75.05	-896.154	9.2176	-886.936	

Table B.7: Relative intensities and energy displacements of the transitions in the pionic $5g \rightarrow 4f$ and $4f \rightarrow 3d$ ^{197}Au hyperfine multiplets.

Transition	$4f \rightarrow 3d$		$5g \rightarrow 4f$	
	relative Intensity	ΔE keV	relative Intensity	ΔE keV
$11/2 \rightarrow 9/2$			100.00	-0.295
$9/2 \rightarrow 7/2$	100.00	-0.617	76.78	0.611
$9/2 \rightarrow 9/2$			6.93	-0.559
$7/2 \rightarrow 5/2$	68.98	1.718	57.54	0.160
$7/2 \rightarrow 7/2$	11.39	-1.787	9.12	0.703
$7/2 \rightarrow 9/2$			0.20	-0.467
$5/2 \rightarrow 3/2$	44.84	-0.225	42.75	-0.744
$5/2 \rightarrow 5/2$	14.74	2.261	6.92	0.423
$5/2 \rightarrow 7/2$	0.57	-1.244	0.26	0.966
$3/2 \rightarrow 1/2$	27.86	-2.546		
$3/2 \rightarrow 3/2$	11.24	0.941		
$3/2 \rightarrow 5/2$	0.81	3.428		

Table B.8: Relative intensities and energy displacements of the transitions in the pionic $5g \rightarrow 4f$ and $4f \rightarrow 3d$ ^{209}Bi hyperfine multiplets.

Transition	$4f \rightarrow 3d$		$5g \rightarrow 4f$	
	relative Intensity	ΔE keV	relative Intensity	ΔE keV
$17/2 \rightarrow 15/2$			100.00	0.183
$15/2 \rightarrow 13/2$	100.00	1.065	75.41	-0.197
$15/2 \rightarrow 15/2$			13.34	0.279
$13/2 \rightarrow 11/2$	66.88	-1.767	54.82	-0.265
$13/2 \rightarrow 13/2$	20.21	1.541	21.84	-0.167
$13/2 \rightarrow 15/2$			0.95	0.309
$11/2 \rightarrow 9/2$	41.13	-1.461	37.82	-0.134
$11/2 \rightarrow 11/2$	31.13	-1.670	26.16	-0.279
$11/2 \rightarrow 13/2$	2.31	1.639	2.56	-0.182
$9/2 \rightarrow 7/2$	21.64	0.615	24.06	0.099
$9/2 \rightarrow 9/2$	34.26	-1.606	26.89	-0.176
$9/2 \rightarrow 11/2$	6.32	-1.815	4.53	-0.322
$7/2 \rightarrow 5/2$	7.90	3.345	13.28	0.354
$7/2 \rightarrow 7/2$	30.43	0.341	24.55	0.044
$7/2 \rightarrow 9/2$	11.59	-1.881	6.60	-0.231
$5/2 \rightarrow 3/2$			5.25	0.573
$5/2 \rightarrow 5/2$	19.73	3.034	19.60	0.299
$5/2 \rightarrow 7/2$	17.82	0.030	8.49	-0.012
$3/2 \rightarrow 3/2$			12.24	0.526
$3/2 \rightarrow 5/2$	25.10	2.760		
$1/2 \rightarrow 3/2$			11.13	0.496

Table B.9: The hyperfine splitting of the pionic ^{181}Ta $4f \rightarrow 3d$ and $5g \rightarrow 4f$ transitions.

Transition	$4f \rightarrow 3d$		$5g \rightarrow 4f$	
	relative Intensity	ΔE keV	relative Intensity	ΔE keV
15/2 \rightarrow 13/2			100.00	-1.421
13/2 \rightarrow 11/2	100.00	-6.056	77.10	1.298
13/2 \rightarrow 13/2			11.73	-2.097
11/2 \rightarrow 9/2	70.64	8.968	56.55	1.686
11/2 \rightarrow 11/2	18.00	-9.451	19.20	1.099
11/2 \rightarrow 13/2			0.72	-2.296
9/2 \rightarrow 7/2	43.55	6.804	39.24	0.722
9/2 \rightarrow 9/2	28.93	8.383	22.46	1.800
9/2 \rightarrow 11/2	1.80	-10.038	1.86	1.213
7/2 \rightarrow 5/2	22.61	-3.707	25.36	-0.801
7/2 \rightarrow 7/2	31.21	7.881	22.12	1.007
7/2 \rightarrow 9/2	4.99	9.460	3.05	2.084
5/2 \rightarrow 3/2	8.32	-15.726	14.65	-2.271
5/2 \rightarrow 5/2	26.45	-1.899	19.06	-0.461
5/2 \rightarrow 7/2	8.56	9.689	3.90	1.347
3/2 \rightarrow 1/2			6.62	-3.258
3/2 \rightarrow 3/2	16.74	-13.915	14.23	-1.964
3/2 \rightarrow 5/2	11.64	-0.088	4.05	-0.153
1/2 \rightarrow 1/2			9.27	-3.048
1/2 \rightarrow 3/2	14.00	-12.621		
1/2 \rightarrow 3/2			3.12	-1.754

Table B.10: Relative intensities and energy displacements of the transitions in the pionic $5g \rightarrow 4f$ and $4f \rightarrow 3d$ natural Re hyperfine multiplets.

Transition	$4f \rightarrow 3d$		$5g \rightarrow 4f$	
	relative Intensity	ΔE keV	relative Intensity	ΔE keV
13/2 \rightarrow 11/2			100.00	-0.910
11/2 \rightarrow 9/2	100.00	-5.059	76.95	1.119
11/2 \rightarrow 11/2			9.71	-1.472
9/2 \rightarrow 7/2	70.64	8.914	56.82	1.072
9/2 \rightarrow 9/2	15.32	-7.650	15.02	1.045
9/2 \rightarrow 11/2			0.46	-1.547
7/2 \rightarrow 5/2	44.07	4.777	40.32	0.002
7/2 \rightarrow 7/2	23.48	8.887	16.26	1.284
7/2 \rightarrow 9/2	1.23	-7.677	1.03	1.257
5/2 \rightarrow 3/2	23.94	-5.981	27.49	-1.276
5/2 \rightarrow 5/2	23.88	6.059	14.10	0.337
5/2 \rightarrow 7/2	2.98	10.169	1.33	1.619
3/2 \rightarrow 1/2	10.07	-15.232	18.22	-2.193
3/2 \rightarrow 3/2	19.00	-4.367	9.18	-0.946
3/2 \rightarrow 5/2	4.15	7.672	1.03	0.668
1/2 \rightarrow 1/2	12.64	-13.985		
1/2 \rightarrow 3/2	3.72	-3.120		

Table B.11: Relative intensities and energy displacements of the transitions in the pionic $5g \rightarrow 4f$ ^{237}Np hyperfine multiplet.

Transition	$5g \rightarrow 4f$	
	relative Intensity	ΔE keV
13/2 \rightarrow 11/2	100.00	-3.245
11/2 \rightarrow 9/2	78.24	4.077
11/2 \rightarrow 11/2	9.66	-5.325
9/2 \rightarrow 7/2	57.74	3.863
9/2 \rightarrow 9/2	15.27	3.813
9/2 \rightarrow 11/2	0.46	-5.589
7/2 \rightarrow 5/2	40.61	-0.049
7/2 \rightarrow 7/2	16.55	4.667
7/2 \rightarrow 9/2	1.05	4.618
5/2 \rightarrow 3/2	27.39	-4.706
5/2 \rightarrow 5/2	14.25	1.211
5/2 \rightarrow 7/2	1.36	5.928
3/2 \rightarrow 1/2	18.02	-8.035
3/2 \rightarrow 3/2	9.18	-3.466
3/2 \rightarrow 5/2	1.04	2.451

Table B.12: Relative intensities and energy displacements of the transitions in the muonic $5g^{7/2} \rightarrow 4f^{5/2}$ and $5g^{9/2} \rightarrow 4f^{7/2}$ ^{237}Np hyperfine multiplets.

Transition	$5g^{7/2} \rightarrow 4f^{5/2}$		$5g^{9/2} \rightarrow 4f^{7/2}$	
	relative Intensity	ΔE keV	relative Intensity	ΔE keV
7 \rightarrow 6			100.00	0
6 \rightarrow 5	100.00	0	79.77	2.863
6 \rightarrow 6			7.99	-0.865
5 \rightarrow 4	73.66	2.609	61.87	2.983
5 \rightarrow 5	12.03	-0.750	12.53	2.724
5 \rightarrow 6			0.31	-1.004
4 \rightarrow 3	51.05	2.221	46.21	1.463
4 \rightarrow 4	18.39	2.556	13.72	3.292
4 \rightarrow 5	0.73	-0.802	0.68	3.033
3 \rightarrow 2	33.09	0.539	33.93	-0.170
3 \rightarrow 3	19.51	2.554	12.01	2.160
3 \rightarrow 4	1.67	2.890	0.85	3.817
2 \rightarrow 1	19.65	-1.176	24.80	-1.685
2 \rightarrow 2	16.58	1.008	7.73	0.386
2 \rightarrow 3	2.23	3.023	0.63	2.716
1 \rightarrow 0	10.14	-2.102		
1 \rightarrow 1	10.94	-0.759		
1 \rightarrow 2	1.85	1.424		

Table B.13: Relative intensities and energy displacements of the transitions in the muonic $6g^{7/2} \rightarrow 4f^{5/2}$ and $6g^{9/2} \rightarrow 4f^{7/2}$ ^{237}Np hyperfine multiplets.

Transition	$6g^{7/2} \rightarrow 4f^{5/2}$		$6g^{9/2} \rightarrow 4f^{7/2}$	
	relative Intensity	ΔE keV	relative Intensity	ΔE keV
7 \rightarrow 6			100.00	0
6 \rightarrow 5	100.00	0	79.43	2.830
6 \rightarrow 6			7.48	-0.470
5 \rightarrow 4	73.59	3.233	60.92	3.103
5 \rightarrow 5	12.79	-0.516	12.27	2.745
5 \rightarrow 6			0.30	-0.554
4 \rightarrow 3	51.36	2.921	45.59	1.755
4 \rightarrow 4	18.38	3.190	13.77	3.268
4 \rightarrow 5	0.82	-0.559	0.69	2.911
3 \rightarrow 2	33.65	0.915	33.60	-0.121
3 \rightarrow 3	19.18	3.142	12.19	2.061
3 \rightarrow 4	1.68	3.411	0.89	3.553
2 \rightarrow 1	20.15	-1.354	24.84	-1.787
2 \rightarrow 2	16.30	1.234	7.90	0.180
2 \rightarrow 3	2.16	3.461	0.66	2.361
1 \rightarrow 0	10.36	-2.752		
1 \rightarrow 1	10.86	-1.066		
1 \rightarrow 2	1.78	1.521		

Table B.14: Magnetic hyperfine constants for the pionic 5g, 4f and 3d levels in the investigated nuclei.

nucleus	$A_1(3d)$ eV	$A_1(4f)$ eV	$A_1(5g)$ eV
^{181}Ta	9.58	1.443	0.345
$^{\text{nat}}\text{Re}$	19.74	2.975	0.711
^{197}Au	1.74	0.262	0.063
^{209}Bi	18.98	2.860	0.683
^{237}Np		5.532	1.322

Summary

Strong and electromagnetic interactions in heavy exotic atoms

The atomic orbits of negatively charged leptons around a nucleus are entirely determined by the electroweak interaction. The influence of the properties of the nucleus is limited to that of the distributions of nuclear charge and magnetism (but for a slight influence of the weak interaction mainly causing nuclear absorption from the lowest orbit). This is also true for the outer orbits of negatively charged hadrons (e.g. pions). For their orbits nearer to the nucleus, however, the strong interaction becomes progressively more important. As a first consequence, the level energies are shifted with respect to the values following from the electromagnetic interaction alone. Even more important, the pions have a chance of being captured by the nucleus that drastically increases with decreasing principal quantum number. As a result, these levels become broadened.

Attempts have been made to describe these shifts and widths by inserting in the Klein Gordon equation for the pion-nucleus system an optical potential representing the strong interaction. The optical potential, developed from low energy pion nucleon scattering by Kisslinger and modified by Ericson and Ericson, adequately predicts the strong interaction effects of the complex energy levels in pionic orbits not too close to the nucleus. Rather recently experimental results for the deeply bound pionic 3d orbit in heavy nuclei such as ^{181}Ta , $^{\text{nat}}\text{Re}$ and ^{209}Bi indicate, that for them strong interaction widths are smaller by a factor of two or more than predicted from the standard optical potential. Such a tendency for strong interaction absorption widths has also been observed in other deeply bound pionic atom orbits: the 3p in ^{110}Pd , 2p in ^{75}As and 1s in ^{23}Na . These nuclei are reported to have smaller absorption widths by a factor of about 1.5 as compared to theoretical predictions. Similar deviations from theory have been observed for the strong interaction shifts.

Some of the above results have been thrown in doubt by Olin et al. on experimental grounds. Other authors suggested that the deviations might at least in some cases be due to the influence of nuclear deformation. Since correct knowledge of the properties of strong interaction is of evident importance, we studied some more cases, among them such ones (^{208}Pb , ^{209}Bi) for which deformation plays no role. The pionic X-ray spectra of ^{181}Ta , $^{\text{nat}}\text{Re}$, $^{\text{nat}}\text{Pt}$, ^{197}Au , ^{208}Pb and ^{209}Bi have been measured to obtain data which provide for a systematical investigation of the pionic 3d levels.

We devoted special attention to methods of obtaining clearly improved results. The improvement of the data was partly established by using modern spectroscopic equipment such as large-volume high-purity Ge-detectors in combination with Compton suppression BGO-shields. Further, good statistics on the "difficult" targets (Ta and Re are difficult because of their large

spectroscopic nuclear ground state quadrupole moments, which causes hyperfine splitting, Pb and Bi because the absorption is already large) was provided for by making the measurements using very intense pion beams at the meson factory PSI (formerly SIN). Highly important is also the attention paid in attempts to reduce backgrounds or, where this was not possible, to correct for them. Thus, e.g., the neutrons, produced in the target under investigation, cause in the Ge-detectors nuclear reactions and background-radiation. This background has largely been reduced by using neutron time-of-flight discrimination with respect to the incident stopped pion.

We showed with improved certainty that the deviations from the theory as mentioned above are indeed real. The widths of the pionic 3d levels are smaller by a factor 1.5 as compared to theoretical predictions. The same deviation as for $\Gamma_0(3d)$ is found for the strong interaction quadrupole shift, ϵ_2 , for both the 4f and 3d orbits. The pionic atom anomaly has recently been confirmed by low-energy π^+ scattering at LAMPF. Especially the π^- scattering on ^{58}Ni and ^{40}Ca at $E_\pi = 30$ and 20 MeV can be explained in terms of the above pionic atom anomaly. Conventional optical potentials do not agree as well with both the π^+ and π^- data.

An explanation for the difference can be found by adding an isovector term to the optical potential. Including an isovector absorption term in the standard optical potential with a negative value for $\text{Im}B_1$ or $\text{Im}C_1$ improves the theoretical values such that agreement is reached for the 3d data on pionic ^{208}Pb and ^{209}Bi , but partly destroys the relatively good agreement with the 4f data.

The muonic X-ray spectra of ^{238}Np provide us with model independent nuclear structure information. From the hyperfine splitting of the muonic $5g_{7/2} \rightarrow 4f_{5/2}$ and $5g_{9/2} \rightarrow 4f_{7/2}$ complexes we obtained the spectroscopic nuclear ground state quadrupole moment, determined to an accuracy of about 0.2%. From the main muonic $4f_{5/2} \rightarrow 3d_{3/2}$, $4f_{7/2} \rightarrow 3d_{5/2}$, $6g_{7/2} \rightarrow 4f_{5/2}$, $6g_{9/2} \rightarrow 4f_{7/2}$, $5g_{7/2} \rightarrow 4f_{5/2}$ and $5g_{9/2} \rightarrow 4f_{7/2}$ transition energies the $B(E2)\downarrow$ -values between various states and the quadrupole moment of the first excited nuclear state, with spin parity $I^\pi = 7/2^+$, were calculated.

Samenvatting

Sterke en electromagnetische wisselwerkingen in zware pionische atomen

De atomaire banen van negatief geladen leptonen zijn volledig bepaald door de electro-zwakke kracht. De invloed van de eigenschappen van de kern is beperkt tot die van de ruimtelijke verdeling van de lading en het magnetisme (en een kleine invloed van de zwakke wisselwerking hetgeen voornamelijk vangst uit de laagste banen veroorzaakt). Dit geldt ook voor meer naar *buiten gelegen banen van negatief geladen hadronen*, bijvoorbeeld pionen.

Voor de dieper gelegen banen wordt voor hadronen de sterke wisselwerking echter belangrijk. Een eerste gevolg is de verschuiving van de bindingsenergieën ten opzichte van de waarden die zouden gelden voor alleen electromagnetische wisselwerking. Nog belangrijker is het feit dat pionen ingevangen kunnen worden in de kern, een effect dat toeneemt met afnemend baanimpulsmoment. Dit absorptieproces veroorzaakt dat de atomaire niveaus verbreed zijn.

Doorgaans worden deze verschuivingen en verbredingen beschreven door in de Klein-Gordon vergelijking voor het pion-kern systeem een optische potentiaal in te voeren, die de sterke wisselwerking beschrijft. Deze optische potentiaal, door Kisslinger ontwikkeld vanuit pion-nucleon verstrooiing bij lage energie en later gemodificeerd door Ericson en Ericson, voorspelt adequaat de effecten van de sterke wisselwerking op de energieniveaus van niet te dicht bij de kern gelegen pionische banen. Recente experimentele resultaten voor sterk gebonden 3d banen in zware kernen zoals ^{181}Ta , $^{\text{nat}}\text{Re}$ en ^{209}Bi geven indicaties dat voor deze kernen de breedten ten gevolge van de sterke wisselwerking ongeveer een factor twee smaller zijn dan met behulp van de standaard optische potentiaal wordt voorspeld. Deze tendens voor absorptiebreedtes is ook waargenomen in andere diepgebonden toestanden in pionische atomen: het 3p niveau in ^{110}Pd , 2p in ^{75}As en het 1s niveau in ^{23}Na . Van deze kernen worden absorptiebreedten gerapporteerd, die een factor 1,5 kleiner zijn dan theoretisch voorspelde waarden. Soortgelijke afwijkingen zijn ook waargenomen voor verschuivingen ten gevolge van de sterke wisselwerking.

Op experimentele gronden worden sommige van de bovengenoemde resultaten door Olin en medewerkers in twijfel getrokken. Andere auteurs suggereren, dat een deel van de discrepantie verklaard zou kunnen worden door de invloed van de deformatie van de kern. Daar betrouwbare kennis van de eigenschappen van sterke wisselwerking van evident belang is, hebben we onderzoek verricht aan kernen, waarvoor deformatie geen rol speelt zoals ^{208}Pb , ^{209}Bi . De pionische Röntgenspectra van ^{181}Ta , $^{\text{nat}}\text{Re}$, $^{\text{nat}}\text{Pt}$, ^{197}Au , ^{208}Pb en ^{209}Bi zijn gemeten om gegevens te verkrijgen, die een systematisch onderzoek van pionische 3d niveaus mogelijk maakt.

Extra aandacht is besteed aan de methoden ter verkrijging van duidelijk betere resultaten dan in vroegere experimenten. De verbetering is onder andere gerealiseerd door het gebruik van moderne detectie-apparatuur, zoals germanium detectoren met kristallen van hoge zuiverheid en met grote detectievolumen geplaatst in Compton onderdrukkings BGO scintillatoren. Daarbij is, door gebruik te maken van hoge intensiteits pionenbundels aan de "Mesonenfabriek" Paul Scherrer Instituut (voorheen SIN), hoge statistiek behaald voor de "moeilijke" targets. Moeilijk zijn de metingen aan Ta en Re omdat deze kernen in hun grondtoestand grote quadrupooldeformaties hebben, welke hyperfijnsplittings veroorzaken, en aan Pb en Bi omdat voor deze kernen de absorptie uit het 3d niveau reeds aanzienlijk is. Er is veel aandacht besteed aan het onderdrukken van de achtergrond in de energiespectra. Neutronen, geproduceerd in de trefplaat, veroorzaken in de germaandetectoren kernreacties en achtergrondstraling. Deze achtergrond wordt voornamelijk gereduceerd door het gebruik van vluchtijddiscriminatie-technieken ten opzichte van het binnenkomende gestopte pion.

Onze metingen tonen zonder meer aan dat de bovengenoemde discrepanties inderdaad aanwezig zijn. De breedten van pionische 3d niveaus zijn een factor 1,5 kleiner vergeleken met de theorie. Dezelfde afwijking wordt ook gevonden voor de quadrupoolverschuiving door sterke interactie in zowel 4f als 3d banen. Deze anomalie wordt ook gevonden in verstrooiingsexperimenten voor laagenergetische geladen pionen in LAMPF. Met name de π^- verstrooiing op ^{58}Ni en ^{40}Ca bij $E_\pi = 30$ en 20 MeV kan worden verklaard in termen van de bovenbeschreven anomalie. Conventionele optische potentialen stemmen niet overeen met zowel de π^+ als de π^- resultaten.

Een verklaring voor de discrepantie kan gevonden worden door het toevoegen van isovectortermen aan de optische potentiaal. De toevoeging van een isovector-absorptieterm met een negatieve waarde voor het imaginaire deel van B_1 of C_1 in de standaard optische potentiaal verbetert de theoretische voorspellingen zodanig dat overeenstemming wordt bereikt voor de 3d resultaten in pionisch ^{208}Pb en ^{209}Bi , maar verslechtert gedeeltelijk de overeenstemming met de 4f waarden.

De muonische Röntgen spectra van ^{238}Np leverden model-onafhankelijke kernstructuur-informatie. Uit de hyperfijnsplitsing van de muonische $5g_{7/2} \rightarrow 4f_{5/2}$ en $5g_{9/2} \rightarrow 4f_{7/2}$ complexen verkregen we het spectroscopische quadrupoolmoment van de kern in de grondtoestand met een nauwkeurigheid van ongeveer 0,2%. Van de muonische $4f_{5/2} \rightarrow 3d_{3/2}$, $4f_{7/2} \rightarrow 3d_{5/2}$, $6g_{7/2} \rightarrow 4f_{5/2}$, $6g_{9/2} \rightarrow 4f_{7/2}$, $5g_{7/2} \rightarrow 4f_{5/2}$ en $5g_{9/2} \rightarrow 4f_{7/2}$ overgangsenergieën zijn de $B(E2)_{\downarrow}$ waarden tussen verschillende toestanden en het quadrupoolmoment van de eerste aangeslagen toestand, met spin en pariteit $I^\pi = 7/2^+$, berekend.

Curriculum vitae

De schrijver van dit proefschrift werd geboren op 1 april 1956 te Boxtel in Noord Brabant. In de middenlimburgse stad Roermond deed hij in mei 1976 eindexamen VWO aan de scholengemeenschap St. Ursula. Direct aansluitend vervulde hij zijn militaire dienst. Een jaar later, september 1977, werd de studie natuurkunde aangevangen aan de Technische Hogeschool te Delft. Het afstudeerwerk werd verricht bij de toenmalige vakgroep Experimentele Kernfysica.

Op 1 februari 1983 trad de schrijver dezes in dienst als wetenschappelijk medewerker van de Stichting voor Fundamenteel Onderzoek der Materie bij de PIMU (pion/muon) groep aan het Nationaal Instituut voor Kernfysica en Hoge-energiefysica (NIKHEF, sectie K) in Amsterdam. Aldaar en op het Schweizerisches Institut für Nuclearforschung (tegenwoordig het Paul Scherrer Institut) te Villigen, Zwitserland werd het in dit proefschrift beschreven onderzoek uitgevoerd.

Stellingen

behorend bij het proefschrift

Strong and electromagnetic interactions
in heavy exotic atoms

door

C.T.A.M. de Laat

Delft, 31 maart 1988

1. De doorberekening van de systematische fout in de uiteindelijk opgegeven fout als gedaan door de auteurs van ref [Oli 85] is onjuist.
[Oli 85] A. Olin et al.; Nuclear Physics A439 (1985) 589
2. Voor het accuraat evalueren van γ -spectra is het meenemen van een stapfunctie noodzakelijk.
Dit proefschrift, hoofdstuk 2.
3. Veel auteurs nemen vol trots de correctie voor de Lamb shift mee naast andere correcties in pionisch-atoommetingen aan het atomaire 3d niveau. Dit toont gebrek aan besef over de fysische achtergrond van dit effect.
Dit proefschrift, hoofdstuk 3.
4. De voorspelling van hett Nilsson-model dat banen in verschillende kernen met dezelfde quantumgetallen hetzelfde quadropoolmoment hebben wordt bevestigd door pionische en muonische metingen.
Dit proefschrift, hoofdstuk 5.
5. Door de wildgroei in definities voor de eigenschappen van Compton-onderdrukkingssystemen is een goede onderlinge vergelijking moeilijk en soms zelfs onmogelijk.
[Nol 85] P.J. Nolan et al.; Nucl. Instr. & Meth. in Phys. Res. A236 (1985) 95
M.A. van Driel; proefschrift, Rijksuniversiteit Utrecht, 1976.
Dit proefschrift, hoofdstuk 2.
6. De Primakov-formule [Gou 74] wordt door een aantal auteurs [Wil 78], [Wil 80] verkeerd gegeven. De reden is een fout in de originele publicatie.
[Gou 74] B. Goulard and H. Primakoff; Phys.rev. C10 (1974) 2034
[Wil 78] W.W. Wilke et al.; Phys.rev. C18 (1978) 1452
[Wil 80] W.W. Wilke et al.; Phys.rev. C21 (1980) 2019

7. De door Fujiwara et al. [Fuj 80] berekende ladingsverdeling van de eerste 0^+ excitatie in ^{12}C geeft aan dat de gebruikelijke benadering, waar in de berekening van de werkzame doorsnede van inelastische electronenverstrooiing de electronengolf slechts wordt beïnvloed door de ladingsverdeling van de grondtoestand, in dit geval niet juist is.
[Fuj 80] Y. Fujiwara et al.; Supp. Progress of Theoretical Physics 68 (1980) 29
8. Hoewel de methode die de auteurs [Gov 74] gebruikt hebben om het percentage positrondesintegratie in ^{132}Cs te bepalen in principe zeer nauwkeurig zou moeten zijn, moet geconcludeerd worden dat hun resultaat aanzienlijk onnauwkeuriger is dan de door hun opgegeven fout.
[Gov 74] S.C. Govere et al.; Nucl. Phys. A227 (1974) 506
[Laa 87] C.T.A.M. de Laat et al.; J. Phys. G: Nuclear Physics 13 (1987) 1283
9. Experimentatoren moeten hun experimenten verdedigen voor onder andere door theoretici bemande Program Advisory Committees (PAC's). Het ware evenwichtiger, indien ook theoretici budgetten zouden moeten aanvragen voor een onder andere door experimentatoren bemande PAC.
10. Sporten, waarbij zij die de inspanning verrichten en zij die in naam de sport beoefenen niet dezelfde zijn, verdienen die naam niet. (b.v. "duivensport", "hengelsport")
11. Het is zeer gewenst dat er telefoonboeken (bij voorkeur elektronische) voor computermail-adressen komen.
12. Een nadelig effect van de huidige hoge frequentie, waarmee steeds nieuwe nog snellere microprocessors worden geïntroduceerd in de personal-computerwereld, is het niet tot volle ontplooiing komen van besturingsystemen voor de tussenliggende modellen.